

Rheology and hydraulic fracture in cataract surgery

Zhiwei Li

A thesis submitted in fulfilment
of the requirements for the degree of
Doctor of Philosophy



UNSW
SYDNEY

School of Chemical Engineering
Faculty of Engineering
University of New South Wales

12 December 2020

Copyright Statement

I hereby grant the University of New South Wales or its agents a non-exclusive licence to archive and to make available (including to members of the public) my thesis or dissertation in whole or part in the University libraries in all forms of media, now or here after known. I acknowledge that I retain all intellectual property rights which subsist in my thesis or dissertation, such as copyright and patent rights, subject to applicable law. I also retain the right to use all or part of my thesis or dissertation in future works (such as articles or books).

For any substantial portions of copyright material used in this thesis, written permission for use has been obtained, or the copyright material is removed from the final public version of the thesis.

Signed

Date

Authenticity Statement

I certify that the Library deposit digital copy is a direct equivalent of the final officially approved version of my thesis.

Signed

Date

Originality Statement

I hereby declare that this submission is my own work and to the best of my knowledge it contains no material previously published or written by another person, or substantial portions of material which have been accepted for the award of any other degree or diploma at UNSW or any other educational institute, except where due acknowledgment is made in the thesis. Any contribution made to the research by others, with whom I have worked at UNSW or elsewhere, is explicitly acknowledged in the thesis. I also declare that the intellectual content of this thesis is the product of my own work, except to the extent that assistance from others in the project's design and conception or in style, presentation and linguistic expression is acknowledged.

Signed

Date

Abstract

Cataracts are responsible for almost half of worldwide blindness, making it one of the biggest health challenges in this era. Cataracts are irreversible because of their pathology, which is controlled by the aging and biochemical change of eye tissues. As a result cataract surgery is currently the only effective treatment. The general procedure of cataract surgery includes separation and removal of the failed lens tissue from the surrounding soft tissue in the eye, followed by artificial lens implantation. Lens removal requires successful separation of lens tissues as a critical step that determines surgical success. However key parts of cataract separation affected by fluid mechanics and rheology are uncharacterised. This project aims to explain the behaviors of such separation phenomena and connect fundamentals with possible explanations and enhancements.

A multi-layer bio-polymer injection model is developed to mimic the separation process in cataract surgeries. The separation can be considered peeling of a soft elastic tissue by a pressure-driven fluid flow, whose performance is closely related to properties such as flow rate and velocity as well as fluid viscosity, normal stress and yield stress. In our project, the separation physics is studied as a hydraulic fracture problem. Theories are proposed to discuss the effectiveness and safety of hydraulic fracture with different flow and fluid parameters. It is found both higher flow rate and viscosity will cause tissue to be deformed more, which may increase the risks of tissue damage. Yield stress fluids with significant elasticity are not suitable as in most cases they rupture the tissue. Normal stress fluids have the potential to provide safe and effective separation. It is found that with a small scale separation, however, the separation effectiveness is mainly affected by the flow rate, and the fluid properties play a more minor role. General ideas and potential improvements according to our results and theories are also proposed for cataract surgeries, which we hope will contribute to easier and safer separation.

Acknowledgments

Firstly, I would like to express my special appreciation to my supervisor, Associate Professor Patrick T. Spicer, whom offered me valuable research opportunity in his group. My research and thesis would not have been possible without his guidance, advice and support.

Thank you for sharing your knowledge in fluid mechanics and rheology. Also thank you for guiding and supporting me through the entire journey. It has been a long journey and you have been a wonderful mentor. Among all the valuable things I have learned from your supervision, such as research skills and critical thinking, one that will influence my future life deeply is "always have passion to your work". This was not taught by talking but by what I observed everyday working with you.

Also, I would like to thank you for constantly improving my ability on spotting and solving problems, and more importantly the ability to set up priorities and get things done when overwhelming tasks happens. All these will be benefit to my future career.

Again, it has been a memorable time to have you as my supervisor in my PhD's study and thank you for all the helps.

Many thanks to Dr. Ian Dinihan for funding this project and providing professional knowledge and insights regarding cataract surgery. The time working with you was a good memory.

I would also like to thank my co-supervisor, Associate Professor Stuart Prescott, for his valuable advice on the project. Thanks for helping me see my project in different aspects.

Many thanks to the lab managers, Camillo Taraborrelli and Eh Hau Pan, for providing access to the labs and instruments, and ordering chemicals. Also to all other chemical engineering staff in UNSW who helped and supported my work and campus life.

I acknowledge all the Complex Fluids group members at UNSW: Jie, Haiqiao, Zengyi, Goldina, Prerna, Isaac, Haoda, Firoozeh and Maryam. Being friends and working with you make my PhD journey a very happy memory in my life. Thank you for the friendship, help and advises.

I must mention my girlfriend, Xiaoying Lu. Thank you for your company and understanding in all the time. Your support gives me great power.

Last but not least, thank to my father and mother who unconditionally support me and encourage me to pursue my decisions. Thank you for giving me strength.

Contents

Abstract	i
List of Figures	vii
1 Introduction	1
1.1 References	2
2 Literature review	3
2.1 Structure of the human eye and lens	3
2.2 Cataract surgery	8
2.3 Eye lens bio-mechanics	13
2.4 Blister test	17
2.5 Fracture mechanism	20
2.5.1 Newtonian fluid hydraulic fracture	23
2.5.2 Shear-thinning fluid hydraulic fracture	27
2.5.3 Yield stress and normal stress	32
2.6 Conclusion	36
2.7 References	38
3 Adhesion measurement	43
3.1 Materials and methods	44
3.1.1 Interface roughness measurement	45
3.1.2 Experimental set-up	48
3.1.3 Adhesion measurement	48
3.1.4 Blister image processing	50
3.2 Results and discussion	52
3.3 Conclusion	58
3.4 References	59
4 Newtonian fluid separation	61
4.1 Theory	62
4.2 Materials and methods	65

4.2.1	Experimental set-up	65
4.2.2	Curvature analyses	67
4.3	Results and discussion	68
4.4	Conclusion	72
4.5	References	73
5	Shear-thinning fluid separation	75
5.1	Theory	76
5.2	Materials and methods	79
5.2.1	Experimental set-up	79
5.2.2	Curvature analyses	80
5.3	Results and Discussion	81
5.4	Conclusion	92
5.5	References	92
6	Complex fluid separation	95
6.1	Materials and methods	98
6.1.1	Experimental set-up	98
6.1.2	Curvature analyses	100
6.2	Results and Discussion	101
6.2.1	Yield stress fluids	101
6.2.2	Normal stress fluids	105
6.3	Conclusion	110
6.4	References	111
7	Conclusion	113
A	MATLAB - curvature measurement code	117
B	MATLAB - error propagation code	119

List of Figures

- 2.1 Structure of the human eye. The lens is located posterior to the aqueous humor and iris, and anterior directly to the vitreous. The primary function of the lens is to focus light going into the eye and project it onto the retina. The zonular fibers merge to the whole equator region and part of the anterior and posterior regions. Figure reproduced from Remington and Goodwin¹. 3
- 2.2 Structure of the eye lens. The capsule is a thin layer of fiber surrounding the whole lens. Posterior to the anterior capsule is the single-layer epithelium. Inside this onion-like structure are the cortex and nucleus, which are the lens fibers differentiated from early epithelium. Figure reproduced from COURSE². 4
- 2.3 Cross-sectional profile of lens capsule fiber cells. The cells are arranged in a hexagonal pattern. The capsule has an onion like structure consisting of layers of fiber cells. Each of these layers is made up of adjacent fibers. Figure reproduced from Adler⁶. 5
- 2.4 Left: SEM photo of nucleus lens fiber cross-sectional profile. Figure reproduced from TROKEL¹¹. Right: Onion-like structure of nucleus and cortex fibers arrangement. Figure reproduced from Aliò *et al.*¹². . . 6
- 2.5 Configuration of fiber cells showing that each element has a $3\ \mu\text{m} \times 9\ \mu\text{m}$ dimension. The angle of sides between two gap junctions is 60° and is not shown precisely. Morphology of layer-layer interface is outlined with red square. Figure reproduced from Mathias *et al.*¹³. . . 7
- 2.6 Immunofluorescence microscopy shows the hexagonal cross-sectional profile of the lens fiber cells. The red color is the location of cadherin, the green color indicates the ezrin-based complex, the framework of fiber cells. The third image merges these two components and shows the overall distribution of the two different complexes. Figure reproduced from Straub *et al.*¹⁴. 7

2.7	The general process of cataract surgery. Here the lens is portrayed as a simple elliptical shape. The outer layer (grey color) is the capsule, the epithelium layer is located between the cortex and capsule and is not shown as it is quite thin. Not all dimensions are to scale.	9
2.8	Multi-quadrant fracture of the eye lens nucleus. Figure reproduced from WebMD ²³	10
2.9	Performance of fracture fluids. A: attachment still exists between capsule and nucleus; B: small clearance and less fluid support; C: easy movement of nucleus blocks the entry; D: good support and sufficient clearance.	11
2.10	A bulge elasticity measurement. The anterior capsule is cut to a round shape and clamped at the aperture between two glass slides. The fluid is pressurized at one side of the capsule, causing deformation bulging. The radius of curvature of the bulge, R , pressure change due to change of volume P , initial volume of capsule V , thickness of capsule t and Poisson's ratio ν are then used to calculate elasticity: $E = \frac{3}{2} \frac{PR}{t} (1 - \nu) V$. Figure reproduced from Fisher ⁸	14
2.11	Capsule tissue tensile test. Arrow indicates ring-shaped specimen. The lens capsule is extracted from the eye and cut to a capsule ring along the equatorial region for measurement. It is then fixed by two pins on the probes and stretched. Figure reproduced from Krag and Andreassen ⁷	15
2.12	Thickness of capsule increases with age until age 75 and then drops slightly. The posterior is the thinnest part and shows an almost constant value. The yield strain decreases continuously from over 100% to about 40% in elders. Figure reproduced from Krag <i>et al.</i> ¹⁷	16
2.13	Configuration of a blister test sample. Here l is the extended length, R the radial length of the blister edge, r the constrained radial length, and h the height between gelatin and glass slide.	18

2.14	Separation system is divided into a stabilized region (A) where no deformation occurs, and a deforming region (B). Part of region B is fluid-filled and the rest is a vapor tip region. l is the peeling length scale of Equation (2.17) that represents the magnitude of the vapor tip, R_F is the length of the fluid-filled deforming region. σ is the compression stress normal to the soft tissue.	20
2.15	Schematic of a typical hydraulic fracture in a general material with the assumption of a fluid vapor tip. Figure reproduced from Garagash and Detournay ⁴⁶	22
2.16	The blister profile in a numerical expression is constant when flow rate remains the same. The front tip curvature is then a constant. Figure reproduced from Ball and Neufeld ⁵¹	25
2.17	The propagating blister is divided into two regions, A is the constrained region and B the deformed region.	26
2.18	Schematic of different flow behaviours for a Newtonian fluid and a shear-thinning fluid. n is the power law index.	27
2.19	Schematic of vapor tip dimensions. Figure reproduced from Moukhtari and Lecampion ⁴⁹	29
2.20	Modified fracture problem. The direction of x points from the fluid entry location to the faraway fracture tip. Figure reproduced from Adachi and Detournay ⁴²	31
2.21	Schematic of the flow behaviour of a yield stress fluids and a shear-thinning fluid. The main distinction is that a minimum shear stress is required to initiate flow of yield stress fluids.	33
2.22	Comparison of flow profile between fluids without yield stress (A) and with yield stress (B). The arrows indicate the local flow velocity. For normal fluids, the velocity decays as the location approaches the wall because of friction. For yield stress fluids there is a yielded zone where fluid flows and acts like a lubricant, and there is an unyielded zone where fluid is in a solid-like state.	34
2.23	Schematic of suspended particle migration caused by a co-effect of shear stress and normal stress in pipe flow.	35

3.1	Schematic of experimental set-up and sample structure. Pressure transducer reads and records the pressure at the entry of the fluid into the micro-channel; compressed air is used to pressurize the liquid in the syringe and push it into the model. (a) 3D structure of injection model, bright green ring indicates the edge of blister where separation happens; (b) T-shape mould used for templating the micro-channel in the base layer.	45
3.2	Profile of rough PDMS surface, a central line is determined so that the enclosed areas F_n above the central line is equal to the enclosed area below.	46
3.3	General image analysis of roughness and central line determination. A: Raw image. B: Profile outlined. C: Binary processing. D: Fixed coordinate. E: Area define and central line location, central line should be set so that the areas $F_1 + F_3 + F_4 = F_2 + F_4$	47
3.4	Microscopy of sample surfaces at varies spots	47
3.5	Schematic of adhesion measurement set-up. Compressed air is pumped in to pressurize the fluid, valve V1 encloses the air when closed and valve V2 stops the flow when closed.	49
3.6	Configuration of a sample, where l is the extended length, R is the radial length of blister edge, r is the constrained radial length, and h is the constrained height between gelatin and glass slide	50
3.7	Image analysis of blister profile. A is the raw image captured with camera and B is the binary image processed with ImageJ. Green curve shows the raw data extracted from B and black dashed curve is the fitting by a spline method using MATLAB.	51
3.8	Blister dynamic profile on flat surface at 5 psi. Legend shows different time intervals in different stages of the process. The black curve indicates that separation approaches its end.	52
3.9	Dynamic pressure with various compressed air pressures on a flat surface. All curves drop to a certain value at the late stage of separation.	53
3.10	Schematic of tissue occupying entry channel.	55
3.11	Blister profiles near the end of separation on a flat surface at three different initial pressure values.	56
3.12	Blister shape correction factor as function of time	56

3.13	Effect of total energy input on separation rate.	57
3.14	Adhesion is proportional to roughness. Data points are the average values of each trail, error bar indicates fluctuation of results on each surfaces.	58
4.1	Simplified eye lens model and schematic of cataract surgery process. Blue color represents injected fluid.	61
4.2	Schematics and dimensions of our hydraulic fracture model. Inside the blister is the fluid, at the front of the fluid is a vapor tip with no fluid inside.	62
4.3	Schematic of experimental set-up and sample structure. Pressure transducer reads and records the pressure at the entry of the fluid into the micro-channel; compressed air is used to pressurize the liquid in the syringe and push it into the model. (a) 3D structure of injection model, bright green ring indicates the edge of blister where separation happens; (b) T-shape mould used for templating the micro-channel in the base layer.	66
4.4	Curvature processing of blister profile. A: Raw image captured with camera. B: Binary image of A for quantification. Green color indicates experimental data extracted from B and black curve is the fitting by Equation (4.2). Curvature is taken at its maximum value.	67
4.5	Radius of water injection at three flow rates. Blacked dashed curves indicates the fitting of Equation (4.1). Left: original radius data. Right: radius adjusted to a log axis.	69
4.6	Normalised radius shows a trend of $t^{0.5}$ (black dashed line). Left: water injection. Right: 40% glycerin injection.	69
4.7	Equation describing the relationship between flow rate and blister profile. Left: whole profile calculated with four flow rates. Right: zoom-in of fracture front with normalized radii.	70
4.8	Blister profile depends on the viscosity and flow rate of the fluid. Left: Water and 40% glycerin injected at 0.2 mL/s. Right: profile of water injected at different flow rates.	71
4.9	Curvature as a function of flow rate. Inset: normalized curvature in a log coordinate showing that the dependency of curvature on flow rate follows $Q^{7/15}$	71

5.1	Flow curve of 0.1%, 0.5% xanthan gum and 40%g glycerin. The viscosity of xanthan gum increases as shear rate decreases, while for glycerin the viscosity is constant as it is a Newtonian fluid nature.	75
5.2	Schematics and dimensions of hydraulic fracture model	76
5.3	Schematic of experimental set-up and sample structure. Pressure transducer reads and records the pressure at the entry of the fluid into the micro-channel; compressed air is used to pressurize the liquid in the syringe and push it into the model. (a) 3D structure of injection model, bright green ring indicates the edge of blister where separation happens; (b) T-shape mould used for templating the micro-channel in the base layer.	79
5.4	Curvature processing of blister profile. A: Raw image captured with camera. B: Binary image of A for quantification. Green color indicates experimental data extracted from B and black curve is the fitting by Equation (4.2). Curvature is taken at its maximum value.	80
5.5	Normalized radius versus time for different fluids plotted in a log axis. The black dashed line indicates $t^{0.5}$	82
5.6	Microscope photos and curve of the fracture front of an advancing blister as the profile becomes increasingly steep, indicating an increased deformation with time. Tested with 0.1%xanthan gum at 0.23 mL/s. . .	83
5.7	Blister profile normalized by maximum radius to the same radius. The black dashed curve represents the theoretical fit from a bell-shaped curve theory.	84
5.8	Dynamic curvature as a function of blister fracture front propagation speed. Starting from fast velocity the curvature increases as velocity drops.	84
5.9	Theoretical profile of the fracture front calculated by Equation (2.6) with different tip lengths. The higher the tissue is lifted the more the tissue is deformed, as well as the longer the length would be. Inset shows longer length gives bigger curvature.	85
5.10	Rheology of 0.1% xanthan gum, 40% glycerin and water in the range of shear rate observed from our experiments. The viscosity of 0.1% xanthan gum has almost four-folds increase between the lowest and highest values.	87

5.11	Pressure loss and pressure gradient in blister for 40% glycerin and 0.1% xanthan gum. Inset is the pressure gradient of blister separated by 40% glycerin during the process. In the separation process the velocity keeps dropping.	87
5.12	Published data of dimensionless opening parameter $\bar{\Omega}_m$ and ζ_m extracted from Adachi and Detournay's paper. $\bar{\Omega}_m$ is obtained at power law index $n=0.6$, while n is determined from the rheology data of 0.1% xanthan gum. ζ_m value depends on n solely so we take also at $n=0.6$. ξ is the adjusted coordinate with $\xi = 1$ the location of the fracture front tip. n is the power-law index exponent.	88
5.13	Comparison between theoretical calculation of curvature and experimental data. The dashed lines denote theory, displayed with the left y-axis, and the flow rate increases at the same pace as the experimental data. The colored points are for experimental data displayed with the right y-axis.	89
5.14	Experimental data with numerically fitted theoretical calculations plotted in a log axis. The dashed lines represent theoretical curvature, from the bottom to the top the theoretical flow rate increases from 0.1 mL/s to 0.9 mL/s with a 0.2 mL/s increment. The red line indicates $\kappa = 0.51/mm$	90
6.1	Schematic contrasting the rheology of a yield stress fluid and shear-thinning fluid. A certain minimum shear stress is needed to initiate movement of static yield stress fluids.	95
6.2	Schematic representation of performance of different fracture fluids. A: attachment still exists between capsule and nucleus; B: small clearance and less fluid support; C: easy movement of nucleus blocks the entry; D: good support and sufficient clearance.	96
6.3	Comparison of velocity profile of shear-thinning fluids without yield stress (A) and with yield stress (B). The arrows indicate the local fluid velocity. For normal fluids, the velocity decays as the location approaches the wall because of drag. For yield stress fluids there is a yielded zone where fluid flows and acts like lubricant, and there is an unyielded zone where fluid is in a solid-like status.	97

6.4	Schematic of experimental set-up and sample structure. Pressure transducer reads and records the pressure at the entry of the fluid into the micro-channel; compressed air is used to pressurize the liquid in the syringe and push it into the model. (a) 3D structure of injection model, bright green ring indicates the edge of blister where separation happens; (b) T-shape mould used for templating the micro-channel in the base layer.	99
6.5	Curvature processing of blister profile. A: Raw image captured with camera. B: Binary image of A for quantification. Green color indicates experimental data extracted from B and black curve is the fitting by Equation (4.2). Curvature is taken at its maximum value.	100
6.6	Hydraulic fracture conducted with 0.1% Carbopol at a pH = 6.7 and 15 psi driving pressure. The profile shows an increase of curvature and the dynamic area shows the decrease of fracture rate at the front. . . .	102
6.7	Plot of the dynamic curvature changes during tissue separation with two yield stress fluids. In the beginning the velocity (fracture rate) is fast and the front has a small curvature. As velocity decreases the curvature keeps increasing to a discontinuous point where a sudden rise can be seen.	103
6.8	Schematic of yield stress fluid flow. The white zone is the yielded zone undergoing fluid-like flow and the grey zone the unyielded zone in a solid-like status. A-B: As velocity decreases, a smaller shear stress will cause a bigger unyielded zone to form and continuously weaken the flow capability. C: The increase of height has similar effects to a decrease of velocity and also makes the total flow more unyielded. . . .	104
6.9	Profile of the fracture front modeled with equation bending . $L = 0$ is the location of fluid front. The inset shows the curvature calculated by $\kappa = 2h/L^2$ as a function of the height.	105
6.10	Comparison of deformation between a shear-thinning fluid (0.5% xanthan) and a high normal stress shear-thinning fluid (0.1% HA). Without a normal stress, the shear-thinning fluid causes a dynamic increase of deformation on tissue during injection. With a normal stress the fluid deformation is balanced to be almost static.	106

6.11 Measured dynamic curvature for 0.5% xanthan gum and static curvature for 0.1% HA at different flow rates. 107

6.12 A: Normal stresses of 0.1% HA and 0.5% xanthan gum obtained from rheological data. B: Pressure drop along the blister at varying velocity. C: Total pressure loss during separation with 0.1% HA. D: Total pressure loss during separation with 0.5% xanthan gum. C,D insets: schematics of stresses distribution during separation for two types of normal stresses. 108

List of Abbreviations

$\dot{\gamma}$	Shear rate
κ	Curvature
μ	Viscosity
σ_0	Compression stress
σ_N	Yield stress
τ	Shear stress
τ_0	Yield stress
B	Bending stiffness
E	Elasticity (Young's modulus)
E'	plane-strain elastic modulus
G	Adhesion strength
h	Blister height
h_c	Constrained height
l	Blister extension length
M	Power law consistency
n	Power law index
P	Pressure
Q	Flow rate
q	Blister shape correction factor
R	Blister radius
V	Velocity (fracture rate)
ν	Poisson's ratio

BSS	Balanced salt solution
CBT	Constrained blister test
IOL	Intraocular optical device

Chapter 1

Introduction

The eye is one of the most delicate components of the human body. One of the most severe consequences of eye disease is blindness. A cataract causes clouding of the lens of the eye, or sometimes adjacent fluids. Cataracts are responsible for almost half of worldwide blindness¹. Surgery to remove cataracts is the most common elective surgical procedure around the world, including Australia. In 2014 - 15 almost 700,000 patients were admitted for elective surgery in public hospitals, 65,000, or slightly more than 9%, were for cataract surgery. If we include private hospitals, in 2014-15 there were 245,797 hospitalisations for cataract surgery. This group represents 1% of the total population but 22% of the population over 65 years of age². Blindness caused by cataract is a physical transformation that can not be reversed by use of drugs or by biological response. The physiology and structure of the eye and the mechanism of cataract formation must be understood in order to address how to treat cataracts³. Fundamentally, treatment of cataracts is carried out by surgical removal of the clouded lens, then replacement by insertion of an artificial lens. In the removal process, fluid is used to create interfaces between eye lens tissues and enlarge the gaps resulted from such fracture. It is the most critical process in the surgery, and the fracture behavior depends on the flow properties such as flow rate and velocity, and fluid properties such as viscosity and shear motion. Besides, such fracture is related to the breakdown of biological adhesion between eye lens tissues, but this adhesion strength is not fully measured. Therefore

it is interesting to study in details how these properties affect the fracture process and how the surgery can be further optimized accordingly. Also it is worth explore possible ways to measure biological adhesion.

To achieve the goals, this thesis is separated into six chapters.

In Chapter (2), background information for eye lens, tissue adhesion, and fluid-induced hydraulic fracture is presented.

In Chapter (3), adhesion of the experimental model is measured, which provides insights into the use of the measurement technique for a model eye lens.

In Chapter (4), the fracture behaviours of Newtonian fluids are discussed to quantify the effectiveness and safety of separation process and the dependency on fluid rheology.

In Chapter (5), effectiveness and safety of separation using shear-thinning fluids are studied, allowing general guidelines for optimized surgery processes.

In Chapter (6), the effects of more complex rheology properties, including yield stress and normal stress fluids, on separation are discussed. The work provides useful insights into the benefits of manipulating rheology properties to optimize real cataract surgery.

In Chapter (7), key findings of this thesis are summarised, and future directions are suggested to enable further studies in this area.

1.1 References

- [1] G. Tabin, M. Chen, L. Espandar, *Current opinion in ophthalmology* **2008**, 19, 55–59.
- [2] AIHW, *Elective surgery waiting times 2014-15 : Australian hospital statistics*, Australian Institute of Health and Welfare, Canberra, **2015**.
- [3] L. A. Remington, D. Goodwin, *Clinical anatomy of the visual system E-Book*, Elsevier Health Sciences, **2011**.

Chapter 2

Literature review

2.1 Structure of the human eye and lens

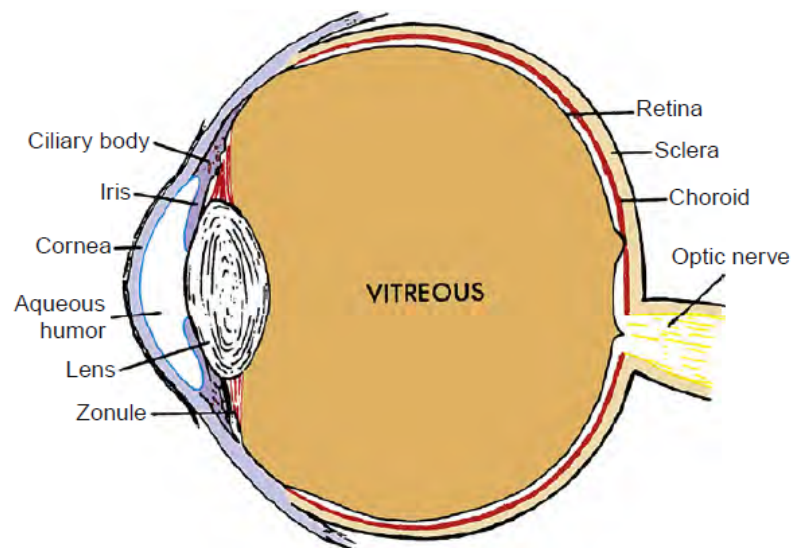


Figure 2.1: Structure of the human eye. The lens is located posterior to the aqueous humor and iris, and anterior directly to the vitreous. The primary function of the lens is to focus light going into the eye and project it onto the retina. The zonular fibers merge to the whole equator region and part of the anterior and posterior regions. Figure reproduced from Remington and Goodwin¹.

The human eye is essentially a biological archetype of a camera (Fig.2.1). In a functional eye, when light is projected to the eye, it will go through cornea, iris and pupil and be focused by the eye lens. After this the light is projected to the retina, received by the nerves, and translated into signals that the brain can read. By this process an image is generated. The lens is located anterior to the vitreous

chamber and posterior to the iris¹. Zonule fibers are attached to the equator region of lens on one end and to the muscle on the other end. The elasticity of eye lens allows it to be deformed in order to alter the dioptric performance, enabling clear vision at different distances. A close look at the eye lens reveals an extremely fine microstructure.

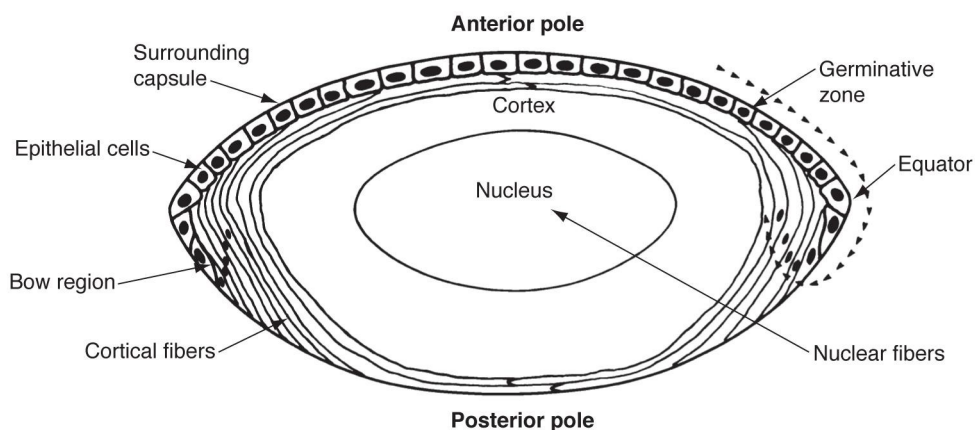


Figure 2.2: Structure of the eye lens. The capsule is a thin layer of fiber surrounding the whole lens. Posterior to the anterior capsule is the single-layer epithelium. Inside this onion-like structure are the cortex and nucleus, which are the lens fibers differentiated from early epithelium. Figure reproduced from COURSE².

The lens is a biconvex, avascular body (Fig.2.2). Considering it as an elliptical structure, the lens has a thickness of 3.0 – 4.6 mm and diameter of 8.4 - 9.9 mm. Both dimensions are age-dependent, however, and the lens thickness increases by an average of 0.02 mm throughout a person's lifetime. Diameter matures and reaches its maximum during a person's teenage years³⁻⁵. For the purposes of cataract surgery research, the lens can be considered to consist of three main components: the capsule, the cortex and the nucleus (Fig. 2.2).

The capsule is a transparent vessel containing the whole lens. It is a highly elastic membrane consisting of fibers arranged in a lamellar pattern¹. Lens elasticity is age- and strain-dependent: at low strain elasticity increases until age 35 and then

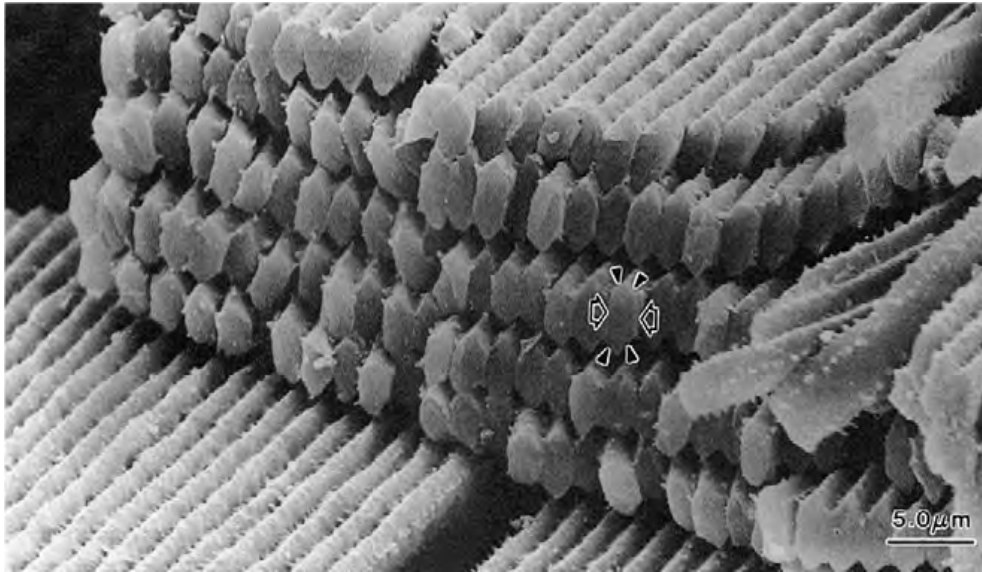


Figure 2.3: Cross-sectional profile of lens capsule fiber cells. The cells are arranged in a hexagonal pattern. The capsule has an onion like structure consisting of layers of fiber cells. Each of these layers is made up of adjacent fibers. Figure reproduced from Adler⁶.

stabilises, while at high strain it decreases with age⁷⁻⁹. The capsule exterior is surrounded by zonular fibers, mostly on the equator regions. The zonule merges to the capsule, stretches and accommodates it. Inside the capsule there is a one-layer epithelium. These cells can only be found at the anterior of the lens. The absence of epithelia at the posterior is because these cells formed the capsule fiber during embryo development. At the anterior, cells are in a cuboidal shape and arranged in a honeycomb pattern (Fig.2.3). At the equator, the cells are gradually elongated to cover the inside of the capsule. The epithelium continues to have cell mitosis throughout its lifetime, and the old cells will gradually lose cellular organelles and differentiate into lens fiber. The above process causes the aforementioned age-dependency of the lens capsule thickness and elasticity¹. According to Adler and Krause⁶, the lens fibers pile up on the outside of the epithelium and the cross-sectional profile has a honeycomb pattern¹⁰. The resulting structure of the interface

between the cell layers has a significant microscale roughness. Though the capsule fiber and the epithelium are not the same cells, they are all considered connected components of the lens capsule, a very thin membrane with a thickness on the order of single cells.

The lens capsule surrounds the lens core: a two-part structure in which a nucleus is enclosed in the cortex. These are all formed by lens fibers differentiated from epithelia. Starting from the embryonic period till the end of the teenage years, the lens fibers that form the mature cortex and nucleus will gradually become an onion-like structure. The resulting structure consists of several layers of fibers. The difference between cortex and nucleus is the period in which they are formed. Viewed in cross-section, the interfaces between nucleus, cortex and capsule are all rough structures as a result of the hexagonal fiber packing (Fig.2.3 2.4 2.5 2.6). The hexagonal shapes are normally $3\ \mu\text{m} \times 9\ \mu\text{m}$ with an angle of 60° . The morphology is important to the lens-capsule separation process during cataract surgery Although more detail is possible, for our practical purposes the cortex and nucleus can be considered together as a single entity.

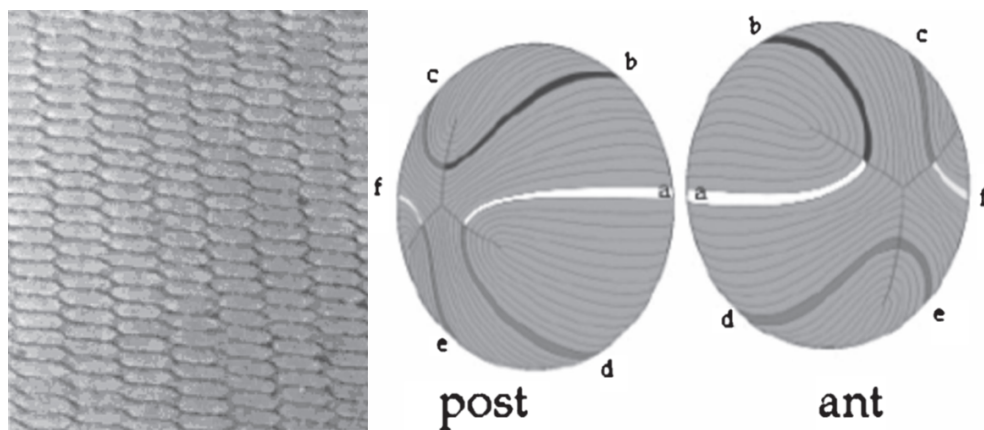


Figure 2.4: Left: SEM photo of nucleus lens fiber cross-sectional profile. Figure reproduced from TROKEL¹¹. Right: Onion-like structure of nucleus and cortex fibers arrangement. Figure reproduced from Aliò et al.¹².

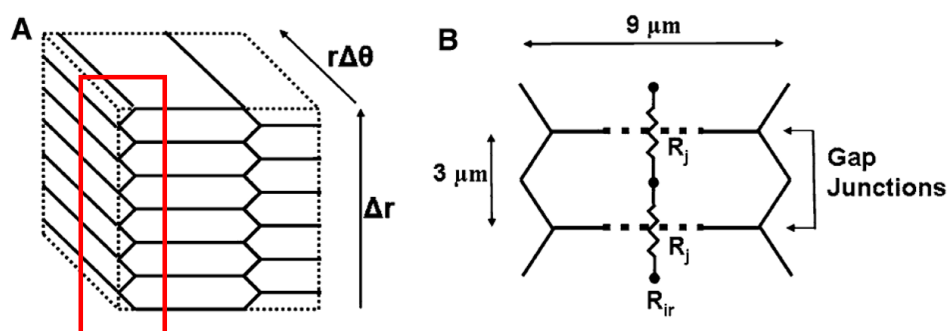


Figure 2.5: Configuration of fiber cells showing that each element has a $3 \mu\text{m} \times 9 \mu\text{m}$ dimension. The angle of sides between two gap junctions is 60° and is not shown precisely. Morphology of layer-layer interface is outlined with red square. Figure reproduced from Mathias et al.¹³.

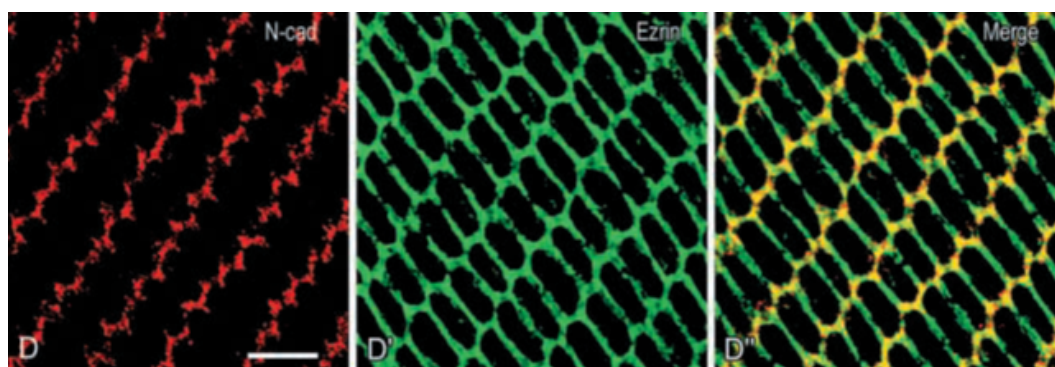


Figure 2.6: Immunofluorescence microscopy shows the hexagonal cross-sectional profile of the lens fiber cells. The red color is the location of cadherin, the green color indicates the ezrin-based complex, the framework of fiber cells. The third image merges these two components and shows the overall distribution of the two different complexes. Figure reproduced from Straub et al.¹⁴.

Many groups have studied the morphology of layers consisting of lens fiber tissues^{1,12,13}. A study based on bovine eye lens fibers has also observed hexagonal ordering of lens fibers (Fig.2.6 (D'')) using fluorescent microscopy of tagged adhesion complexes. Cadherin is associated with several other cell proteins and enable visualisation of the adjacent cell connections. In addition to likely providing inter-fibre adhesion, the protein also enables cortical-capsule adhesion and cortical-nucleus adhesion¹⁴.

2.2 Cataract surgery

Cataracts cause eye lens opacity and can account for as much as half of global blindness¹⁵. Cataracts can have various causes that affect the metabolism of the eye lens such as aging, disease and genetics, although aging is the most common cause¹⁶. Continuous lens growth caused by epithelium division causes the increase of eye lens capsule thickness and degradation of lens mechanical properties^{7,17}. Cataracts can be located in the nucleus or the cortex, and surgical intervention is not typically able to distinguish, requiring removal of the cortex and nucleus together.

Chemical mechanisms of cataract formation are thought to be:

- Osmotic imbalance in fiber cells
- Oxidative caused by free radical damage
- Protein modification
- Metabolism disturbance

All of these contribute to an irreversible failure, requiring removal and replacement of the eye lens¹⁸ via cataract surgery treatment.

In a cataract surgery (Fig.2.7), the anterior capsule is opened by the capsulorhexis method, involving cutting a 5 mm entry point and gently lifting the anterior capsule to create an initial gap between the capsule and cortex. A fluid is then injected into this gap, building hydraulic pressure that separates the two tissues. Depending on the fluid used this process is known as either hydrodissection (balanced salt solution, BSS) or viscodissection (high molecular weight hyaluronic acid solution)¹⁹. Normally hydrodissection is sufficient to remove the epithelium, cortex and nucleus. However tissues can sometimes remain attached to the capsule even after

several attempts. If so, the next step is to apply viscodissection. Once the adhering tissue is removed the lens cortex and nucleus are broken up using ultrasound, a process known as phacoemulsification, and the fragments removed by suction. The last step is to insert a silicon-based artificial intraocular lens (IOL) inside the capsule.

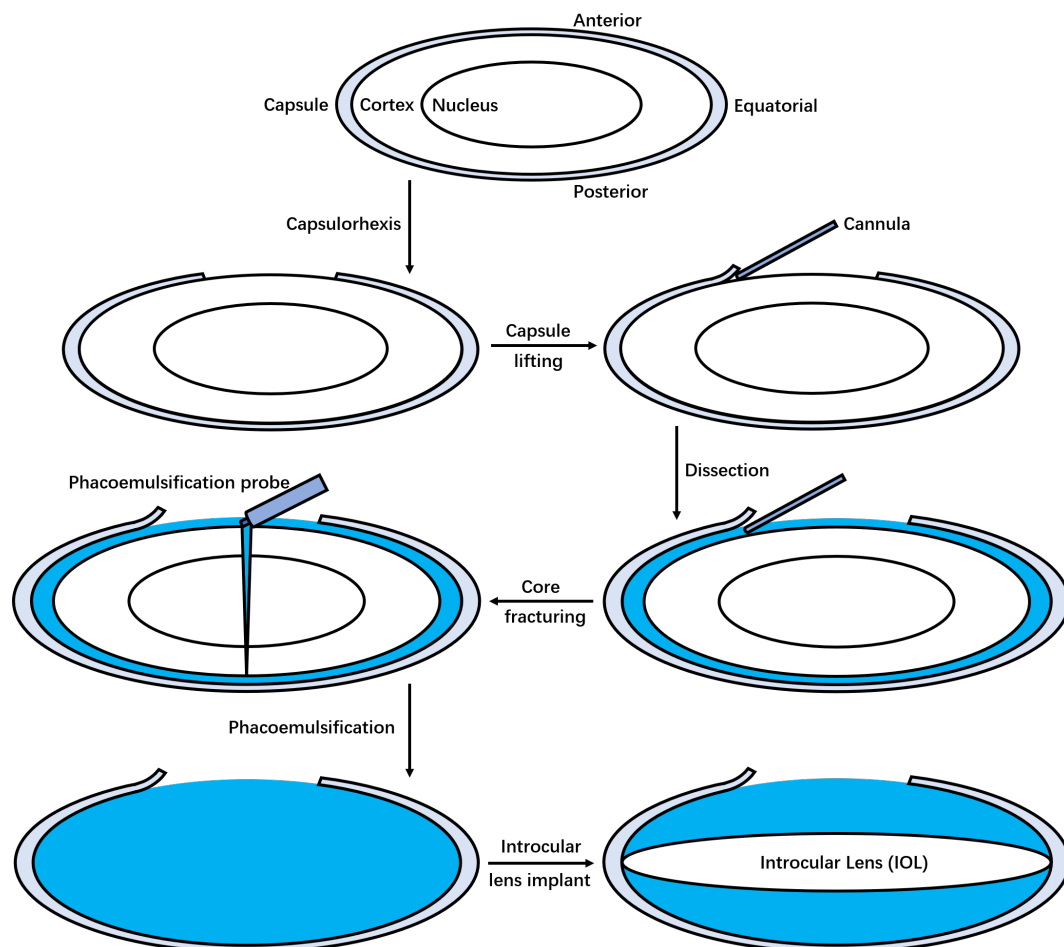


Figure 2.7: The general process of cataract surgery. Here the lens is portrayed as a simple elliptical shape. The outer layer (grey color) is the capsule, the epithelium layer is located between the cortex and capsule and is not shown as it is quite thin. Not all dimensions are to scale.

Hydrodissection is the most basic approach to separate interfaces between capsule, cortex and nucleus and injections can be performed at single or multiple sites.

There are several concerns about hydrodissection. During the injection, hydraulic pressure may build up near the posterior pole region, causing a bulge and pushing the nucleus toward the anterior, blocking the entry and the ability of the injected fluid to exit²⁰ (Fig.2.9 (B)). A build-up of pressure puts stress on the capsule and zonules and risks catastrophic rupture. Multi-quadrant injections can be more effective at separating tissues (Fig.2.8)^{21,22}, but can add risk versus single injection. Fortunately posterior capsule rupture due to hydrodissection is rare but the complex deformation of the elastic capsule material could permanently alter its mechanical properties and not much is known.

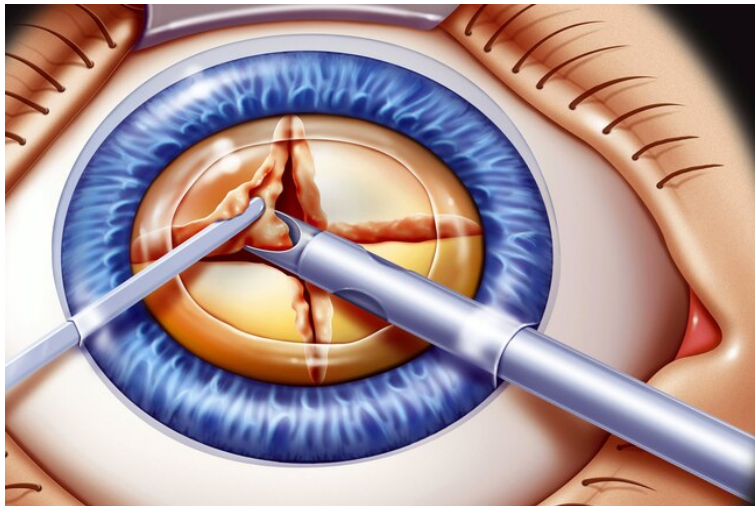


Figure 2.8: Multi-quadrant fracture of the eye lens nucleus. Figure reproduced from WebMD²³.

Phacoemulsification prepares the delaminated nucleus and cortex for removal. The lens is fractured and dispersed by ultrasonic energy and then aspirated from the eye. A special probe is used to do both aspiration and irrigation in order to supplement the fluid being aspirated along with the fractured lens, maintaining space in the capsule. During phacoemulsification, ultrasound energy is significant, while 250 to 500 Hg vacuum pressure is applied along with up to 25 cc/min irrigation flow rate¹⁹. Success of phacoemulsification requires the nucleus to be

at a location with no attachment to the capsule, and there must be enough space between them to allow rotation and movement of the nucleus²⁰ (Fig.2.9 (A,D)). Such space is achieved better by viscodissection than hydrodissection as the more viscous fluid better maintains the separation¹⁹. When the low-viscosity BSS is used alone for nucleus division and sculpting, most of the fluid leaks out, leaving only a small space to cushion nucleus removal (Fig.2.9 (B)).

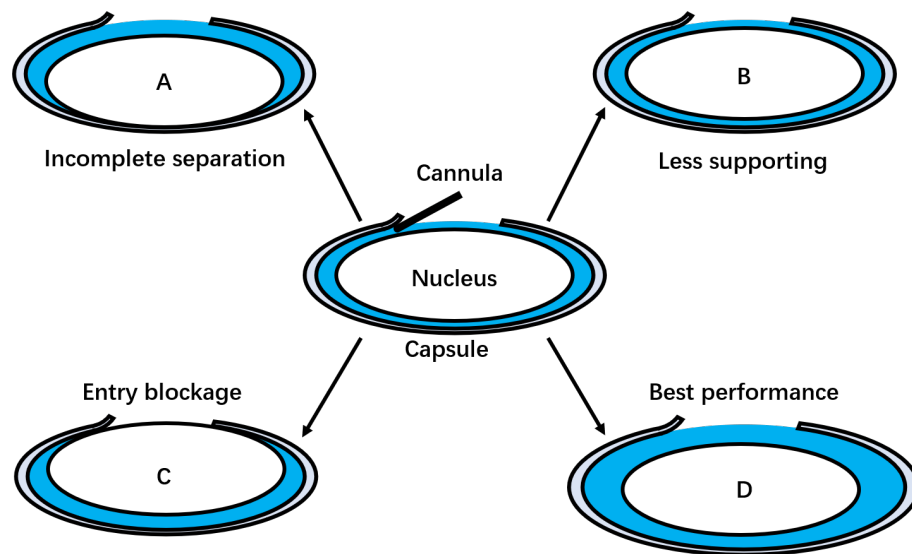


Figure 2.9: Performance of fracture fluids. A: attachment still exists between capsule and nucleus; B: small clearance and less fluid support; C: easy movement of nucleus blocks the entry; D: good support and sufficient clearance.

Viscodissection provides and maintains a larger gap even when used with hydrodissection during phacoemulsification. This indicates the importance of the rheology of the fluid used during surgery, as multiple functions are needed for success. The hyaluronic acid solution used during viscodissection has a non-Newtonian, shear-thinning behavior that can be tuned by adjusting concentration, interaction, and molecular weight. The details of fluid rheology and flow and their impact on surgical success has not been studied in great detail and a key motivation of this thesis is to better quantify such effects in a way that can both explain the success

of current materials and enable any possible design improvements in future formulations. We are interested in the effects of viscoelasticity, or the complex flow and memory effects of polymer solutions, on tissue separation and deformation. For example, sudden increase in fluid pressure during dissection could cause dangerous irreversible tissue rupture, but the viscodissection fluids used likely thin when injected but recover viscosity and maintain separation where needed during core removal. Doing so on the time scale of insertion of the replacement lens is a key design parameter for cataract surgery. A commercial product DisCoVisc has a strong cushioning effect during surgery, but does not enable removal of any epithelium that remains on the capsule. Any cells left behind can cause a postoperative complication called posterior capsule opacification (PCO), where the epithelia grow rapidly and encroach on the visual axis, causing light scattering and secondary visual loss²⁴. It is therefore essential to remove epithelium during surgery, and for this task the less viscous viscodissection materials are more effective at cortical-cleaving for epithelium removal²¹.

During separation and removal of tissues inside the eye lens, it is essential to overcome the biological adhesion between layers. An important target for fluid cleavage is corticalcapsular adhesion, referring to the attachment between cortex and capsule. A “furry” epinucleus surface is observed in 20% of patient cases, and refers to a nucleus surface with higher surface area structures that have stronger adhesion, making hydrodissection more difficult. Adhesion is divided into three kinds depending on the location: anterior, posterior and equatorial. These three types exist either alone or together, while equatorial adhesion occurs in most patients. Studies indicate that adhesion can often remain after single-site hydrodissection, and sometimes even after multiple single-site hydrodissection²⁰. It is reasonable to

assume that such adhesion also exists between nucleus and cortex because of the similarity of these tissues. For this work we focus on the corticalcapsular adhesion.

For hydrodissection and viscodissection there has been no quantification of effects of operation parameters such as injection flow rate, pressure, and fluid properties on surgery performance. It is generally believed that a small amount of fluid is a safe choice for surgery, so conventionally a 2 mL syringe is used to limit the volume of fluid used in both methods. Nearly all studies about safety concerns and operation effectiveness in surgery are based on either capsule rupture rate or a subjective grading method. When removing posterior polar cataract (PPC), the rupture rate can be as high as 36%, and surgery is of higher risk when there is an associated pre-existing posterior capsule defect^{25,26}. Also, for all documented ruptures, 61% are caused by mishaps during phacoemulsification²⁷. The physiology change of capsule tissue due to growth of the cataract may be one reason. Cortical cataracts can cause the cortex to be extremely hydrated, which may make the tissue more fragile²⁸. Since the lens fibers that comprise cortex and capsule are essentially the same and the only difference is their shape, there may be similar variations happening. The posterior capsule is the thinnest in the eye lens, which could also contribute to the occurrence of rupture. A more quantitative approach to understanding and mapping the limits of hydraulic tissue separation is needed to connect the above phenomena and increase the safety of cataract surgery.

2.3 Eye lens bio-mechanics

In cataract surgery, the biggest safety concern is that the deformation caused by injection of fluid may cause damage to the tissue, either loss of elasticity and/or rupture. It is then important to know the bio-mechanics of the eye lens, such as the maximum stress and strain the lens can endure. The mechanical properties of

related tissue have been studied, and knowledge of the lens capsule thickness, radius of curvature and low bending stiffness is used to construct a membrane model description²⁹.

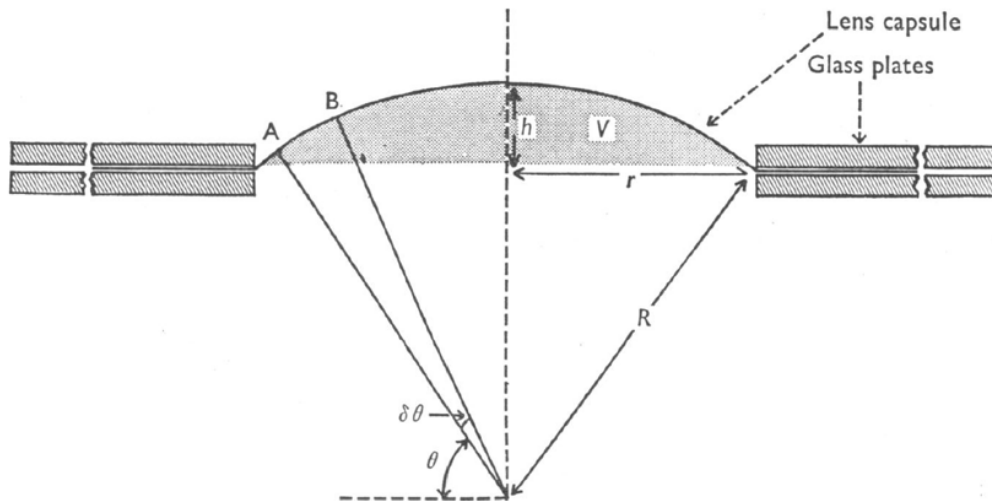


Figure 2.10: A bulge elasticity measurement. The anterior capsule is cut to a round shape and clamped at the aperture between two glass slides. The fluid is pressurized at one side of the capsule, causing deformation bulging. The radius of curvature of the bulge, R , pressure change due to change of volume P , initial volume of capsule V , thickness of capsule t and Poisson's ratio ν are then used to calculate elasticity: $E = \frac{3}{2} \frac{PR}{t} (1 - \nu) V$. Figure reproduced from Fisher⁸.

The elasticity of a material is usually tested by measuring its deformation response to a gradually increased stress. An example is a measurement of the bulging deformation of a mounted flat tissue when exposed to pressure from one side (Fig.2.10). The pressure, volume and shape of the bulge are then recorded to calculate the elasticity^{8,30}. The main problem with this method is potential damage to the capsule when it is clamped in place, causing bias and rupture that does not represent the actual material properties. Inhomogeneities in the tissue can also affect accuracy. The tensile deformation of capsule tissue has also been tested by cutting a ring of tissue and stretching it on two pins (Fig.2.11). The test in Fig.2.11 is advantageous as it better provides uniaxial deformation^{7,17}.

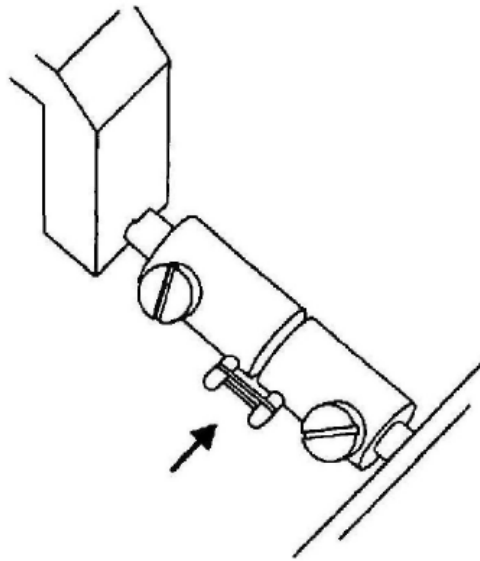


Figure 2.11: Capsule tissue tensile test. Arrow indicates ring-shaped specimen. The lens capsule is extracted from the eye and cut to a capsule ring along the equatorial region for measurement. It is then fixed by two pins on the probes and stretched. Figure reproduced from Krag and Andreassen⁷.

Fisher found that the Poisson's ratio is about 0.47 for all eyes tested. The test typically assumes the lens capsule is in-compressible and linear elastic⁸. Measurements indicate the Young's modulus in children is around 6×10^7 dyn/cm², and drops to 3×10^7 dyn/cm² at age 60 and 1.5×10^7 dyn/cm² over age 90⁸. These findings provide a basis for modeling flow and tissue deformation during surgery.

More recent work indicates the eye lens capsule actually has a non-linear elasticity¹⁷ that decreases with age. Tissue thickness increases with age, from 11 to 33 μm at the age of 75 and then drops slightly. The yield strain, the amount the capsule can be deformed before being broken, decreases linearly from 108% in infants to approximately 40% in elders (Fig.2.12). The thickness of the eye lens plays a critical role in determining the mechanical properties of the capsule tissue.

Another study³⁰ found that capsule tissue is not homogeneous and varies in thickness depending on location with an average of 16.7 μm . They reported a yield

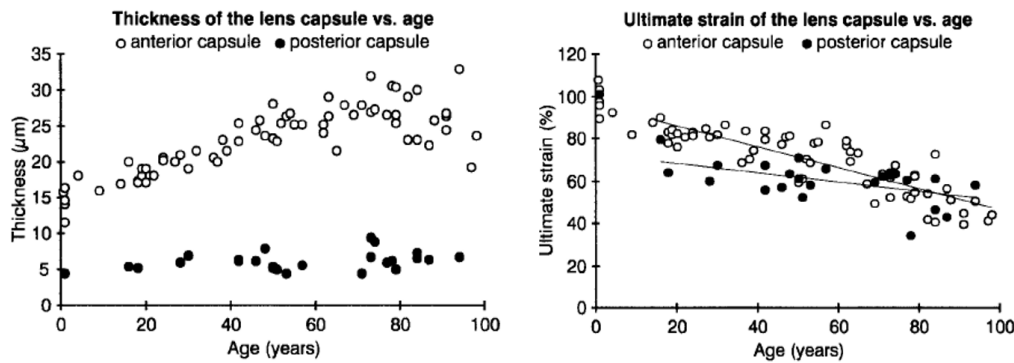


Figure 2.12: Thickness of capsule increases with age until age 75 and then drops slightly. The posterior is the thinnest part and shows an almost constant value. The yield strain decreases continuously from over 100% to about 40% in elders. Figure reproduced from Krag et al.¹⁷.

strain of 29.4% and a yield stress of 1.36 MPa, in good agreement with previous work^{8,17}. The age-related increase in capsule fragility makes deformation easier but more difficult to predict and more sensitive to the pressure and force used during cataract surgery. Understanding of the extremes of behaviour possible in surgical situations is essential to ensure safety.

Regardless of the nature of eye lens capsule, surgery will affect tissue mechanical properties in various ways. In cataract surgery, optical reflection is required to visually inspect the condition of the lens. When not feasible surgeons use dyes to improve the contrast. One dye, trypan blue can have negative effects on anterior lens capsule elasticity: increasing stiffness by 47% and decreasing yield strain by 13% for capsules with thickness 10 µm³¹. Given the variability of the tissue mechanical properties, it is useful to have a more consistent framework to model and discuss its expected behaviour during surgery.

As part of this work, we wish to develop an analogue soft material that can be used to study fluid-induced separation of adhesion. The lens capsule mainly consists of a network of type IV collagen³⁰, so we use its properties as a basis for

our experimental design and studies. We choose gelatin, a natural polymer sourced from collagen as a key part of our analogue tissue setup. Benefiting from Krag and Andreassen's and Dick *et al.*'s findings, we set $40\% \times (100\% - 13\%) = 35\%$ as a safe upper limit of strain deformation for patient cataract surgery.

2.4 Blister test

Our study of the physical aspects of cataract surgery requires two main elements:

- An easily accessible model to mimic the eye lens capsule environment. As we focus on mechanical properties and deformation, we choose to use reproducible analogues rather than biological tissues.
- An experiment that allows study of hydraulic pressure effects on adhesion and separation while documenting hydrodynamics that mimic those of cataract surgery.

Many techniques have been developed to study adhesion breakdown, and examples include peeling, stretching, three-point bending, blister tests. We examine them each in turn to choose the appropriate method. The peeling test is most widely used to measure adhesion in biological tissues. Marmor tested the adhesion of retina tissue by peeling it off retinal pigment epithelium³². Peeling has also been used to study carotid bifurcation tissue adhesion strength³³, as well as blocks of cell masses^{34,35}. Peeling tests require tissue that is sufficiently large and strong to be clamped and held for testing without damage. Stretching tests have similar requirements, while three-point bending tests require fairly large sample sizes. Eye lens capsule tissue is small, thin, and fragile, making the above methods infeasible. A better method mimics the flow used to cleave tissue in surgery and harnesses it to measure applied stress without damage. The blister test meets these requirements

as it closely resembles the key aspects of cataract surgery. The blister test was first proposed by Dannenberg who pumped mercury into the gap of a specimen, measured the pressure and volume of mercury that was injected, and calculated the adhesion energy³⁶.

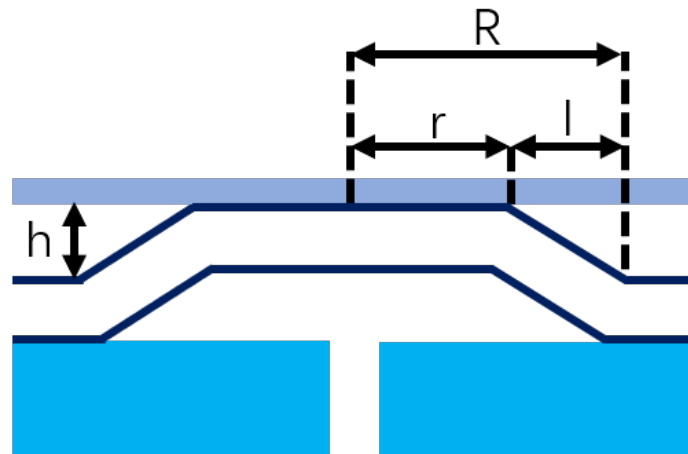


Figure 2.13: Configuration of a blister test sample. Here l is the extended length, R the radial length of the blister edge, r the constrained radial length, and h the height between gelatin and glass slide.

A standard blister test injects fluids or air into a gap between substrate and attached film, forming a blister and thus separating the adhering surfaces (Fig.2.13). The blister test avoids issues with clamping or other sample preparation, requires only minimal modification of the sample to allow application of pressure, provides a direct measure of deformation³⁷, and allows good resolution of small deformations while avoiding excessive dissipation of energy³⁸. As the eye environment limits the extent of tissue movement during surgery, we apply the constrained blister test (CBT) by carrying out separation studies between two rigid surfaces that set a maximum vertical strain. The CBT pressurises the analogue tissue-substrate system with liquid via a small entry hole and allows documentation of the rate of blister volume growth as the two surfaces separate.

Adhesion measurement by blister test is carried out using an energy balance³⁹⁻⁴¹:

$$G = \frac{dW_{ext}}{dA} = P \cdot \frac{dVol}{dA} = P \cdot h \cdot q \quad (2.1)$$

The adhesion G is characterised by the total external energy input to create new interfacial area A , which equals to the product of pressure P and volume of fluid injected $dVol$. Practically, the external energy dW_{ext} would be consumed in many forms such as tissue deformation, elastic and kinetic dissipation during fast separation. In a constrained blister test we are able to minimise the effect of other forms of energy as much as possible so that external energy input is mainly consumed by adhesion breakdown. In theory the adhesion is characterised by the total external energy input to create new interfacial area, equal to the product of pressure P with the volume of fluid injected $dVol$. When difficult to measure the volume of fluid injected, a shape correction factor q is used to correlate the pressure and the gelatin layer height^{39,40}:

$$q = \left(1 - \frac{l}{2R}\right) + \left(\frac{l}{3R} - \frac{1}{2}\right) \cdot \frac{dl}{dR} = \frac{1}{2} + \frac{r}{2R} \quad (2.2)$$

where l is the extended length of blister, R is the blister radial length and r is the radial length of blister top in contact with the glass slide constraint (Fig.2.13). Often, the change in extended length is too small so that $\frac{dl}{dR}$ is much smaller than the other terms so it can be neglected. Therefore the equation is transformed to the first right-hand side term related to the two radial lengths and not the separation dynamics. Using pressure, blister height, and the geometric correction factor, it is straightforward to calculate the value of adhesion in an experiment.

2.5 Fracture mechanism

Hydraulic fracture of soft tissue in this project can be considered a formation of a blister and a subsequent peeling of a soft elastic sheet by a pressure-driven fluid flow (Fig.2.14). The fluid is injected at a constant flow rate Q by a constant pressure P_d . As fluid is injected, the adhesion between two layers is broken down, and the top layer with thickness d is lifted to height H till it touches the constraint as a fixed height of h_c . The setup enables quantification of deformation at the fracture front. As separation occurs, there exists a vapor tip l between the fluid front R_F and the blister fracture front R . The pressure in the lag tip P_t is considered to be zero as it forms in a volume sealed by fluid influx. As l/R is very small, it is generally considered that $R_F \equiv R$. Conditions in the tip are set by the balance between the compression stress σ , that is normal to the soft sheet, and the pressure of the fluid P_f .

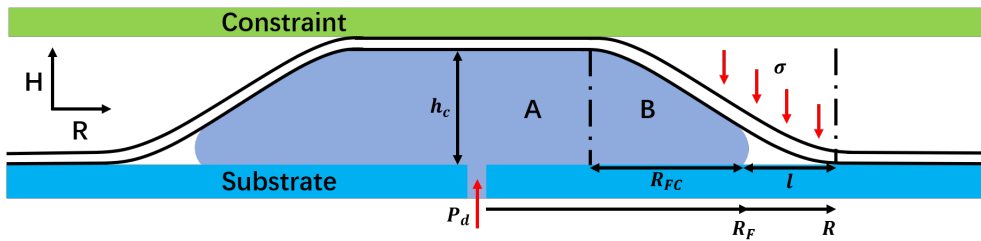


Figure 2.14: Separation system is divided into a stabilized region (A) where no deformation occurs, and a deforming region (B). Part of region B is fluid-filled and the rest is a vapor tip region. l is the peeling length scale of Equation (2.17) that represents the magnitude of the vapor tip, R_F is the length of the fluid-filled deforming region. σ is the compression stress normal to the soft tissue.

Based on this model, the blister is divided into two parts, known as the fluid-filled and the fluid vapor tip regions, and different theories govern their behaviour. The vapor tip is a practical description that avoids a description of infinite pressure at the blister tip⁴² and allows numerical mass conservation using lubrication the-

ory descriptions of the flowing fluid and elasticity theory descriptions of material deformation at the vapor tip where separation occurs.

The main equation in lubrication theory is Reynolds Equation⁴³, which describes: (1) Newtonian fluid flow, (2) negligible fluid body force and inertia force, (3) laminar flow, (4) a negligible pressure gradient across the film thickness, and (5) a small fluid film thickness⁴⁴. A simple form ignores any squeezing of fluid by the film, giving a relationship between pressure P , height of tissue lifted h , viscosity μ and local velocity V as:

$$h^2 \frac{dP}{dx} = 12\mu V \quad (2.3)$$

The Reynolds Equation can be extended to describe a power-law fluid using⁴⁵

$$\tau = M\dot{\gamma}^n \quad (2.4)$$

$$\frac{dP}{dx} = 2^{n+1} \left(\frac{2n+1}{n}\right)^n \frac{MV^n}{h^{n+1}} \quad (2.5)$$

where M and n are the power-law consistency and index respectively. Make $M = \mu$ and $n = 1$ for Newtonian fluids then Equations (2.3) and (2.5) are interchangeable.

In the vapor tip region, the hydraulic pressure essentially performs a basic peeling test fracture. A continuity exists that allows the pressure obtained by the Reynolds Equation to be fit to the beam bending theory. The minimum element of the bending fits the pressure at the fluid front to:

$$B \frac{d^4 h}{dx^4} = P \quad (2.6)$$

where B is the bending stiffness of the tissue calculated by Young's modulus E , tissue thickness d and Poisson's ratio ν .

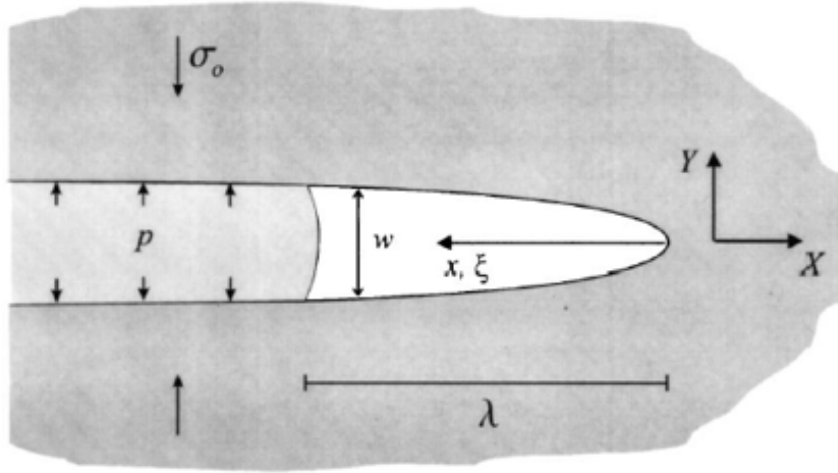


Figure 2.15: Schematic of a typical hydraulic fracture in a general material with the assumption of a fluid vapor tip. Figure reproduced from Garagash and Detournay⁴⁶.

$$B = \frac{Ed^3}{12(1-\nu^2)} \quad (2.7)$$

Combining Equations (2.3) and (2.6) gives a more generalised form that relates the pressure, height, bending stiffness and velocity of fracture front:

$$h^2 \frac{d^5 h}{dx^5} = \frac{12\mu V}{B} \quad (2.8)$$

Solving this equation and modeling the scale as well as the governing factors of general hydraulic fracture, Garagash and Detournay requires a dimensionless analyses using the vapor tip height w and size λ , which can later be used to analyse the deformation of material at the fracture front (Fig.2.15).

$$w = \epsilon L_\mu \Omega, \quad \lambda = L_\mu \Lambda, \quad \epsilon = \sigma_0 / E' \quad (2.9)$$

where ϵ is a dimensionless height correction parameter, L_μ is the characteristic length scale of viscous dissipation, and Ω and Λ are the dimensionless crack

opening and size, respectively. $E' = E/(1 - \nu^2)$ is the plane-strain elastic modulus. Depending on the five dominating parameters: viscosity μ , fracture velocity V , compression stress σ_0 , plane-strain elastic modulus E' and fracture toughness K_{Ic} , these equations can be solved to fit different criteria^{42,47-51}.

2.5.1 Newtonian fluid hydraulic fracture

Garagash and Detournay provides a theory for general hydraulic fracture, which can be adapted to a blister geometry in which an adhered elastica is bulged off a rigid substrate by Newtonian fluids. In this scenario, the fracture toughness is limited to a very small value approaching zero, and the viscosity of pressure-driven fluid is constant. Two recent papers published by different groups Wang and Chung, Ball and Neufeld proposed the same theory, both concluding that at low toughness the fracture of elastic tissue is dominated by the fluid viscosity (Fig.2.14) and can be described by Equation (2.9).

Using the lubrication approximation, the blister central deflection is⁵²:

$$\frac{\partial h}{\partial t} = \frac{1}{12\mu} \nabla [h^3 \nabla (B \nabla^4 h + \rho g h)] \quad (2.10)$$

and according to flow rate-dependent mass conservation:

$$Qt = 2\pi \int_0^{R_F(t)} h(r, t) r dr \quad (2.11)$$

For low flow rates and quasistatic deformation with a free moving surface, the profile of the blister can be written as⁵⁰:

$$h(r, t) = \frac{3Qt}{\pi R_F^2(t)} \left[1 - \frac{r^2}{R_F^2(t)} \right]^2 \quad (2.12)$$

The fracture front curvature is then:

$$\kappa = h''(r, t) = \frac{24Qt}{\pi R_F^4} \quad (2.13)$$

We are particularly interested in the curvature of the fracture front, as this relates the degree of deformation the elastic material experiences and can thus be tied to the potential danger of tissue rupture. For a constrained blister test as we use here, the blister has a region where there is no longer a free surface and the blister shape is described by a frustum profile. Adjusting $h_c = 3Qt/\pi R_F^2(t)$ and $R_{FC} = R_F$ gives:

$$h(x) = h_c \left[1 - \frac{r^2}{R_{FC}^2(t)} \right]^2, (x = r) \quad (2.14)$$

Adapting this with Equation (2.13) gives the representative of curvature for a frustum at $r = R_F$:

$$\kappa = h''(r, t) = \frac{8h_c}{R_{FC}^2} \quad (2.15)$$

For peeling of an elastic film off a rigid substrate without a pre-wetting fluid film, at the tip of the blister there are two characteristic length scales of the vapor tip, the natural and peeling length scales, respectively⁵¹:

$$L_c = \sqrt{B\kappa/\sigma_0} \quad (2.16)$$

$$l_p = 4 [3\mu B^2 \dot{R}_F / \sigma_0^3] \quad (2.17)$$

If $L_p > L_c$, then fluid propagation is dominated by the viscosity, while $L_c > L_p$ means that the separation is dominated by the tissue adhesion. When viscosity dominates, the blister propagation radius and central deflection are:

$$R_F(t) = 1.52 \left[\frac{B^3 Q^7}{(12\mu)^2 Q^2} \right]^{1/30} t^{3/10} \quad (2.18)$$

and

$$h(0, t) = 0.41 \left[\frac{(12\mu)^2 \sigma_0 Q^8}{B^3} \right]^{1/15} t^{2/5} \left(1 - \frac{r^2}{R_{FC}^2(t)} \right)^2 \quad (2.19)$$

When the flow rate is constant, the blister remains the same shape with proportional propagation of radius and height (Fig.2.16).

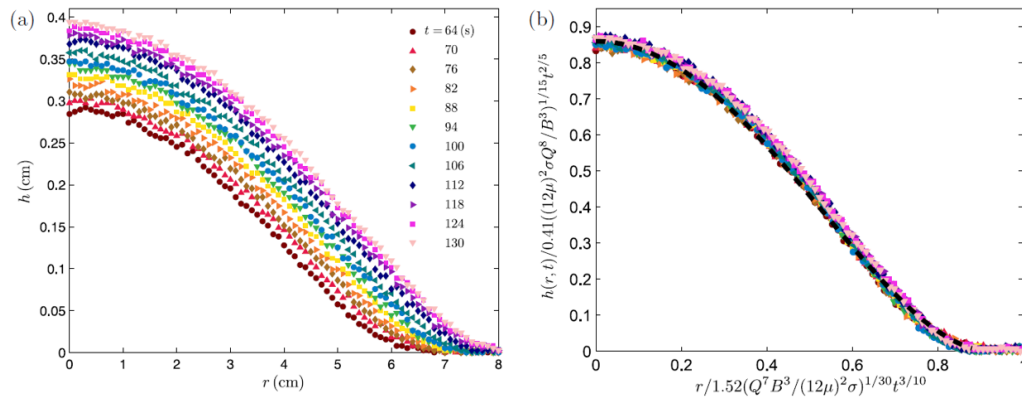


Figure 2.16: The blister profile in a numerical expression is constant when flow rate remains the same. The front tip curvature is then a constant. Figure reproduced from Ball and Neufeld⁵¹.

At arbitrary time t_c , a plate is put h_c above the substrate to constrain further lift, and then:

$$h_c = h(0, t_c) \quad (2.20)$$

$$R_{FC} = R_F(t_c) \quad (2.21)$$

substituting h_c into $R_{FC}/h_c^{3/4}$, then

$$R_{FC} = \frac{1.52 \cdot h_c^{3/4}}{0.41^{3/4}} \left[\frac{B^{1/4}}{(12\mu)^{1/6} Q^{7/30} \sigma_0} \right] \quad (2.22)$$

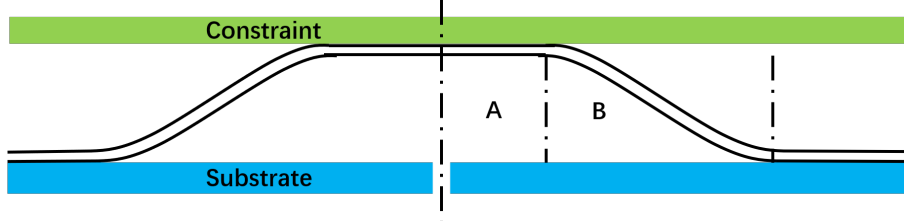


Figure 2.17: The propagating blister is divided into two regions, A is the constrained region and B the deformed region.

Substituting R_{FC} , t_c to (2.15), for a constrained blister test, gives curvature at the fracture front as:

$$\kappa = \frac{8h_c}{R_{FC}^2} = \frac{0.909}{h_c^{1/2}} \left[\frac{(12\mu)^{1/3} Q^{7/15} \sigma_0}{B^{1/2}} \right] \sim \mu^{1/3} Q^{7/15} \quad (2.23)$$

The fracture front curvature then only depends on the flow rate and viscosity of fluid injected.

For a conventional, unconstrained blister test, Equation (2.18) is valid. However, when the height is constrained, after the film touches the constraint it stops deforming and the whole blister can be divided into two regimes, the deforming regime (B) and constrained regime (A) (Fig.2.17). The first regime keeps deforming and is subjected to a critical R_{FC} which is determined by the height of constraint h_c . By global conservation and geometry of the conical circular frustum blister, the propagation radius is then:

$$R_F = \begin{cases} R_F(t) & t \leq t_c \\ \frac{R_{FC}}{2} + \frac{1}{6} \sqrt{\frac{36Qt}{\pi h} - 3R_{FC}^2} & t > t_c \end{cases} \quad (2.24)$$

From beam theory, in a pure bending regime the strain ε and curvature has the relationship:

$$\varepsilon = \kappa d \quad (2.25)$$

where d is the distance to the neutral axis of the top layer which is approximately 0.7 mm. This equation connects the yield strain of real lens capsule and the deformation of material that is mimicking the capsule.

Note that Equations (2.13), (2.18), (2.19) and (2.23) are all based on a free surface blister test so the application of them on constrained blister test may have discrepancies on the scale of values. However, under the assumption of the existence of uniform pressure inside the blister, they are still capable of reflecting the positive trend and dependency of each individual parameters.

2.5.2 Shear-thinning fluid hydraulic fracture

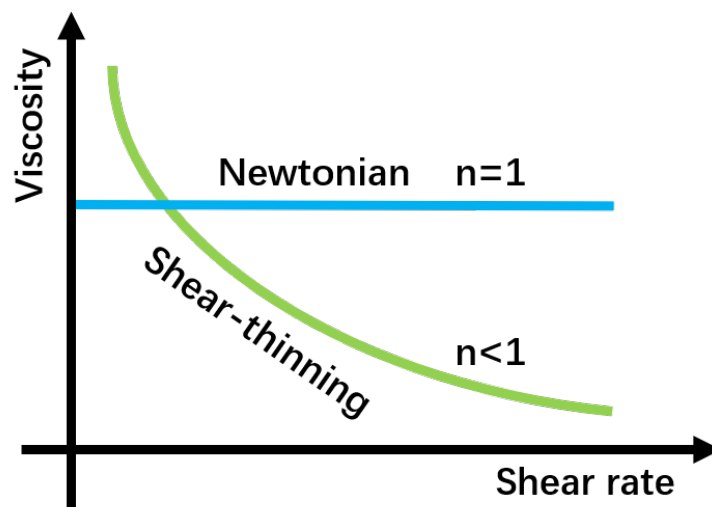


Figure 2.18: Schematic of different flow behaviours for a Newtonian fluid and a shear-thinning fluid. n is the power law index.

The fluids most commonly and widely used for hydraulic fracture have a similar flow behaviour to the (much less viscous) fluids used in cataract surgery for viscodissection. Both fluid classes exhibit what is called shear-thinning, where their

viscosity decreases the faster they are deformed. In contrast to Newtonian fluids that do not vary in rheology during flow, as shear-thinning fluids are moved faster (higher shear rates $\dot{\gamma}$) their viscosity μ becomes lower (Fig.2.18). As viscosity represents the flow resistance of a fluid, shear-thinning fluids require less applied shear stress (τ) when shear rate is high. In a simple form, shear-thinning behaviour can be mathematically described by a power-law model relating stress, σ and shear rate, $\dot{\gamma}$:

$$\tau = M\dot{\gamma}^{n-1}, \quad (2.26)$$

where M is the power law consistency and n the power law index. This equation reduces to the Newtonian case for $n = 1$, where the consistency becomes viscosity.

For Newtonian fluids, a constant viscosity can be applied via lubrication theory and Poiseuille's law to model the viscous drag and corresponding pressure drop, which can then be balanced with elasticity theory to predict the size and opening of fracture. For shear-thinning fluids, there is a more complicated balance because of the mutual dependency between shear rate-dependent viscosity, changes in fracture size that affects the shear rate, and viscosity-dependent drag. Despite this complexity, shear-thinning fluid-induced hydraulic fracture can still be described using the previously discussed theory⁴⁶.

Here two modified theories based on Equation (2.9) are introduced to describe general scaling of shear-thinning fluids and the second is more restricted to best describe the fracture studied in this project.

Equations (2.9) are modified as⁴⁹;

$$w = \epsilon L_n \Omega_n(\xi), \quad \lambda = L_n \Lambda, \quad \epsilon = \sigma_0 / E' \quad (2.27)$$

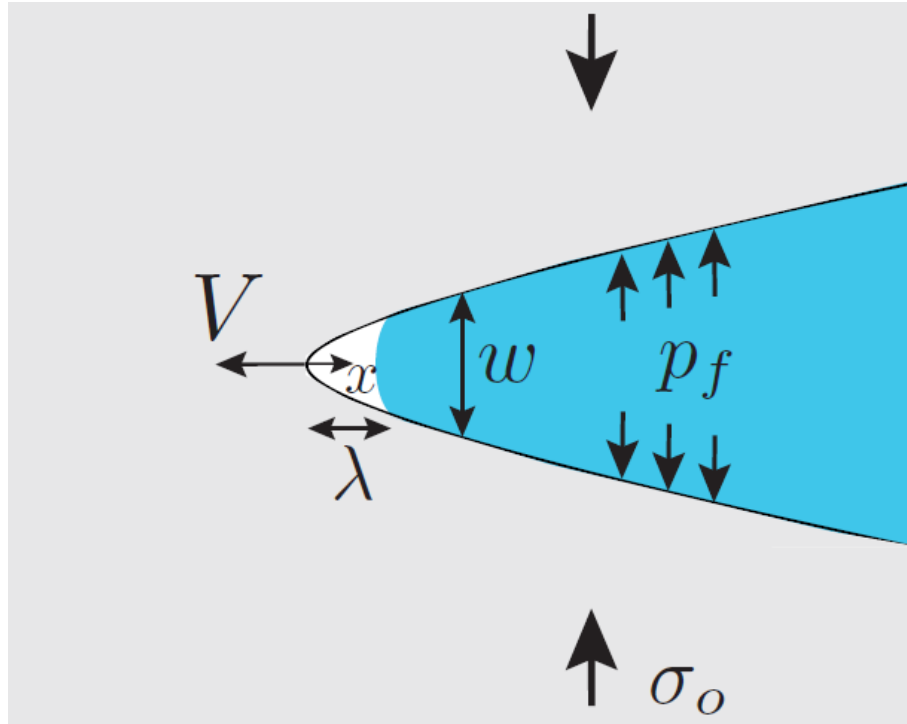


Figure 2.19: Schematic of vapor tip dimensions. Figure reproduced from Moukhtari and Lecampion⁴⁹.

where L_n is the characteristic length scale equal to the size of the vapor tip, λ (Fig.2.19). The dimensionless coordinate $\xi = x/L_n$ gives a scale of the distance to the fracture tip, with the dimensionless fluid lag $\Lambda = \xi = 1$ at $x = L_n$ makes $\lambda = L_n$. Here $\epsilon = \sigma_0/E'$ is a small parameter calculated by the compression stress σ_0 and material plane-strain elastic modulus $E' = E/(1 - \nu^2)$, a product of Young's modulus E and Poisson's ratio ν . The L_n can be further written as:

$$L_n = V \left(\frac{M'}{\sigma_0} \right)^{\frac{1}{n}} \left(\frac{E'}{\sigma_0} \right)^{\frac{n+1}{n}} \quad (2.28)$$

where $M' = \frac{2^{n+1}(2n+1)^n}{n^n} M$ is a modified power-law consistency with M and n obtained from $\tau = M\dot{\gamma}^{n-1}$. V is the fracture rate which is the velocity of fracture front. The last element $\Omega_n(\xi)$ is the dimensionless fracture opening and can be written as:

$$\Omega_n(\xi) = k_n \sqrt{\xi} \quad (2.29)$$

k_n denotes the dimensionless toughness, a parameter that involves the material fracture toughness K_{Ic} which can be related to the adhesion between two attached materials:

$$k_n = \sqrt{\frac{32}{\pi}} \frac{1}{V^{1/2}} \left(\frac{\sigma_0^{2-n}}{M' E^{3n+1}} \right)^{1/2n} K_{Ic} \quad (2.30)$$

with $\xi = 1$ there is $\Omega_n(1) = k_n$, and we apply the curvature function of bending under uniformly distributed load $\kappa = 2w/L_n^2$, giving a general form of curvature at the vapor tip:

$$\kappa = 2\sqrt{\frac{32}{\pi}} \left(\frac{\sigma_0^{3/2+3/n}}{E^{7/2+3/2n} M'^{3/2n}} \right) K_{Ic} \frac{1}{V^{3/2}} \sim \frac{1}{V^{3/2}} \quad (2.31)$$

This gives a relationship between curvature and fracture rate, as well as a quantification of the vapor tip size. However it fails to discuss the effects of flow rate which is closely related to the fluid pressure p_f . Also the scenario of zero toughness is not restricted. The second theory is introduced to include these factors.

Adachi and Detournay proposed a power-law model⁴² based on Equations (2.9), with the condition that shear-thinning behavior is described by the relationship between shear stress τ and shear rate $\dot{\gamma}$, namely $\tau = M(2\dot{\gamma})^n$, where M and n has the same meaning as previous theory indicated (e.g. Newtonian fluids $n = 1, M = \mu$; shear-thinning fluids $0 < n < 1$). Also considering a dimensional solution, we change the direction of dimensionless coordinate $\xi = x/l$ (Fig.2.20) the cracking size and opening can be written as:

$$l = \zeta_m L_m(t), \quad w = \epsilon_m(t) L_m(t) \Omega_m(\xi) \quad (2.32)$$

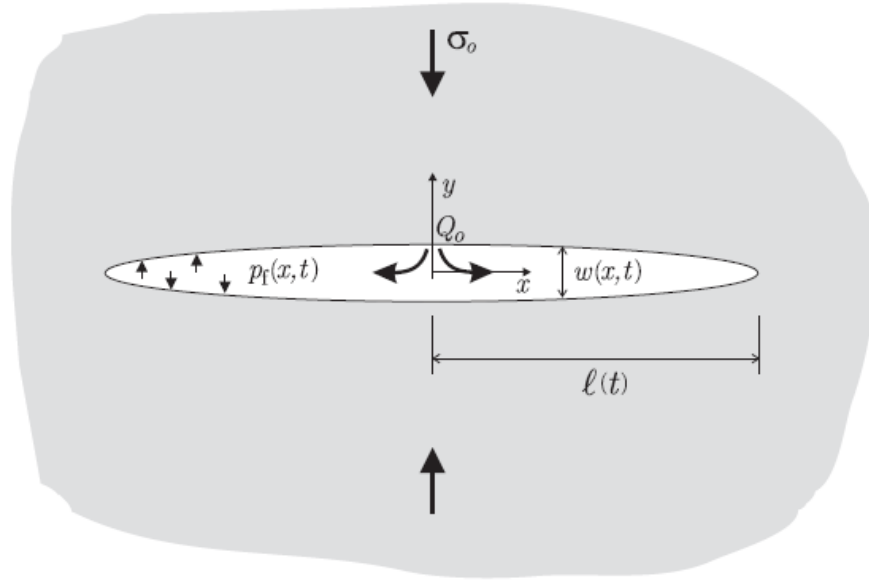


Figure 2.20: Modified fracture problem. The direction of x points from the fluid entry location to the faraway fracture tip. Figure reproduced from Adachi and Detournay⁴².

where ζ_m a dimensionless cracking length with a singular dependency on the power-law index n . $L_m(t), \epsilon_m(t), \Omega_m(\xi)$ are dimensionless parameters with similar definitions as the previous theory, and can be expressed with respect to $M' = \frac{2^{n+1}(2n+1)^n}{n^n} M$, plane-strain elastic modulus E' , time t and flow rate Q_0 :

$$\epsilon_m(t) = \left(\frac{M'}{E' t^n} \right)^{\frac{1}{n+2}}, \quad L_m(t) = Q_0^{1/2} \left(\frac{E'}{M'} \right)^{\frac{1}{2(n+2)}} t^{\frac{1}{2} + \frac{n}{2(n+2)}} \quad (2.33)$$

$\Omega_m(\xi)$ can be computed using n and dimensionless coordinate $\xi = x/l$ and with $\xi = (l-L)/l \rightarrow 1$ which indicates the fracture front, $\Omega_m(\xi)$ can be considered a constant Ω_m . Applying $\kappa = 2w/L^2$, tip size L is constant:

$$\kappa = 2\Psi \left(\frac{M'}{E'} \right)^{\frac{1}{2(n+2)}} Q_0^{\frac{1}{2}} t^{\frac{1}{2} - \frac{n}{2(n+2)}} \quad (2.34)$$

with $\Psi = 2\zeta_m^2 \Omega_m / L^2$, and for $0 < n < 1$, there is $\frac{1}{2} - \frac{n}{2(n+2)} > 0$. We then draw the conclusion that curvature at the fracture tip driven by shear-thinning fluids has a positive relationship with the flow rate and the time. For an expansion flow as in a blister test, fracture rate decays with time so curvature is negatively related to fluid velocity at the fracture front. For a free surface soft material separation, the shape of the blister can be described as a spherical cap, so that the time can be transformed to fracture rate as $t = 3Q_0 / \pi \epsilon_m(t) L_m(t) \Omega_m(0) V^2$. Then the curvature has following relationship:

$$\kappa = \frac{2}{L^2} \left(\frac{3}{\pi \bar{\Omega}_m(0)} \right)^{\frac{1}{n+3}} \zeta_m^{\frac{n+2}{n+3}} \bar{\Omega}_m(\xi) \left(\frac{M'}{E'} \right)^{\frac{1}{2(n+3)}} Q_0^{\frac{n+4}{2(n+3)}} \left(\frac{1}{V} \right)^{\frac{2}{n+3}} \sim Q_0^{\frac{n+4}{2(n+3)}} \left(\frac{1}{V} \right)^{\frac{2}{n+3}} \quad (2.35)$$

Notably, this is consistent with with Equation (2.23) which is derived from Newtonian fluid solutions: as fracture propagates the fracture rate becomes slower, so that at the front the shear rate becomes lower, causing a higher viscosity in the shear-thinning case. Similar to Newtonian fluid solutions, the theories presented for shear-thinning fluids are also for a free surface blister with uniform compression stress acting perpendicular to the direction of propagation, therefore when applying to a constrained blister the scale may eventually fail to describe the flow, requiring further study.

2.5.3 Yield stress and normal stress

As part of this work focuses on more complex fluid rheology, we can not completely apply past theories to description of more complex systems like yield stress and normal stress fluids in cataract surgery. It is, however, worthwhile to learn the behaviours of these two fluid classes on cataract surgery hydraulic fracture mainly because: 1. Yield stress fluids may provide cushioning effects to protect the eye

lens capsule and 2. High normal stress fluids may aid controlling the vertical hydrodynamic pressure and increase safety of lens capsule tissue deformation.

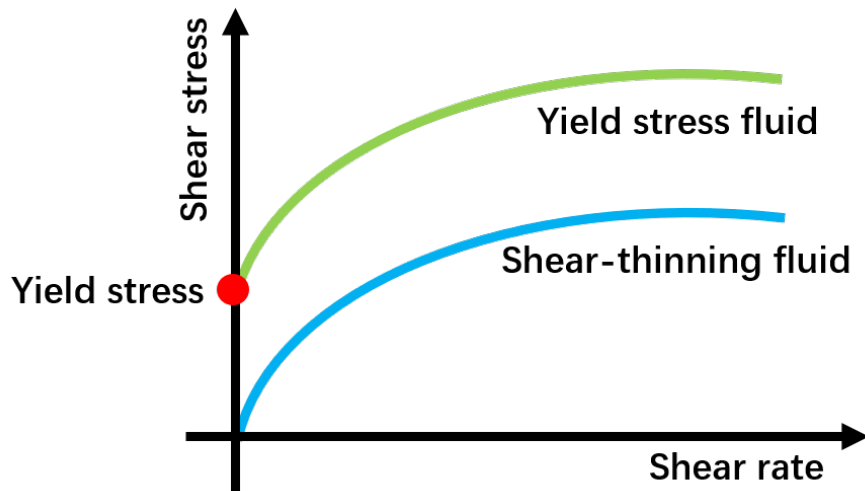


Figure 2.21: Schematic of the flow behaviour of a yield stress fluids and a shear-thinning fluid. The main distinction is that a minimum shear stress is required to initiate flow of yield stress fluids.

Broadly speaking, yield stress fluids are only able to flow and behave as a liquid when the applied shear stress exceeds a critical value, the yield stress. At stresses below the yield stress the system behaves as an elastic solid with no flow (Fig.2.21).

Though yield stress effects are not directly documented in cataract surgery, several articles have discussed phenomena that can be connected to the unique properties of a yield stress fluid. Generally, after the hydraulic fracture in surgery is done, it is necessary to test if lens capsule can be peeled off the nucleus surface completely with no attachment. This is normally done by manually rotating and depressing the nucleus. With different fluids, the performance may vary. If it can be done smoothly, then the capsule will not be damaged when removing the nucleus²⁰, otherwise the capsule may tear during nucleus extraction (Fig.2.9 (A)). When hydrodissection is conducted with Newtonian balanced salt solution, it can easily flow out of the capsule and cause less support to the capsule (Fig.2.9 (B)). Likewise, the nucleus

may not receive enough support so that it could be pushed to the entry and block it, causing pressure build-up (Fig.2.9 (C)). If the fluid has less flow capability it may still remain in the capsule and provide enough support (Fig.2.9 (D)) without blockage. Such capability is described as a "cushioning effect"¹⁹. Translating this into rheology terminology, it closely resembles the yield stress so it is important to characterise yield stress fluid behaviour in hydraulic fracture. An analogy to hydraulic fracturing is also appropriate as "proppants" are used for the same purpose in deep wells.

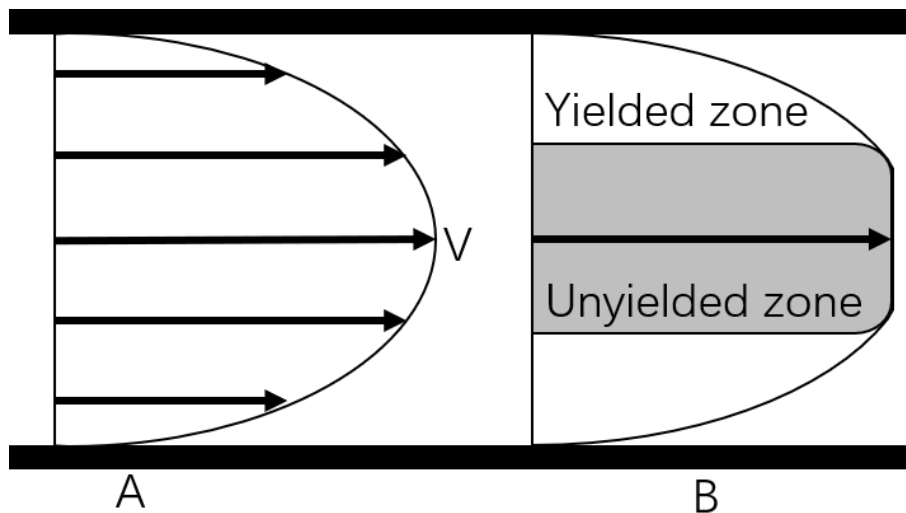


Figure 2.22: Comparison of flow profile between fluids without yield stress (A) and with yield stress (B). The arrows indicate the local flow velocity. For normal fluids, the velocity decays as the location approaches the wall because of friction. For yield stress fluids there is a yielded zone where fluid flows and acts like a lubricant, and there is an unyielded zone where fluid is in a solid-like state.

At small scales of fracture, the geometry can be considered Poiseuille flow between two parallel stationary plates. For yield stress fluids flowing in such geometry, the flow profile can be described by a plug shape which consists of the yielded region and unyielded region (Fig.2.22). The yielded region is normally very close to the plates and the shear stress in this region is higher than the yield stress because

of friction. As the location approaches the centre between the two plates, friction gradually decreases until it is lower than the yield stress, where there is a transition from yielded fluid to unyielded fluid (solid). The flow therefore shows a plug-like profile and in the unyielded region the fluid remains in a solid-like state with very low flow capability. In a squeezing flow that is similar to the flow at the fluid front of hydraulic fracture, the shear stress τ can be simply written $\tau = \mu \frac{dV}{dy} + \tau_0$, where τ_0 is the yield stress⁵³. Additional fluid rheology such as normal stress can be considered to supplement the benefits of existing dissection fluids.

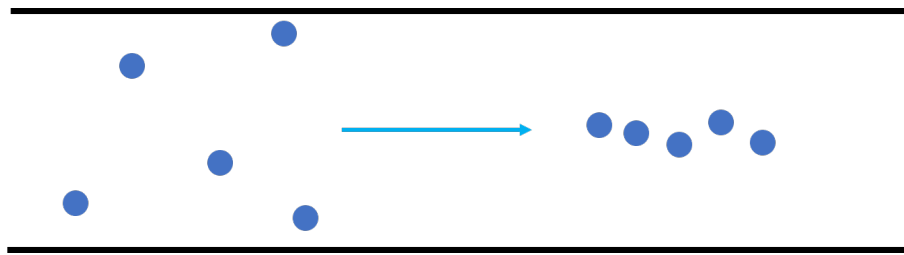


Figure 2.23: Schematic of suspended particle migration caused by a co-effect of shear stress and normal stress in pipe flow.

Normal stress is a stress perpendicular to the direction of shear flow and it is independent of the fluid pressure. Normal stress flow can cause interesting effects on process flows such as die swell and rod climbing, where fluids move in directions orthogonal to the direction of shear flow, potentially complicating production of polymer materials and operation of mixing processes. In terms of normal stress fluids, there is no literature discussing the effects of high fluid normal stress on hydraulic fracture. However the foundation of such behavior is simply lifting (or pulling together) of objects by apparent pressure. We thus make an analogy of such lifting behavior with the migration of suspended particles in high normal stress fluid pipe flow (Fig.2.23). This phenomenon occurs when suspended particles move to the centre of the streamline in a pipe flow due to bulk normal stress and shear rate gradients⁵⁴. The effect of normal stress on particles can be expressed in a simple

linear equation^{55,56}:

$$\Sigma = C_N + C_S \quad (2.36)$$

where C_N and C_S are contributions of normal and shear stresses respectively. We will use our experimental system to examine any contributions such fluids make to hydraulic fracture in tissue models.

2.6 Conclusion

Cataract is one of the greatest human health challenges, accounting for almost half of blindness cases. It is caused by physiology and aging and is irreversible, so the only effective treatment is cataract surgery. Despite the success of cataract surgery, there are numerous factors that have not been quantified or optimised in a way that can predict safety and relate measurable properties to the risk of lens capsule rupture. In addition there is not currently sufficient knowledge to begin design of robotic surgical control systems. This project aims to provide some of these details and, hopefully, enhance safety of cataract surgery. The objectives are to understand the fluid separation mechanism and improve connections between rheology, hydrodynamics and adhesion.

In this chapter firstly the eye lens structure was introduced, and some key findings are:

- The whole lens has four main components that matter in surgery: capsule, epithelium, cortex and nucleus.
- Capsule, cortex and nucleus are complex structures of enucleated fiber cells that are the product of epithelium cell differentiation.

- The lens capsule is a fragile vessel and it grows thicker over a person's lifetime because of the growth of epithelium. Epithelium is located between the capsule and cortex and it is only a single-layer cell tissue.
- The cortex and nucleus have an onion-like structure. They are comprised of several layers of fiber cells and each layer is comprised of adjacent fiber cells. The cells are hexagonal in shape so the interface between them is not smooth.

Secondly cataract surgery is introduced. The cataract is an irreversible structure that can only be treated by surgery, which removes and replaces the failed lens to restore sight. In general the capsule is first opened by capsulorhexis, then a viscodissection/hydrodissection is performed to break the adhesion between tissues. At last the cortex and nucleus are fractured and removed by phacoemulsification and an intraocular replacement lens is implanted. Though capsule rupture is rare, it does occur. Viscodissection may ease this risk as it provides more cushion effects, but variations in adhesion between capsule and cortex, corticalcapsular adhesion make more detailed understanding a necessity. Enabling better control of operation parameters is expected to improve safety by reducing risk.

Third, the bio-mechanics of the eye lens are introduced and discussed in the context of safety concerns. The elasticity of the lens capsule decays with age due to the growth and deviation of epithelium cells, causing an increase in capsule thickness. The variation in values of important properties including yield strain, yield stress, Young's modulus, and thickness are discussed.

The blister test is introduced to study the separation process, and a theory is explained to describe flow behavior of multiple fluid types in tissue fracture. The separation is dominated by the fracture front tip, which means the radius propagation and deformation is determined by the conditions of the fracture front. The

extent of separation and the curvature at the fracture front are shown to be critical variables for measurement as a path to characterising cataract surgery processes.

2.7 References

- [1] L. A. Remington, D. Goodwin, *Clinical anatomy of the visual system E-Book*, Elsevier Health Sciences, **2011**.
- [2] T. C. COURSE, *Lens Anatomy*, **2020**, <http://cataractcourse.com/lens-anatomy-and-development/lens-anatomy/>.
- [3] M. Dubbelman, G. Van der Heijde, H. A. Weeber *et al.*, *Optometry and Vision Science* **2001**, *78*, 411–416.
- [4] S. A. Strenk, J. L. Semmlow, L. M. Strenk, P. Munoz, J. Gronlund-Jacob, J. K. DeMarco, *Investigative ophthalmology & visual science* **1999**, *40*, 1162–1169.
- [5] C. E. Jones, D. A. Atchison, J. M. Pope, *Optometry and Vision Science* **2007**, *84*, 990–995.
- [6] F. H. Adler, *Adler's physiology of the eye: clinical application*, Mosby, **1992**.
- [7] S. Krag, T. T. Andreassen, *Progress in retinal and eye research* **2003**, *22*, 749–767.
- [8] R. Fisher, *The Journal of physiology* **1969**, *201*, 1–19.
- [9] G. Van Alphen, W. P. Graebel, *Vision Research* **1991**, *31*, 1417–1438.
- [10] W. J. Krause, J. H. Cutts *et al.*, *Concise text of histology*, Williams & Wilkins, **1986**.
- [11] S. TROKEL, *Investigative Ophthalmology & Visual Science* **1962**, *1*, 493–501.
- [12] J. L. Aliò, A. Anonia, C. Sagnelli PCavallotti, L. Cerulli, *Aging of the human lens Age-related changes of the human eye*, **2008**.
- [13] R. T. Mathias, J. Kistler, P. Donaldson, *Journal of Membrane Biology* **2007**, *216*, 1–16.
- [14] B. K. Straub, J. Boda, C. Kuhn, M. Schnoelzer, U. Korf, T. Kempf, H. Spring, M. Hatzfeld, W. W. Franke, *Journal of cell science* **2003**, *116*, 4985–4995.
- [15] G. Tabin, M. Chen, L. Espandar, *Current opinion in ophthalmology* **2008**, *19*, 55–59.
- [16] K. J. Cruickshanks, B. Klein, R. Klein, *American journal of public health* **1992**, *82*, 1658–1662.

-
- [17] S. Krag, T. Olsen, T. T. Andreassen, *Investigative ophthalmology & visual science* **1997**, *38*, 357–363.
- [18] A. I. Jobling, R. C. Augusteyn, *Clinical and experimental optometry* **2002**, *85*, 61–75.
- [19] V. Vasavada, V. A. Vasavada, L. Werner, N. Mamalis, A. R. Vasavada, A. S. Crandall, *Journal of Cataract & Refractive Surgery* **2008**, *34*, 1173–1180.
- [20] A. R. Vasavada, D. Goyal, L. Shastri, R. Singh, *Journal of Cataract & Refractive Surgery* **2003**, *29*, 309–314.
- [21] A. R. Vasavada, R. Singh, D. J. Apple, R. H. Trivedi, S. K. Pandey, L. Werner, *Journal of Cataract & Refractive Surgery* **2002**, *28*, 1623–1628.
- [22] A. R. Vasavada, S. A. Dholakia, S. M. Raj, R. Singh, *Journal of Cataract & Refractive Surgery* **2006**, *32*, 1196–1200.
- [23] WebMD, *What to Expect With Cataract Surgery*, <https://www.webmd.com/eye-health/cataracts/ss/slideshow-cataract-surgery-expect>, Accessed: 2020-06-08.
- [24] I. M. Wormstone, L. Wang, C. S. Liu, *Experimental eye research* **2009**, *88*, 257–269.
- [25] A. Vasavada, S. Raj, V. Vasavada, S. Shrivastav, *Eye* **2012**, *26*, 761–770.
- [26] Y. Ghosh, G. Kirkby, *Eye* **2008**, *22*, 844–848.
- [27] S. H. Dewey, *Journal of Cataract & Refractive Surgery* **2002**, *28*, 11–14.
- [28] S. Ermiş, F. Öztürk, Ü. Ü. Inan, *British journal of ophthalmology* **2003**, *87*, 1356–1359.
- [29] R. M. Pedrigi, J. D. Humphrey, *ASME 2008 Summer Bioengineering Conference*, **2008**, pp. 1013–1014.
- [30] C. C. Danielsen, *Experimental Eye Research* **2004**, *79*, 343–350.
- [31] H. B. Dick, S. E. Aliyeva, F. Hengerer, *Journal of Cataract & Refractive Surgery* **2008**, *34*, 1367–1373.
- [32] M. F. Marmor, *Progress in retinal research* **1993**, *12*, 179–204.
- [33] J. Tong, G. Sommer, P. Regitnig, G. A. Holzapfel, *Annals of biomedical engineering* **2011**, *39*, 1703–1719.

References

- [34] K.-L. P. Sung, M. K. Kwan, F. Maldonado, W. H. Akeson, *Journal of Biomechanical Engineering* **1994**.
- [35] E. A. Evans, D. A. Calderwood, *Science* **2007**, *316*, 1148–1153.
- [36] H. Dannenberg, *Journal of Applied Polymer Science* **1961**, *5*, 125–134.
- [37] M. Napolitano, A. Chudnovsky, A. Moet, *Journal of Adhesion Science and Technology* **1988**, *2*, 311–323.
- [38] Y. Chu, C. Durning, *Journal of Applied Polymer Science* **1992**, *45*, 1151–1164.
- [39] Y.-S. Chang, Y.-H. Lai, D. A. Dillard, *The Journal of Adhesion* **1989**, *27*, 197–211.
- [40] M. Parsons, A. Polyakova, E. Stepanov, A. Hiltner, E. Baer, *The Journal of Adhesion* **1998**, *68*, 45–63.
- [41] J. Williams, *International Journal of Fracture* **1997**, *87*, 265–288.
- [42] J. Adachi, E. Detournay, *International Journal for Numerical and Analytical Methods in Geomechanics* **2002**, *26*, 579–604.
- [43] O. Reynolds, *Philosophical transactions of the Royal Society of London* **1886**, 157–234.
- [44] Q. J. Wang, Y.-W. Chung, *Encyclopedia of tribology*, Springer, **2013**.
- [45] J. Desroches, E. Detournay, B. Lenoach, P. Papanastasiou, J. R. A. Pearson, M. Thiercelin, A. Cheng, *Proceedings of the Royal Society of London. Series A: Mathematical and Physical Sciences* **1994**, *447*, 39–48.
- [46] D. Garagash, E. Detournay, *J. Appl. Mech.* **2000**, *67*, 183–192.
- [47] E. Detournay, *International Journal of Geomechanics* **2004**, *4*, 35–45.
- [48] A. P. Bungler, E. Detournay, D. I. Garagash, *International journal of fracture* **2005**, *134*, 175–190.
- [49] F.-E. Moukhtari, B. Lecampion, *Journal of Fluid Mechanics* **2018**, *838*, 573–605.
- [50] Z.-Q. Wang, E. Detournay, *Journal of Applied Mechanics* **2018**, *85*, year.
- [51] T. V. Ball, J. A. Neufeld, *Physical Review Fluids* **2018**, *3*, 074101.
- [52] J. Flitton, J. King, *European Journal of Applied Mathematics* **2004**, *15*, 713–754.
- [53] S. Wilson, *Journal of Non-Newtonian Fluid Mechanics* **1993**, *47*, 211–219.
- [54] B. Ho, L. Leal, *Journal of Fluid Mechanics* **1976**, *76*, 783–799.

- [55] J. F. Morris, F. Boulay, *Journal of rheology* **1999**, 43, 1213–1237.
- [56] R. M. Miller, J. F. Morris, *Journal of non-newtonian fluid mechanics* **2006**, 135, 149–165.

Chapter 3

Adhesion measurement

In cataract surgery, it is well-recognized that there is biological adhesion between the capsule, the cortex and the nucleus. Such adhesion is termed "cortical-capsular adhesion" and remains a largely uncharacterised eye lens property. The absence of such knowledge, despite the wide use of cataract surgery for decades, is mainly because of the relatively small size of the eye lens and the fragility of lens tissues, making them difficult to study by conventional adhesion tests like peeling. More information on adhesion in lens tissues and the dynamics of their separation would aid understanding and optimisation of cataract surgeries.

A general definition of adhesion strength is the minimum energy required to separate a unit area of surface. Based on this, the measurement of adhesion strength of various materials has been intensively studied. Depending on the texture and mechanical properties of the substrate, different testing methods are developed. For common plastic tapes and films, a simple peeling test is useful. Adhesion can be related to an energy, and if the material substrates under study are elastic then their deformation during peeling must also be considered¹⁻³. Peeling and other adhesion test methods that use direct contacted measuring geometries may be limited in their usefulness for fragile materials, as the test may cause damage to the material prior to the measurement. Other methods are then preferred, such as the four-point bending test that bends two attached soft sheets and measures the stress required to cause them to crack⁴. Direct deformation of materials by probe testing is also

used⁵. Another commonly-used test is the blister test, where a pressurized fluid is pushed in between two surfaces to cause separation and allow calculation of the necessary driving pressure⁶. The blister tests allows testing of fragile material adhesion without complications other tests bring such as clamping damage, mechanical stress control, and sample non-uniformity⁷⁻⁹. The blister test also closely mimics the physical process that occurs during cataract surgery. Therefore, this chapter adapts the blister test to measure the adhesion strength of two soft polymer gels as an experimental model for soft eye lens tissue. The technique offers a potential approach to measurement of biological tissue adhesion, such as the corticalcapsular in the eye lens.

3.1 Materials and methods

To adapt the blister test, a polymer gel combined multi-layer injection model is used to measure the adhesion. The first part is the base of injection model, which consists of a channeled base and a contacting surface. Polydimethylsiloxane (PDMS) with cross-linker:polymer mass ratio of 1:10. A T-shape mould (Fig.3.1 (b)) is used to make a T-channel inside the base (Fig.3.1 (a)). Roughness of the contact surface layer is tuned by moulding on sand paper with different roughness values. The channeled base and the contact surface are brought together by treating the surface with a plasma cleaner prior to contact. For the final injection model preparation, the injection model is put in a petri dish which is then filled up with 30 mL of 15% aqueous gelatin solution to cover the whole model base. The gelatin layer is then allowed to solidify for 3 hours before use.

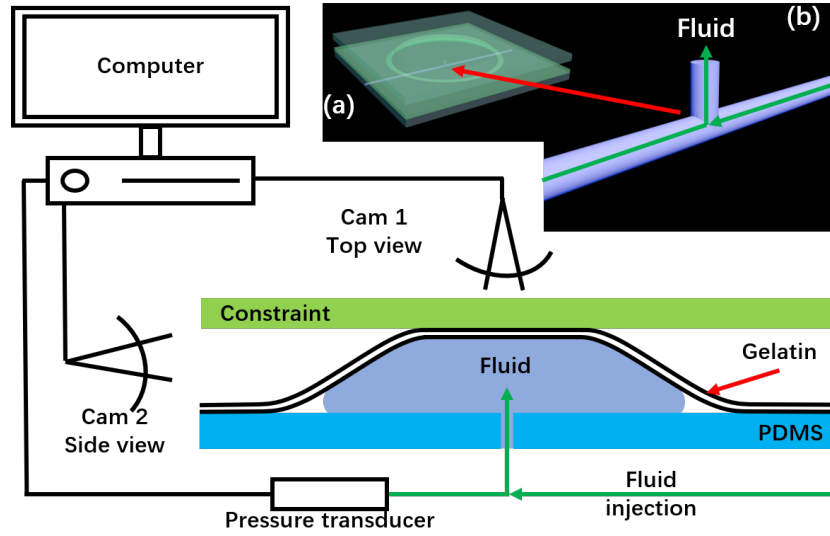


Figure 3.1: Schematic of experimental set-up and sample structure. Pressure transducer reads and records the pressure at the entry of the fluid into the micro-channel; compressed air is used to pressurize the liquid in the syringe and push it into the model. (a) 3D structure of injection model, bright green ring indicates the edge of blister where separation happens; (b) T-shape mould used for templating the micro-channel in the base layer.

3.1.1 Interface roughness measurement

Three substrate surfaces with different roughness values are used to study the impact of contact area on adhesion. We characterise roughness by its average value. To calculate it, a central line is drawn to enclose the profile of the experimental model surface. The average roughness R_a is then the arithmetical mean deviation of the distance y between the profile and the central line^{10,11}

$$R_a = \frac{1}{n} \sum_{i=1}^n |y^i| \quad (3.1)$$

where n is the horizontal sample length of the rough surface profile (e.g. in Fig.3.2 n being the length of left to the right). The central line is drawn so that the areas F_n enclosed by the profile above and below the central line should equal one

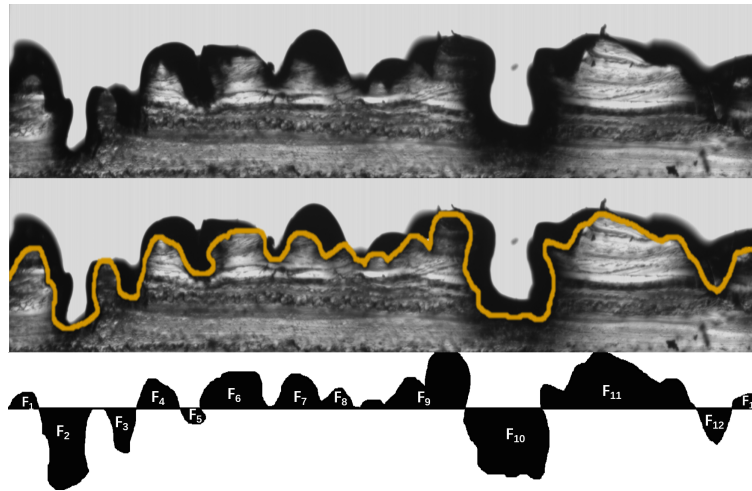


Figure 3.2: Profile of rough PDMS surface, a central line is determined so that the enclosed areas F_n above the central line is equal to the enclosed area below.

another

$$F_1 + F_4 + F_6 + F_7 + F_8 + F_9 + F_{11} + F_{13} = F_2 + F_3 + F_5 + F_{10} + F_{12} \quad (3.2)$$

To determine the location of the central line for any irregular profiles, a simple method is used. The profile is input into ImageJ and processed to a binary image with only black and white colors (Fig.3.3 (A,B,C)), then the overall area of the profile is measured. Applying a fixed coordinate the area of the profile should equal the product of the central line y distance and total x length (e.g. in Fig.3.3 (E) profile area = $F_2 + F_4$, and the requirement for roughness calculation $F_2 = F_1 + F_3$, so that central line area = $F_1 + F_3 + F_4 = F_2 + F_4 =$ profile area). With measurable profile area and total x length the location of central line is easily calculated.

By this method, all rough surfaces were measured at multiple locations of the surface to ensure the values are representative (Fig.3.4).

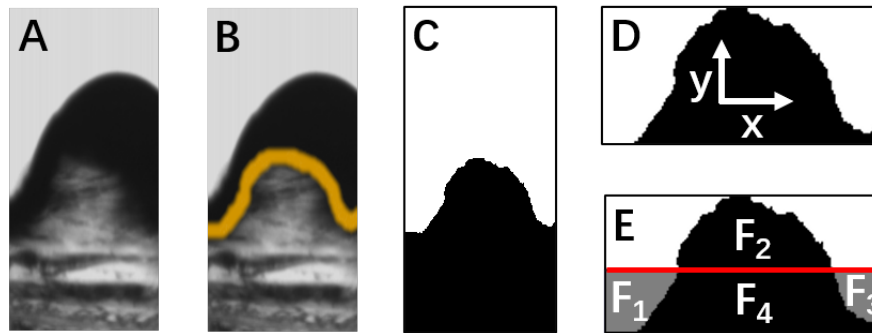


Figure 3.3: General image analysis of roughness and central line determination. A: Raw image. B: Profile outlined. C: Binary processing. D: Fixed coordinate. E: Area define and central line location, central line should be set so that the areas $F_1 + F_3 + F_4 = F_2 + F_4$.

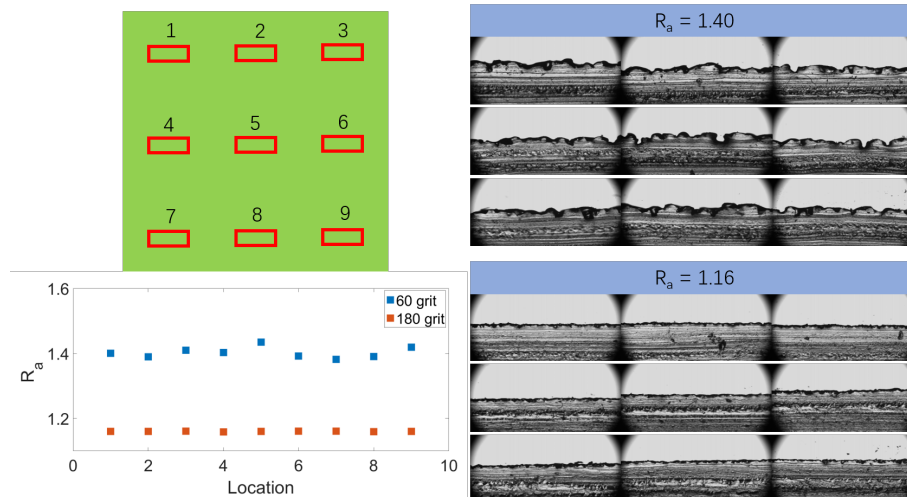


Figure 3.4: Microscopy of sample surfaces at varies spots

3.1.2 Experimental set-up

Fig.3.1 shows a schematic of the experimental set-up. A glass slide is placed approximately 2.5 mm above the injection model to constrain the maximum height the gelatin layer can reach when separated. During an experiment, the injection model is connected to a pressure transducer and syringe via the two ends of the micro-channel. Compressed air pressurizes the fluid in the syringe and moves liquid into the system. The pressure transducer monitors the instantaneous pressure and allows us to record it by a computer. Two cameras are used to capture the top view and side view of the blister during an experiment to provide information on rate and extent of separation. The top view shows the extent of separation while the side view shows the profile of the artificial tissue being separated.

3.1.3 Adhesion measurement

Before starting an adhesion measurement, the surfaces need to be validated as reproducible. As shown in the microscope photos (Fig.3.4) both rough surfaces have consistent roughness at different locations, which means that the models have relatively well-distributed patterns. This will then ensure a consistent adhesion strength measurement for the whole injection model.

To measure the adhesion strength of the models, modifications need to be made to the experiment set-up above. Fig.3.5 shows the set-up for measuring adhesion. Valve 1 controls the opening of compressed air, and seals the system if fully closed. Valve 2 stops flow if fully closed.

Before the start of experiment, compressed air is preset to a target value using a regulator while valve 2 is kept closed. Immediately after starting, valve 1 is closed, which ensures that a certain amount of air is compressed inside the syringe with exactly the target value. Valve 2 is then opened to trigger the separation by the

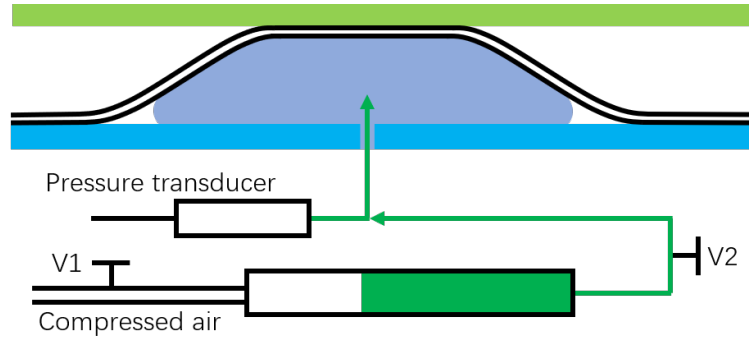


Figure 3.5: Schematic of adhesion measurement set-up. Compressed air is pumped in to pressurize the fluid, valve V1 encloses the air when closed and valve V2 stops the flow when closed.

energy stored in the compressed air. As separation happens, the air pressure is continuously released until the pressure is not enough to support the separation of tissue. During the whole process, side and top views are captured with time to show the extent of separation and the curvature of the blister edge, which can then be used to calculate the area of separation and the volume of fluid injected to create the blister.

Adhesion measurement by blister test uses an energy balance to determine the work of separation¹²⁻¹⁴:

$$G = \frac{dW_{ext}}{dA} = P \cdot \frac{dVol}{dA} = P \cdot h \cdot q \quad (3.3)$$

The adhesion G is characterised by the total external energy input W_{ext} to create new interface area, which is given by the product of pressure P and volume of fluid injected $dVol$. Practically, the external energy would be consumed in many forms such as tissue deformation, and elastic and kinetic energy dissipation during fast separation. A constrained height blister allows us to minimize the significance of other forms of energy as much as possible and ensure that the external energy input is mainly consumed by adhesion breakdown. A shape correction factor q is used to

measure the volume of fluid injected to the blister, correlating the pressure and the height the gelatin layer is lifted^{12,13}:

$$q = \left(1 - \frac{l}{2R}\right) + \left(\frac{l}{3R} - \frac{1}{2}\right) \cdot \frac{dl}{dR} = \frac{1}{2} + \frac{r}{2R} \quad (3.4)$$

where l is the extended length of blister which shows the dimension of deforming region B , R is the blister radial length and r is the radial length of the constrained region A of blister (Fig.3.6). Often, the change in extended length $\frac{dl}{dR}$ is two orders of magnitude smaller than the other terms of the equation and can be neglected. The resulting equation equates the left term to only the two radial lengths.

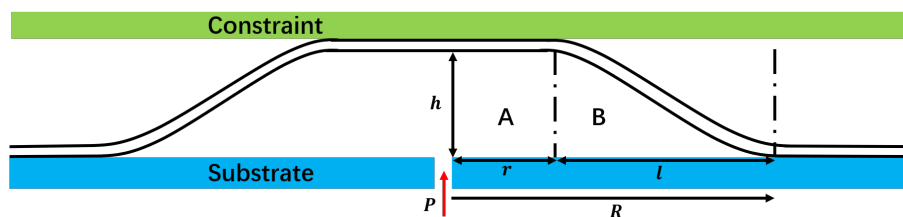


Figure 3.6: Configuration of a sample, where l is the extended length, R is the radial length of blister edge, r is the constrained radial length, and h is the constrained height between gelatin and glass slide

When pressure, height, and shape correction factor are accessible, the value of adhesion can be directly calculated.

3.1.4 Blister image processing

To obtain the necessary parameters for adhesion calculation, the blister profile needs to be digitized and quantified. Software ImageJ and MATLAB are used. Generally the process is as follows:

- The blister image is obtained directly from experiment-setup camera (Fig.3.7 (A))

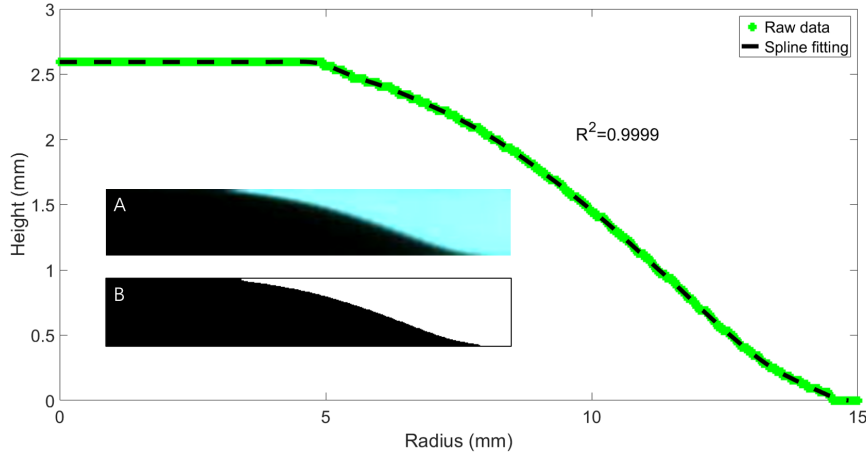


Figure 3.7: Image analysis of blister profile. A is the raw image captured with camera and B is the binary image processed with ImageJ. Green curve shows the raw data extracted from B and black dashed curve is the fitting by a spline method using MATLAB.

- It is input into ImageJ and converted to binary image with only black and white color (Fig.3.7 (B))
- By setting the scale of B to 36 pixels/mm, it is then digitized and exported to a coordinate (Fig.3.7)
- This is then input into MATLAB and fitted by a spline method, with the fitting $R^2=0.9999$ (Fig.3.7)

The raw images are captured with a resolution that gives 36 pixels/mm scale, meaning that the minimum observable length unit being 0.028 mm. The fitting accuracy is shown to have $R^2=0.9999$. Combining these two factors the error in dimension measurement is only 1%. This is however not an issue for final adhesion calculation because if criticising this with error propagation in Equation 3.4, there is

$$q_{error} = \frac{1}{2} + \frac{r \times error}{2R \times error} = \frac{1}{2} + \frac{r}{2R} = q \quad (3.5)$$

Once the processing is complete the parameters q , l , r and R can be read directly for adhesion measurement.

3.2 Results and discussion

Generally, during a separation process, system pressure always decays as separation continues. If the system is running with continuous driving pressure supply which is higher than the minimum requirement for separation, the system pressure tends to drop to a steady state value with ongoing separation. If the driving pressure supply is not continuous through the whole separation process, it will decay to a point at which the pressure is not sufficient to support the separation. This is the point of minimum requirement by which the intrinsic adhesion can be measured and is only accurately obtained if the separation is performed at a very low rate¹³.

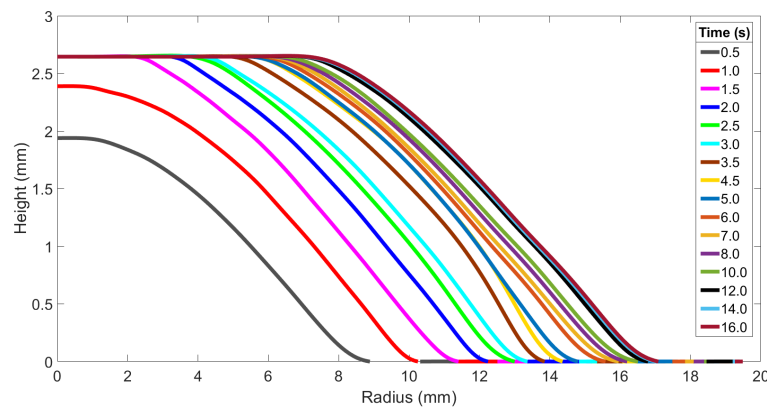


Figure 3.8: Blister dynamic profile on flat surface at 5 psi. Legend shows different time intervals in different stages of the process. The black curve indicates that separation approaches its end.

It is necessary to define the period of the separation process near the end. Fig.3.8 shows the dynamic profile of a flat surface separating from a compressed air pressure of 5 psi. At the beginning the blister grows rapidly and soon makes contact with the glass slide above. Following that there is a decay process where the separation

rate continually drops. This correlates with the system pressure (Fig.3.9) which shows the same trend. As can be seen after 12 seconds there is only ~ 0.3 mm propagation in 4 seconds, which is much slower than the rate before this time. This late stage is so slow that the separation can be considered terminated, thus the static blister profile and pressure after 12 seconds can be selected for adhesion calculation. It can be seen that the time for tissue to reach the constraint is only 1.5 seconds which likely means that the tissue is not stretched to an extent that deformation can't be neglected. Also noticeable is that the height of the constraint is around 2.7 mm with a variation of ± 0.1 mm. Parsons *et al.* found that too small or large a height can destabilise blister growth and it is preferable that the height be within 1.5 - 5 times as thick as the tissue. Based on this, the height of the constrained blister model presented in this chapter is controlled to be approximately 2.5 times thicker than the tissue to provide stable propagation¹³.

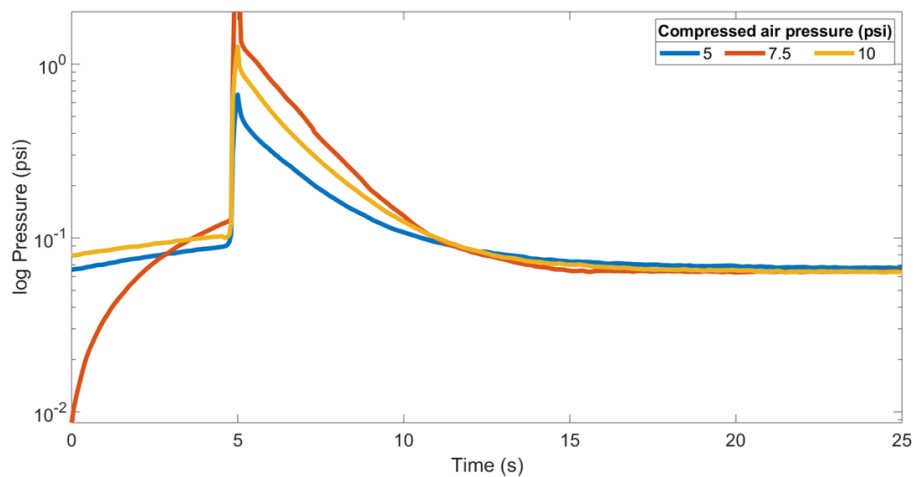


Figure 3.9: Dynamic pressure with various compressed air pressures on a flat surface. All curves drop to a certain value at the late stage of separation.

Fig.3.9 shows a separation process with three different initial pressures and all three curves fall to a certain value at the end of separation. As expected, during separation without continuous pressure supply, the initially stored energy will be

gradually consumed until it is not sufficient to further support the breakdown of adhesion.

For all three trials, a peak value in pressure is seen. This peak is where the separation first starts. In some early studies the peak value is defined as the critical pressure to create new surface. However, in our project, it is found that the peak value may not be taken as the effective value to calculate adhesion because it is always much higher than the minimum pressure needed to maintain separation and this initial pressure may be not reliable. In some cases the debonding after this initial critical pressure can be “catastrophic”¹⁵. The data shown indicate that a high critical pressure may not be related to adhesion strength as the measured peak pressure at 7.5 psi compressed air pressure is higher than that at 10 psi. In all the experiments no obvious pattern was observed from this peak pressure. The reason for such inconsistency is that initial pressure depends on many factors, including the angle of fluid injection from the entry channel, the air trapped between the tissue and the active fluid tip and especially the occupation by tissue of the entry channel for the experiments conducted here (Fig.3.10).

Creation of new interfacial area and breaking adhesion requires the fluid find a weak point. If the tissue is only laid on the substrate, the tissue and substrate are only weakly bonded by adhesion and can be lifted and separated easily (Fig.3.10 (left)). In this case, the pressure is the true value that can trigger the initial fracture. However, as shown in Fig.3.10 (right), when the entry channel is partially occupied by tissue there will be less variability of adhesion to be broken. At the region where tissue occupies the entry, more energy is needed to overcome the shear motion between the tissue and the channel wall. Therefore, the energy is consumed in more aspects than only creating new interface. If too much is present, as when tissue fully occupies the channel (Fig.3.10 (bottom)), a much higher pressure than the actual

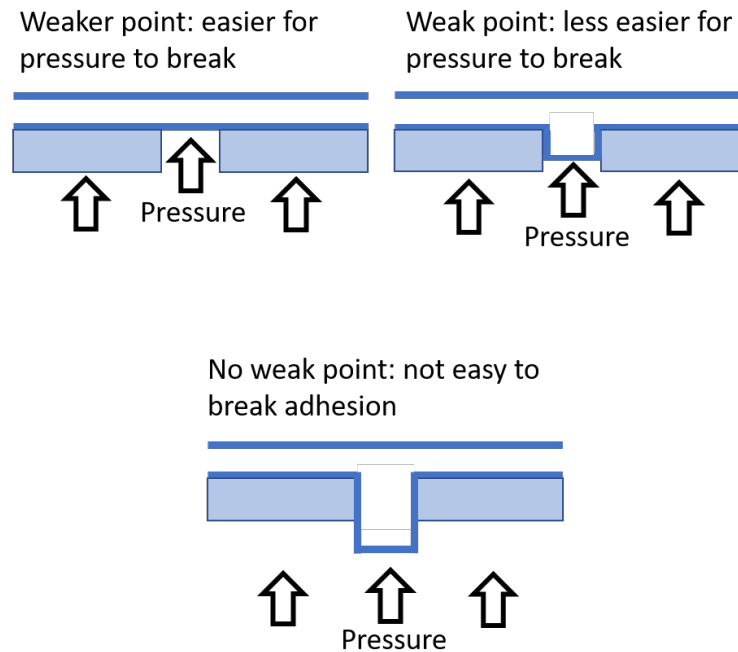


Figure 3.10: Schematic of tissue occupying entry channel.

pressure that is required occurs because of unnecessary energy consumption. This being said, if this initial peak pressure is used for calculation, the adhesion strength calculated would be higher than it should be because the contributions to compress, shear and lift the tissue are added on. To ensure the accurate measurement, we only concern about the pressure in the later stabilized stage after the initial breakdown happens, as in that stage the only dominating energy consumption is adhesion breakdown.

Once the late stage of separation is determined the next step is to extract the blister profiles for all three conditions studied (Fig.3.11). Differences in the constrained radial length and the blister edge radial length are evident, with the latter value increasing with pressure as more area is exposed during separation.

Based on the final profile, the shape correction, q , value can be extracted. Fig.3.12 shows the q value during the separation process. Plotting q as a function of time we

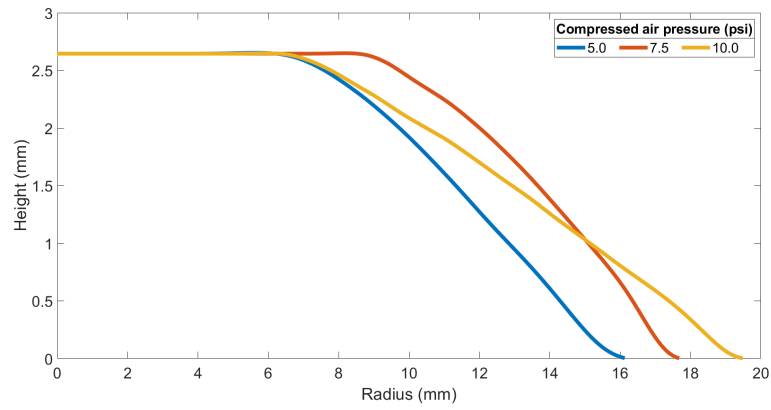


Figure 3.11: Blister profiles near the end of separation on a flat surface at three different initial pressure values.

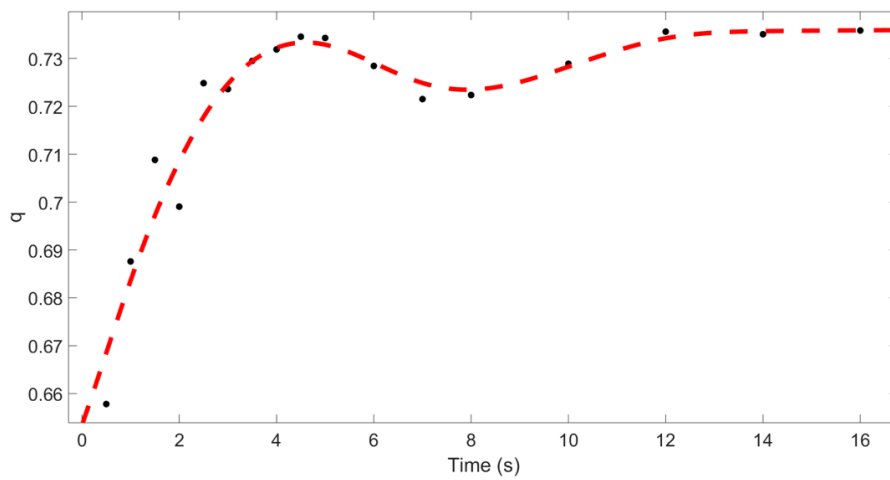


Figure 3.12: Blister shape correction factor as function of time

see that this value starts low at the beginning and then increases slowly. This is because adhesion and deformation are still stabilising but the system q becomes more consistent with time and blister growth, approaching 1. At the late stage there is little change in the shape and radial lengths of the blister, so q becomes more constant and can be used to calculate intrinsic adhesion.

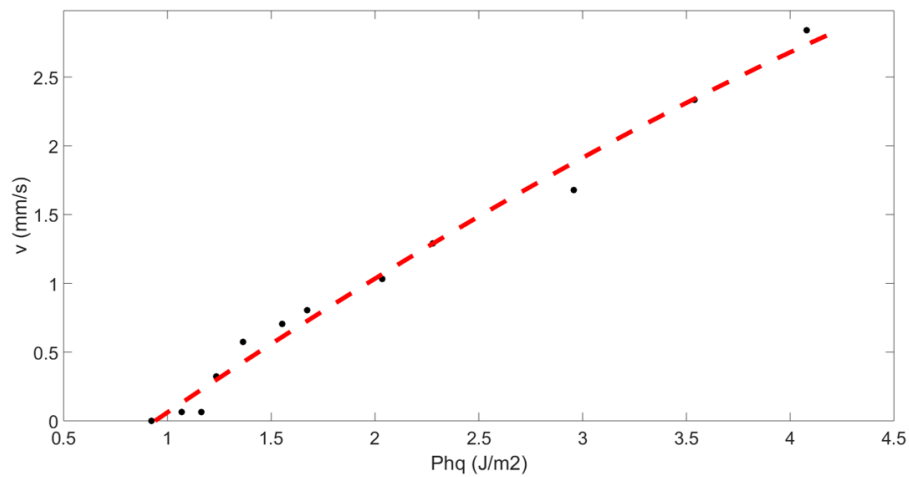


Figure 3.13: Effect of total energy input on separation rate.

From Fig.3.11, q can be extracted for all three pressures. Using the measured P and h , the effect of energy input on the separation is easily determined. It is obvious that in (Fig.3.13), the separation rate depends on the total energy input to the system. As energy is continuously consumed, the separation rate gradually decreased to the stage that close to the end of separation in which the rate becomes zero. When separation rate is zero, the energy input Phq is at around 0.93 J/m^2 . This being the intrinsic value of adhesion.

Processing the data obtained on surfaces with three different roughness values using the same method, we find that the adhesion values increase with roughness (Fig.3.14). Rougher surfaces have larger total unit contact area between the base and the tissue, so the increased adhesion is consistent with expectations. Notably the

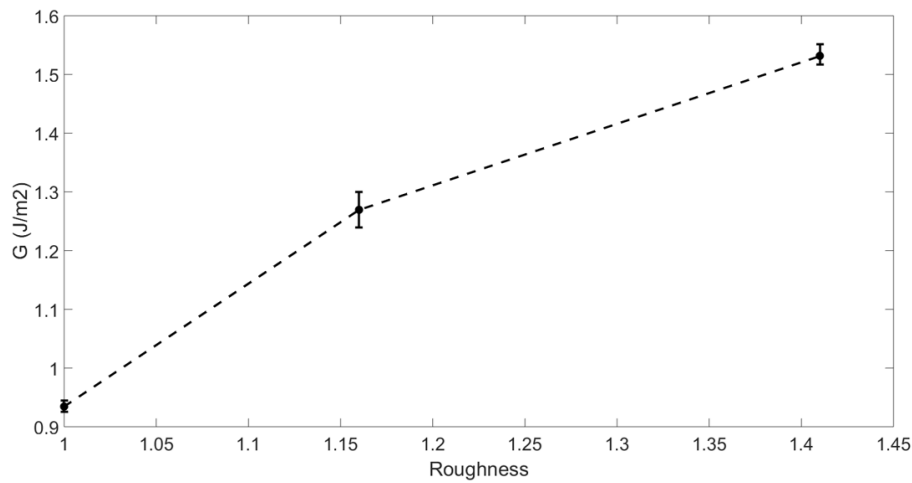


Figure 3.14: Adhesion is proportional to roughness. Data points are the average values of each trail, error bar indicates fluctuation of results on each surfaces.

relationship is not linear, likely because of variation in the rough surfaces versus the average value. We do not expect the length scale of roughness used here, however, to affect fluid flow and the resulting separation.

3.3 Conclusion

This chapter proposed and used a constrained blister test to explore adhesion of soft model tissues to rough and rigid substrates. The constrained height allows the energy to be consumed mostly on breakdown of adhesion. The results suggest that the adhesion strength for this system varies between 0.93 J/m^2 and 1.52 J/m^2 depending on the roughness, with rougher surfaces providing higher adhesion strength. For future experiments the roughest interface with 1.52 J/m^2 is used, allowing a more stable separation and partially mimicking heterogeneous biological tissues. The results also indicate the potential for blister test use in measurement of adhesion strength of actual soft and brittle biological tissues. The test's relatively gentle conditions and lack of direct destructive contact with the sample prevents unexpected tissue damage and related energy depletion.

3.4 References

- [1] K. Kendall, *Journal of Physics D: Applied Physics* **1975**, 8, 1449.
- [2] J. Kim, K. Kim, Y. Kim, *Journal of adhesion science and technology* **1989**, 3, 175–187.
- [3] K.-S. Kim, J. Kim **1988**.
- [4] R. Dauskardt, M. Lane, Q. Ma, N. Krishna, *Engineering Fracture Mechanics* **1998**, 61, 141–162.
- [5] G. Josse, P. Sergot, C. Creton, M. Dorget, *The Journal of Adhesion* **2004**, 80, 87–118.
- [6] H. Dannenberg, *Journal of Applied Polymer Science* **1961**, 5, 125–134.
- [7] J. Hinkley, *The Journal of Adhesion* **1983**, 16, 115–125.
- [8] M. Napolitano, A. Chudnovsky, A. Moet, *Journal of Adhesion Science and Technology* **1988**, 2, 311–323.
- [9] Y. Chu, C. Durning, *Journal of Applied Polymer Science* **1992**, 45, 1151–1164.
- [10] E. P. DeGarmo, J. T. Black, R. A. Kohser, B. E. Klamecki, *Materials and process in manufacturing*, Prentice Hall Upper Saddle River, **1997**.
- [11] J. Leitão, T. Hegdahl, *Acta Odontologica Scandinavica* **1981**, 39, 379–384.
- [12] Y.-S. Chang, Y.-H. Lai, D. A. Dillard, *The Journal of Adhesion* **1989**, 27, 197–211.
- [13] M. Parsons, A. Polyakova, E. Stepanov, A. Hiltner, E. Baer, *The Journal of Adhesion* **1998**, 68, 45–63.
- [14] J. Williams, *International Journal of Fracture* **1997**, 87, 265–288.
- [15] Z. Chen, K. Zhou, X. Lu, Y. C. Lam, *Acta mechanica* **2014**, 225, 431–452.

Chapter 4

Newtonian fluid separation

Cataract is the most widely experienced disease in ophthalmology. It accounts for almost half of human blindness globally, making it one of the biggest health challenges in this era^{1,2}. Because of its pathology, which is closely related to the aging and biochemical change of eye tissues³⁻⁵, cataracts are irreversible. As a result cataract surgery is the only effective way treatment^{6,7}.

The general procedure of cataract surgery includes separation and removal of the failed lens tissue from the surrounding soft tissue in the eye, followed by artificial lens implantation. Lens removal requires successful separation of lens tissues as a critical step that determines surgical success.

In a simplified description, the lens consists of a fragile and elastic capsule that with the actual lens nucleus inside of it, and the nucleus is where the cataract forms. Lens nucleus and capsule initially closely attached to one another at the cell-level by biological adhesion. In surgery the capsule needs to stay in the eye and remain

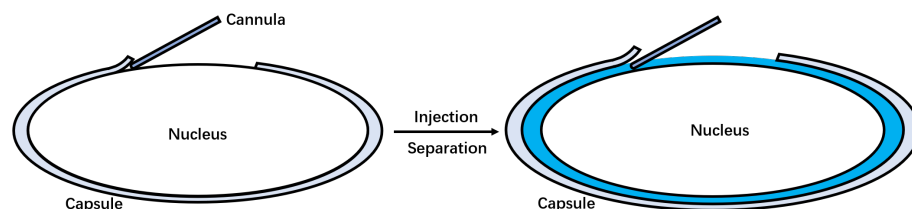


Figure 4.1: Simplified eye lens model and schematic of cataract surgery process. Blue color represents injected fluid.

intact, while the nucleus must be safely separated from the capsule and removed (Fig.4.1).

The removal is done by injecting fluid into the gap between capsule and lens tissues to create hydraulic pressure and achieve separation. The most commonly used injection fluid is balanced salt solution (BSS)⁸. The most significant complication possible during cataract surgery is damage to or rupture of the capsule^{9,10}. When either happens, permanent loss of sight can result, so there is a need to characterize the physical aspects and safety of lens tissue separation. Studies of lens mechanical properties suggest that the maximum strain a capsule can withstand may be as low as 29.4% to 40%^{5,11}, providing a basis for more formal study of the separation process and dynamics in cataract surgery.

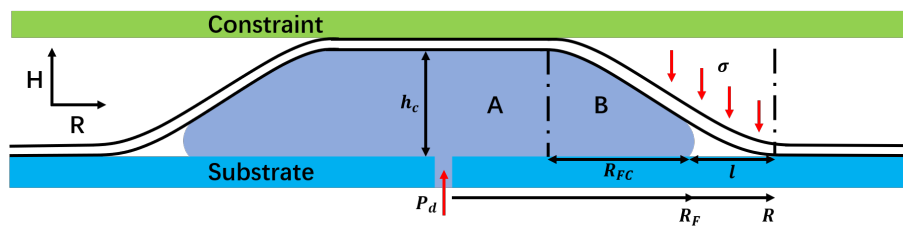


Figure 4.2: Schematics and dimensions of our hydraulic fracture model. Inside the blister is the fluid, at the front of the fluid is a vapor tip with no fluid inside.

4.1 Theory

In an interesting parallel, the separation process in cataract surgery can be considered as hydraulic fracture - a formation of blister or peeling of a soft elastic sheet from an adhered substrate caused by a pressurized flowing fluid (Fig.4.2). In this model, there is a vapor tip existing (discussed later), used to balance the pressure in calculation. Note that in real experiments the length of tip l is normally 2 magnitude shorter than the total radius and thus can be neglected. This makes $R_F = R_F + l = R$ and $R_{FC} = R_{FC} + l$. Using such an analogy allows us to adapt existing theories of

fracture to describe our system. The dynamic radius during the separation can be described by:

$$R_F(t) = \frac{R_{FC}}{2} + \frac{1}{6} \sqrt{\frac{36Qt}{\pi h} - 3R_{FC}^2} \quad (4.1)$$

The blister can be divided into a constrained region (A) and deforming region (B) (Fig.4.2). The profile of (B) can be described by

$$h(x) = h_c \left(1 - \frac{r^2}{R_{FC}^2(t)} \right)^2 \quad (4.2)$$

where $x = r$ follows a fixed coordinate pointing from the entry of fluid to the edge of the blister (e.g. $x = r = R_F$ means x is at the fracture front). h_c is the constrained height of the blister. Equation suggests that with different deforming length R_{FC} there is different blister profile.

With constrained height a constant, R_{FC} can be expressed by a function of viscosity and flow rate^{12,13}.

$$\frac{R_{FC}}{h_c^{0.75}} = \frac{1.52}{0.41^{0.75}} \left[\frac{B^3}{(12\mu)^2\sigma} \right]^{1/12} Q^{-1/6} \quad (4.3)$$

This suggests that when viscosity and flow rate are constant, the blister will have a static profile, regardless of the separation process.

To further analyse the performance of separation for these studies based on the blister profile, a key criterion is the deformation of the tissue during separation, as it will determine the danger of rupture based on mechanical tissue failure. To do so, we introduce a vapor tip hydraulic fracture theory proposed by Ball and Neufeld, and Wang and Detournay in their own studies.

Hydraulic fracture in general uses hydraulic pressure of flowing fluids to break the attachment between two materials, create a gap and enlarge it¹⁴. In Ball and

Neufeld's and Wang and Detournay's theory, such fracture happens with the existence of a vapor tip at where fracture occurs (Fig.4.2 $l : R_F \rightarrow R$). Besides, the fracture is defined to be a viscosity dominated fracture, meaning that fracture deformation depends on the conditions of fluid at the fracture front. The viscosity dominates when the elasticity of the tissue and adhesion is relatively small that they causes minor effects on fluid pressure. The dominating equations for this system are the lubrication equation in flowing fluid and beam bending equation at the vapor tip (as discussed in Section (2.5.1)). At the fracture tip the tissue has the biggest deformation, which can be quantified by the curvature at the front, a useful variable to describe the the deformation caused by beam bending. Generally bigger curvature means bigger deformation. By balancing the equations Ball and Neufeld and Wang and Detournay proposed same form of equations to describe the radius and height of a blister:

$$R_F(t) = 1.52 \left[\frac{B^3 Q^7}{(12\mu)^2 Q^2} \right]^{1/30} t^{3/10} \quad (4.4)$$

and

$$h(0, t) = 0.41 \left[\frac{(12\mu)^2 \sigma Q^8}{B^3} \right]^{1/15} t^{2/5} \left(1 - \frac{r^2}{R_{FC}^2(t)} \right)^2 \quad (4.5)$$

Combining these two equations by making $r=0$ in Equation 4.5 and cancelling the time scale t gives Equation 4.3, which can be transformed into

$$R_{FC} = \frac{1.52 \cdot h_c^{3/4}}{0.41^{3/4}} \left[\frac{B^{1/4}}{(12\mu)^{1/6} Q^{7/30} \sigma} \right] \quad (4.6)$$

Substitute into general expression for curvature¹⁵ $\kappa = \frac{8h_c}{R_{FC}^2}$, there is

$$\kappa = \frac{8h_c}{R_{FC}^2} = \frac{0.909}{h_c^{1/2}} \left[\frac{(12\mu)^{1/3} Q^{7/15} \sigma}{B^{1/2}} \right] \sim \mu^{1/3} Q^{7/15} \quad (4.7)$$

which shows the curvature of tissue at the fracture front. The equation giving a positive dependency of tissue curvature on the viscosity and flow rate of the fluid injected to separate them. In short, both more viscous fluid and faster flow rate will cause the fluid to bend the tissue to a bigger curvature and thus bigger deformation. This is the fracture behavior of viscosity dominated hydraulic fracture.

Overall there are currently three main obstacles to successful cataract surgery: 1. The adhesion between the two tissues is unknown and variable, and there is no accurate measurement of corticocapsular adhesion.¹⁶; 2. The flow parameters in a surgery such as pressure and flow rate are not quantified or prescribed, surgeons tend to use a small volume of fluid and inject gently (subjectively judged) to prevent potential danger; 3. The performance of different fluids used in the surgery is not quantified except based on surgical outcomes. In Chapter (3), the blister test has been validated to have potential in measuring corticalcapsular lens adhesion.

This chapter focuses on the performance of Newtonian fluids, specifically water and glycerin, on the separation effectiveness and safety to provide a baseline understanding of the flow and impact of key rheological variables. A bi-layer injection model of gelatin and PDMS polymer gels is used to mimic the eye tissue. Here water has the same rheology as BSS and glycerin is used as an easily manipulated Newtonian fluid to study the effects of viscosity.

4.2 Materials and methods

4.2.1 Experimental set-up

The injection model consists of a bi-layer structure. The top layer is made of 15% w/w gelatin (Young's modulus¹⁷ $E=16000$ Pa) to mimic the eye lens capsule and the

bottom layer (PDMS 1:10) mimics the nucleus. Water ($\mu = 8.9 \times 10^{-4} \text{Pa} \cdot \text{s}$) and 40% glycerin ($\mu = 3.8 \times 10^{-3} \text{Pa} \cdot \text{s}$) are used to study the effects of viscosity.

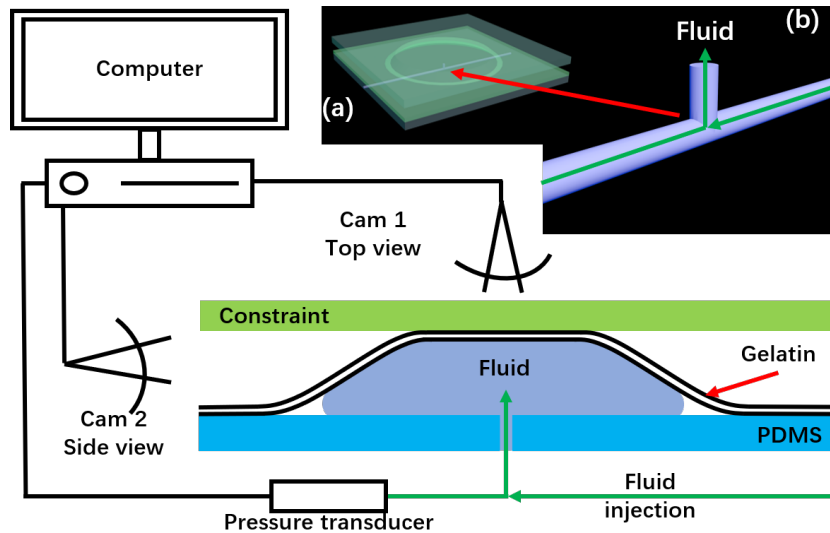


Figure 4.3: Schematic of experimental set-up and sample structure. Pressure transducer reads and records the pressure at the entry of the fluid into the micro-channel; compressed air is used to pressurize the liquid in the syringe and push it into the model. (a) 3D structure of injection model, bright green ring indicates the edge of blister where separation happens; (b) T-shape mould used for templating the micro-channel in the base layer.

Fig.4.3 shows a schematic of the experimental set-up. A glass slide is placed approximately 2.5 mm above the pre-made injection model to constrain the maximum height the gelatin layer can lift up. In an experiment, the injection model is connected to a pressure transducer and syringe via the two ends of the micro-channel. Compressed air pressurizes the fluid in the syringe and moves the liquid. The pressure transducer monitors instantaneous pressure and records it digitally. Two cameras are used to capture the top and side view of the experiment. The top view shows the extent of separation while the side view shows the profile of the tissue being separated.

4.2.2 Curvature analyses

The curvature is measured directly from the images of blister profile. The data processing and curvature measurement apply software ImageJ and MATLAB. Analysis is done by below procedure:

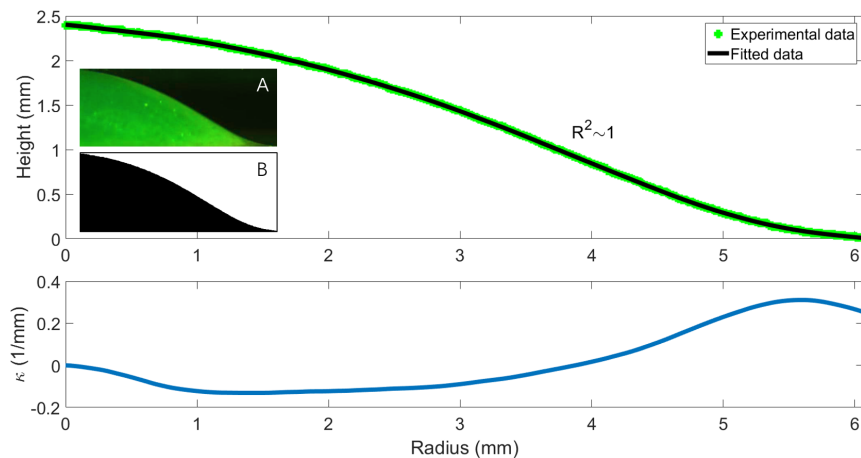


Figure 4.4: Curvature processing of blister profile. A: Raw image captured with camera. B: Binary image of A for quantification. Green color indicates experimental data extracted from B and black curve is the fitting by Equation (4.2). Curvature is taken at its maximum value.

- The blister image is obtained directly from experiment-setup camera (Fig.4.4 (A))
- It is input into ImageJ and converted to binary image with only black and white color (Fig.4.4 (B))
- The scale of B, 79.78 pixels/mm, is set in ImageJ allowing B to be digitized and exported to a coordinate (Fig.4.4 Green color)
- This data is then input into MATLAB and fitted by Equation (4.2), with the fitting $R^2 \sim 1$ (Fig.4.4)

- The curvature curve is then computed by MATLAB with code in Appendix (A), and the maximum value is also selected automatically as the curvature at the fracture front

The raw images are captured with a resolution that gives 79.78 pixels/mm scale, meaning that the minimum observable length unit being 0.0125 mm. This length scale is small enough for accurate curvature measurement and will be discussed in more details in Chapter (5). The fitting accuracy is shown to have $R^2 \sim 1$ which means a perfect fitting. Comparing the values of experimental data and fitted data the difference (error) in average is within 0.3% of the original data.

4.3 Results and discussion

Firstly, the effectiveness of separation is analysed by the separation radius. Equation (4.1) gives a good fit to the radius (Fig.4.5 (left)). Transforming this into a log axis one can find that, despite using different flow rates, all experiments show common trends of radius propagation in a steady state manner. From Equation (4.1) it is clear that $R \sim \sqrt{\frac{Qt}{\pi h}}$ and thus all radii are normalised by $R/\sqrt{Q/\pi h}$ which returns a general relationship between t and R (Fig.4.6).

It can be seen that after the initial transient, all radii collapse to the same line presented by $t^{1/2}$. This is valid for both water injection and 40% glycerin injection, meaning that for narrow gap flows, viscosity is not the dominant factor in blister propagation. In the beginning the radius does not follow a common pattern, likely because the flow is in a transient process as the fluid starts to form a stable front. In Chapter (3), results of pressure reading in adhesion measurement show a peak value when the blister first forms, and the propagation and corresponding pressure release are plotted in Fig.3.9. Depending on the flow rate, the pressure decays at a different pace. Before the pressure drops from the peak value to a constant steady

state value, the transient pressure equilibration drives the flow in the blister and the radius does not propagate in a uniform pattern.

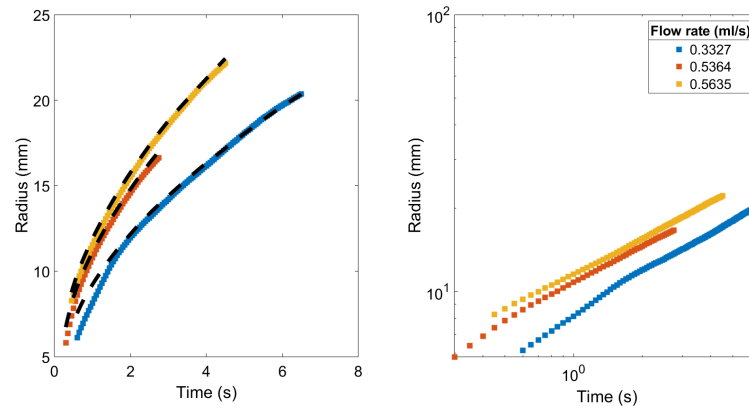


Figure 4.5: Radius of water injection at three flow rates. Blacked dashed curves indicates the fitting of Equation (4.1). Left: original radius data. Right: radius adjusted to a log axis.

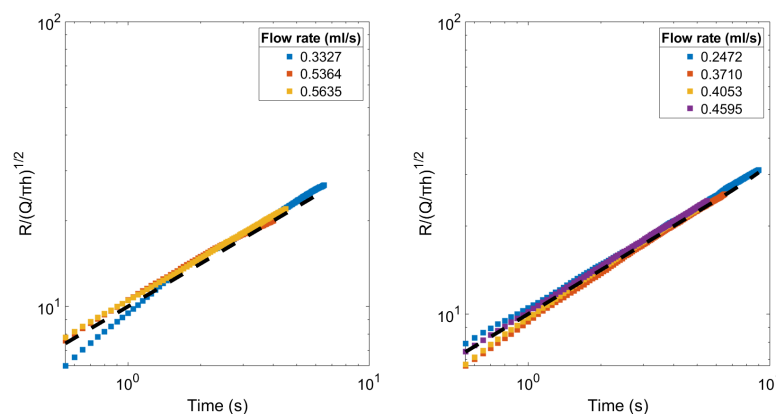


Figure 4.6: Normalised radius shows a trend of $t^{0.5}$ (black dashed line). Left: water injection. Right: 40% glycerin injection.

While higher fluid flow rates will cause faster separation, the flow rate also affects the blister profile and thus deformation. According to Equation (4.3), when the height is fixed, higher flow rate will give a smaller R_F (Fig.4.7 (left)). For the extent of our experiments such difference would not affect the overall radius change as the volume difference caused by changing profile can be neglected compared

to the total volume of the blister. However, this affects the deformation of blister tissue. As fluid is injected, it generates a pressure at the fracture front to lift the tissue. The initial pressure that drives the fluid increases as flow rate increases. The pressure drop along the horizontal direction of propagation calculated from $h^2(dP/dr) = 12\mu V$ is two magnitudes smaller than the initial pressure, making the pressure at the fracture front still higher when flow rate is faster.

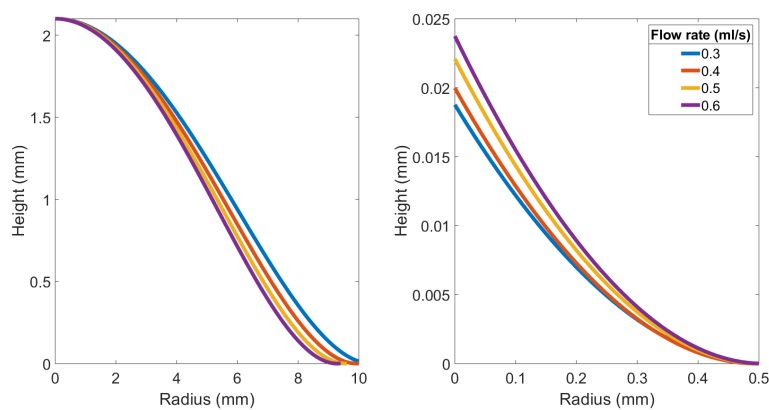


Figure 4.7: Equation describing the relationship between flow rate and blister profile. Left: whole profile calculated with four flow rates. Right: zoom-in of fracture front with normalized radii.

The tissue deformation is characterised by the shape and curvature of the fracture front (Fig.4.7 (right)). Normalising the radius of the front with different flow rates to the same distance one can find that at faster flow rates the tissue is lifted higher, which gives a bigger curvature of the tissue as the local height approaches zero. Applying Equation (4.7) the theoretical curvature as a function of flow rate can be derived. Cancelling the pre-factor shows a trend of curvature-flow rate dependency (black dashed curve in Fig.4.9).

Direct measurement of curvature for water and 40% glycerin separation gives the same results. Fig.4.8 right shows a steeper change of height when flow rate is faster. Also when viscosity is higher the blister becomes steeper. Fitting the profiles

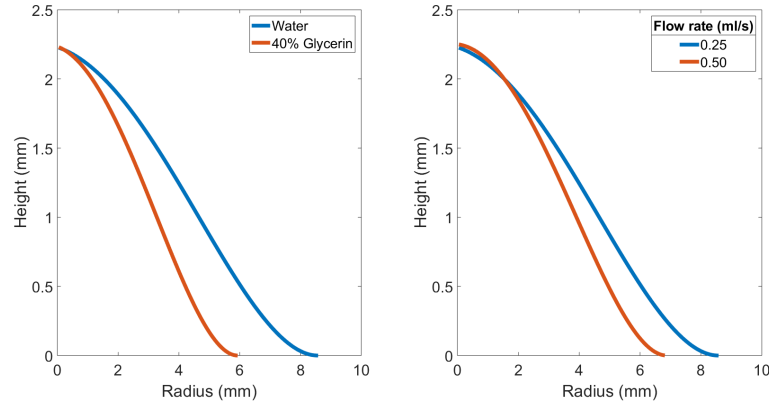


Figure 4.8: Blister profile depends on the viscosity and flow rate of the fluid. Left: Water and 40% glycerin injected at 0.2 mL/s. Right: profile of water injected at different flow rates.

obtained in experiments to the bell-shape theory $h(x) = h_c \left[1 - \frac{r^2}{R_{FC}^2(t)} \right]^2$, then applying equation ¹⁵ $\kappa = |h''|/(1+h'^2)^{3/2}$ at the fracture front allows the curvature to be measured (Fig.4.9).

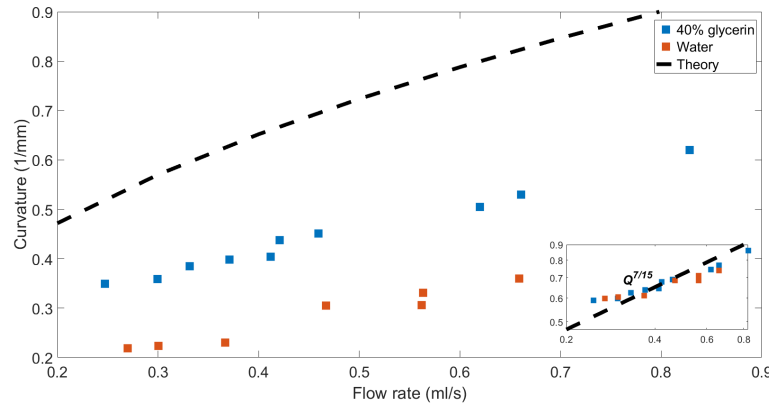


Figure 4.9: Curvature as a function of flow rate. Inset: normalized curvature in a log coordinate showing that the dependency of curvature on flow rate follows $Q^{7/15}$.

The curvature of blisters formed by both water and 40% glycerin follows the same trend of $\kappa \sim Q^{7/15}$, however the scale is not similar. The reason may be that for the theoretical expression $\kappa = a \cdot Q^{7/15}$, the pre-factor a is mainly affected by the viscous pressure drop which is derived from lubrication theory, and this depends

on the shape of the blister. In theory as the blister has a semi-spherical shape the pressure drop caused by the viscous drag force is different from when it is in a frustum shape. As velocity and height are constant, a semi-spherical blister would have a shorter radius and thus the total pressure drop along the direction of propagation would be smaller and thus cause bigger curvature. By using a power-law fit the actual curvature expressions of 40% glycerin and water follow $\kappa = 0.6505 \cdot Q^{7/15}$ and $\kappa = 0.4516 \cdot Q^{7/15}$ respectively.

This chapter provides a characterisation of the basic hydrodynamic aspects of tissue separation by viscous fluids. It relates to one of the more common, and safe procedures for real cataract surgery when balanced salt solution. We propose that the safe threshold for general surgery performance be related to the upper limit of strain of the eye lens capsule, typically considered to be 35%^{4,18}. Most of the patients who receive this surgery are elders and the thickness of lens capsule increases with age to a maximum value of 33 μm ⁵. The Young's modulus of capsule tissue also varies to 1.5×10^6 Pa in 90 s¹¹. Applying the bending stiffness equation $B = Ed^3/12(1 - \nu^2)$, the modulus becomes 6 Pa \cdot mm³. Knowing these, and also knowing the conditions of lens capsule deformation during cataract surgery, the curvature can be re-scaled to find a safety threshold. We calculate it using the parameters of the eye lens capsule to determine that a safe injection flow rate using water would be 8 $\mu\text{L/s}$ and this would ensure that the strain of capsule tissue is under 35%, safe for all patients.

4.4 Conclusion

This chapter proposed a viscosity-dominated hydraulic fracture process for eye lens capsule removal. The effectiveness of separation is studied for a blister with constrained height. The radius equation is revised to show a flow rate dependency.

At higher flow rates the separation is more effective and this follows $R \sim \sqrt{Qt/\pi h}$. Deformation of tissue as a result of varying viscosity and flow rate in Newtonian fluid injection is studied and it is found that both the increase of these two parameters will cause an increase of tissue curvature at the fracture front, increasing deformation and rupture risk. This trend can be roughly described by $\kappa \sim \mu^{1/3} Q^{7/15}$. This finding can be applied to current cataract surgery which mostly uses injected balanced salt solution (BSS). For BSS it would be good to control or set an upper limit to the flow rate so that the deformation does not threaten human eye tissue safety. The results also provide a general idea of the safe range of BSS injection which may aid the performance of cataract surgery.

4.5 References

- [1] G. Tabin, M. Chen, L. Espandar, *Current opinion in ophthalmology* **2008**, 19, 55–59.
- [2] AIHW, *Elective surgery waiting times 2014-15 : Australian hospital statistics*, Australian Institute of Health and Welfare, Canberra, **2015**.
- [3] K. J. Cruickshanks, B. Klein, R. Klein, *American journal of public health* **1992**, 82, 1658–1662.
- [4] S. Krag, T. T. Andreassen, *Progress in retinal and eye research* **2003**, 22, 749–767.
- [5] S. Krag, T. Olsen, T. T. Andreassen, *Investigative ophthalmology & visual science* **1997**, 38, 357–363.
- [6] L. A. Remington, D. Goodwin, *Clinical anatomy of the visual system E-Book*, Elsevier Health Sciences, **2011**.
- [7] A. I. Jobling, R. C. Augusteyn, *Clinical and experimental optometry* **2002**, 85, 61–75.
- [8] V. Vasavada, V. A. Vasavada, L. Werner, N. Mamalis, A. R. Vasavada, A. S. Crandall, *Journal of Cataract & Refractive Surgery* **2008**, 34, 1173–1180.
- [9] A. Vasavada, S. Raj, V. Vasavada, S. Shrivastav, *Eye* **2012**, 26, 761–770.
- [10] Y. Ghosh, G. Kirkby, *Eye* **2008**, 22, 844–848.

References

- [11] R. Fisher, *The Journal of physiology* **1969**, 201, 1–19.
- [12] T. V. Ball, J. A. Neufeld, *Physical Review Fluids* **2018**, 3, 074101.
- [13] Z.-Q. Wang, E. Detournay, *Journal of Applied Mechanics* **2018**, 85, year.
- [14] D. Garagash, E. Detournay, *J. Appl. Mech.* **2000**, 67, 183–192.
- [15] M. Kline, *Calculus: an intuitive and physical approach*, Courier Corporation, **1998**.
- [16] A. R. Vasavada, D. Goyal, L. Shastri, R. Singh, *Journal of Cataract & Refractive Surgery* **2003**, 29, 309–314.
- [17] A. D. Doyle, J. Lee, *Biotechniques* **2002**, 33, 358–364.
- [18] H. B. Dick, S. E. Aliyeva, F. Hengerer, *Journal of Cataract & Refractive Surgery* **2008**, 34, 1367–1373.

Chapter 5

Shear-thinning fluid separation

In Chapter (4) we examined the use of Newtonian, viscous fluids as fracturing fluids for soft model tissues. Viscosity dominated the behaviour of viscous fluids, but more complex fluids are also used in cataract surgery.

A widely used technique in cataract surgery is viscodissection, which uses viscoelastic hyaluronic acid polymeric solutions, that exhibit shear-thinning rheology, to separate the lens nucleus and capsule tissue¹⁻³.

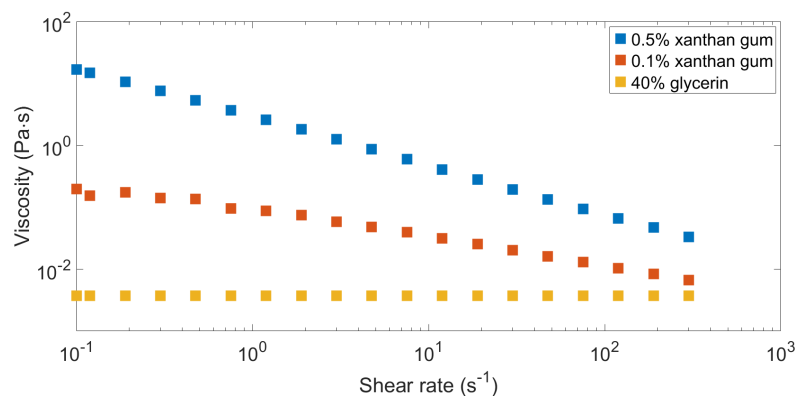


Figure 5.1: Flow curve of 0.1%, 0.5% xanthan gum and 40%g glycerin. The viscosity of xanthan gum increases as shear rate decreases, while for glycerin the viscosity is constant as it is a Newtonian fluid nature.

Shear-thinning fluids have unique flow behavior when compared to Newtonian fluids, as they decrease in viscosity as their rate of deformation or shear rate increases (Fig.5.1 0.1% and 0.5% xanthan gum). Said another way, the faster a shear-thinning fluid flows, the less resistance and viscous drag it offers.

Applying this to cataract surgery, this eases injection, as hypodermics and can- nula have narrow widths and impart large shear rates, minimising resistance to injection. Once inside the eye tissue, however, the viscosity increases and provides a stabilising force to maintain separation as it occurs inside the lens, preventing it from collapsing. Historically the technique has been suitably safe, but the dynam- ics of soft tissue separation and fracturing by shear-thinning fluids has not been studied quantitatively from a rheological perspective⁴⁻⁶.

Existing assessment of viscodissection fluids is primarily based on grading by experts that rates the effectiveness of surgical shear-thinning fluids by “difficulty”. A widely used criterion for safety is the tissue rupture rate among all surgical cases. The rupture rate overall is rare but when it happens the eye lens will be permanently damaged. Among all the rupture cases, 61% can be related to the mishaps of the use of viscous fluids⁷. For more robust understanding and design applications, it is also worthwhile to quantify separation driven by shear-thinning fluids and to assess boundaries for safe operations.

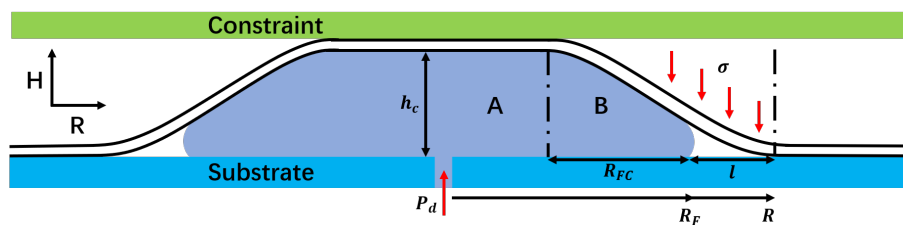


Figure 5.2: Schematics and dimensions of hydraulic fracture model

5.1 Theory

The location of the fracture front (radius for a radially propagating blister) and the fracture rate (velocity at the fracture front) have been discussed in Chapter (4). A general description of the dimensions in this problem is as Fig.5.2. Overall the

radius of the fracture front can be reproduced by:

$$R_F(t) = \frac{R_{FC}}{2} + \frac{1}{6} \sqrt{\frac{36Qt}{\pi h} - 3R_{FC}^2} \quad (5.1)$$

which gives that $V = dR_F/dt \sim \sqrt{Q/2\pi ht}$.

In a general shape, the blister profile of the deforming region can be modelled by:

$$h(x) = h_c \left(1 - \frac{r^2}{R_{FC}^2(t)} \right)^2 \quad (5.2)$$

The safety of dissection, as related to the deformation of the soft tissue at the fracture front, can be quantified by the curvature of the tissue there. A model can be derived from the Newtonian fluid separation case showing the dependency of curvature on flow rate and viscosity at the fracture front^{8,9}:

$$\kappa = \frac{8h_c}{R_{FC}^2} = \frac{0.909}{h_c^{1/2}} \left[\frac{(12\mu)^{1/3} Q^{7/15} \sigma}{B^{1/2}} \right] \sim \mu^{1/3} Q^{7/15} \quad (5.3)$$

For shear-thinning fluids, the curvature expression can be obtained by applying suitable rheology expressions and solving dimensionless equations accordingly. General scaling of hydraulic fracture is¹⁰:

$$w = \epsilon L_\mu \Omega, \quad \lambda = L_\mu \Lambda, \quad \epsilon = \sigma_0 / E' \quad (5.4)$$

If the shear-thinning behavior is expressed by $\mu = M\dot{\gamma}^{n-1}$, where μ is viscosity, $\dot{\gamma}$ is shear rate, M is power-law consistency, and n is the power-law index, the above equations can be reduced to a form consisting of dimensionless parameters¹¹:

$$w = \epsilon L_n \Omega_n(\xi), \quad \lambda = L_n \Lambda, \quad \epsilon = \sigma_0 / E' \quad (5.5)$$

with the parameters calculated numerically, applying curvature $\kappa = 2w/L_n^2$ there is:

$$\kappa = 2\sqrt{\frac{32}{\pi}} \left(\frac{\sigma_0^{3/2+3/n}}{E'^{7/2+3/2n} M'^{3/2n}} \right) K_{Ic} \frac{1}{V^{3/2}} \sim \frac{1}{V^{3/2}} \quad (5.6)$$

describing the relationship between the curvature κ , fracture rate V and fracture toughness of fractured material K_{Ic} . By modifying the rheology expression to $\tau = M(2\dot{\gamma})^n$, where τ is the shear stress, applying $\kappa = 2w/L^2$ and solving Equations (5.4), curvature can be modelled by¹²:

$$\kappa = 2\Psi \left(\frac{M'}{E'} \right)^{\frac{1}{n+2}} Q_0^{\frac{1}{2}} t^{\frac{1}{2} - \frac{n}{2(n+2)}} \quad (5.7)$$

with $\Psi = 2\zeta_m^2 \Omega_m / L^2$ considered a constant. For a free surface soft material separation, the shape of the blister can be described as a spherical cap, so that the time can be transformed to fracture rate as $t = 3Q_0 / \pi \epsilon_m(t) L_m(t) \Omega_m(0) V^2$. Then the curvature has following relationship:

$$\kappa = \frac{2}{L^2} \left(\frac{3}{\pi \bar{\Omega}_m(0)} \right)^{\frac{1}{n+3}} \zeta_m^{\frac{n+2}{n+3}} \bar{\Omega}_m(\xi) \left(\frac{M'}{E'} \right)^{\frac{1}{2(n+3)}} Q_0^{\frac{n+4}{2(n+3)}} \left(\frac{1}{V} \right)^{\frac{2}{n+3}} \sim Q_0^{\frac{n+4}{2(n+3)}} \left(\frac{1}{V} \right)^{\frac{2}{n+3}} \quad (5.8)$$

This is consistent with Equation (5.3) which is derived from Newtonian fluid solutions: as fracture propagates the fracture rate becomes slower, as a result, the shear rate at the fracture front decreases with time. For shear-thinning fluids, viscosity increases as the shear rate decreases, increasing the deformation of the tissue at the front that we detect through increased curvature.

5.2 Materials and methods

5.2.1 Experimental set-up

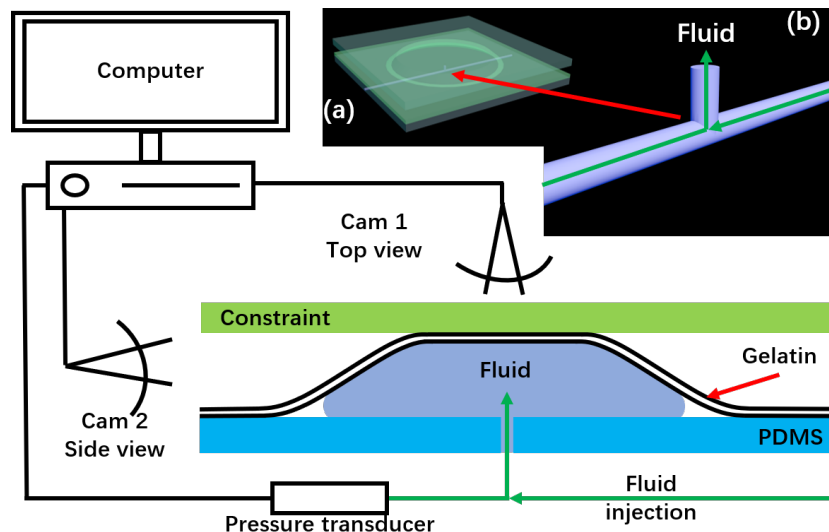


Figure 5.3: Schematic of experimental set-up and sample structure. Pressure transducer reads and records the pressure at the entry of the fluid into the micro-channel; compressed air is used to pressurize the liquid in the syringe and push it into the model. (a) 3D structure of injection model, bright green ring indicates the edge of blister where separation happens; (b) T-shape mould used for templating the micro-channel in the base layer.

The injection model is the same as Chapter (4) with a bi-layer gel structure and microfluidic channel. The top layer is made of 15% gelatin to mimic the eye lens capsule and the bottom layer (PDMS 1:10) is the nucleus. The injected fluid is 0.1% aqueous xanthan gum to study the effects of shear-thinning viscosity.

Fig.5.3 shows a schematic of the experimental set-up. A glass slide is placed approximately 2.5 mm above the pre-made injection model to constrain the maximum height the gelatin layer can reach. For each experiment, the injection model is connected to a pressure transducer and syringe via the two ends of the micro-channel. Compressed air pressurizes the fluid in the syringe and creates pressure

inside the system. The pressure transducer monitors the pressure and digitally records the instantaneous values. Two cameras are used to capture the top and side view of the experiment. The top view shows the extent of separation while the side view shows the profile of the tissue as it separates.

Fluid rheology is measured using a TA Instruments stress-controlled DHR-1 rheometer with a cone and plate geometry with cone and plate geometry (cone diameter 60 mm, angle 2 degrees). Flow curves are performed over a shear rate range of 0.1-300 s^{-1} with flow sweep procedure. Shear stress, shear rate, viscosity and normal stress are all measured.

5.2.2 Curvature analyses

Using the same method as introduced in Chapter (4), the curvature is measured directly from the images of blister profile. The data processing and curvature measurement apply software ImageJ and MATLAB. Analysis is done by below procedure:

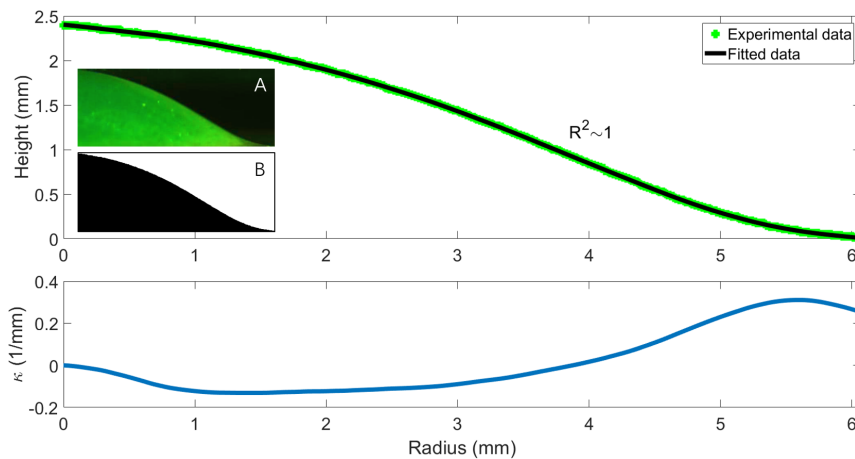


Figure 5.4: Curvature processing of blister profile. A: Raw image captured with camera. B: Binary image of A for quantification. Green color indicates experimental data extracted from B and black curve is the fitting by Equation (4.2). Curvature is taken at its maximum value.

- The blister image is obtained directly from experiment-setup camera (Fig.5.4 (A))
- It is input into ImageJ and converted to binary image with only black and white color (Fig.5.4 (B))
- The scale of B, 79.78 pixels/mm, is set in ImageJ allowing B to be digitized and exported to a coordinate (Fig.5.4 Green color)
- This data is then input into MATLAB and fitted by Equation (4.2), with the fitting $R^2 \sim 1$ (Fig.5.4)
- The curvature curve is then computed by MATLAB with code in Appendix (A), and the maximum value is also selected automatically as the curvature at the fracture front

The raw images are captured with a resolution that gives 79.78 pixels/mm scale, meaning that the minimum observable length unit being 0.0125 mm. This length scale is small enough for accurate curvature measurement and will be discussed in more details in Chapter (5). The fitting accuracy is shown to have $R^2 \sim 1$ which means a perfect fitting. Comparing the values of experimental data and fitted data the difference (error) in average is within 0.3% of the original data.

5.3 Results and Discussion

Like Chapter (4), we still start with discussing separation effectiveness. This separation performance is characterised using the blister radius, which reflects the separation area. Generally, increasing the flow rate increases the overall area separated. From Equation (5.1) we see that $R \sim \sqrt{\frac{Qr}{\pi h}}$. We compare this to experimental results by plotting the separation radius formed by three fluids with different

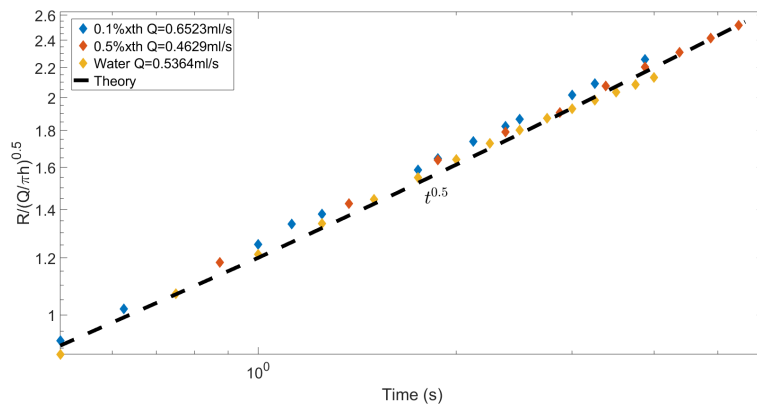


Figure 5.5: Normalized radius versus time for different fluids plotted in a log axis. The black dashed line indicates $t^{0.5}$.

rheological properties and flow rates. The radii are normalized by $R/\sqrt{Q/\pi h}$ and plotted against time (Fig.5.5). Despite differences in the flow rate and rheological properties, the radii of all three fluids show the expected scaling with $t^{1/2}$. The universal behaviour indicates that the radius of blister undergoing separation is not affected by fluid viscosity as much as its flow rate. For shear-thinning fluids the viscosity varies during the whole separation, but the theoretical shape factor $q = 1 - R_{FC}/2R_F$ ^{13,14} indicates that viscosity causes less than 3% variation to the overall radius. As radius increases we expect this difference to decrease further, so Equation (5.1) can be used as an expectation for the experiments and surgeries.

Though viscosity has a very minor effect on the dynamic progression of the separation radius, we also need to quantify any rheology effects on the blister deformation. The dynamic blister profile is extracted from the side view videos. Fig.5.6 shows the dynamic profile of the deforming region of an advancing blister separated by 0.1% xanthan gum. We expect from theory (Equation (5.1)) and observation that as separation progresses, fracture front velocity becomes slower. For Newtonian fluids the decrease in velocity does not affect the fluid rheology, but here shear-thinning fluids have a distinct response to local shear rate: increased viscosity. The

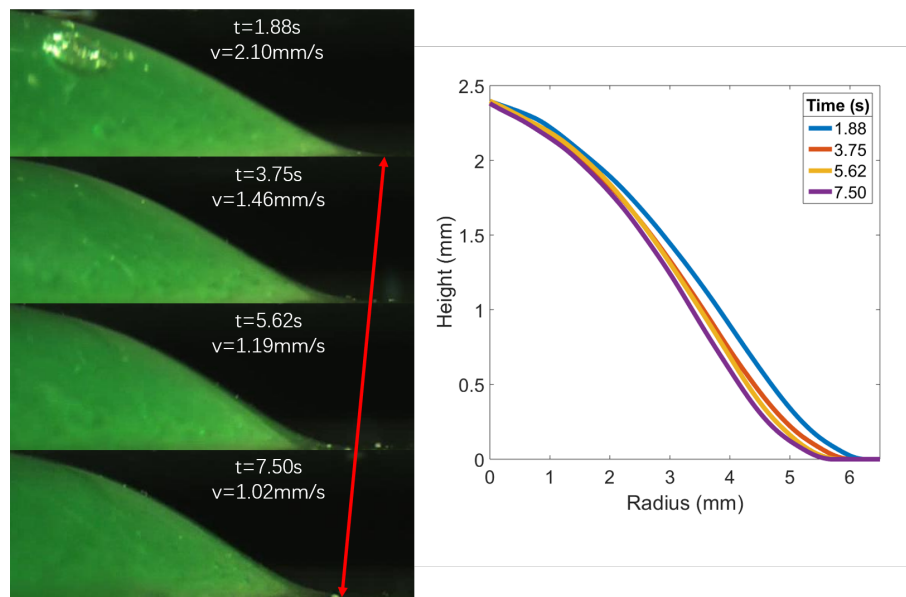


Figure 5.6: Microscope photos and curve of the fracture front of an advancing blister as the profile becomes increasingly steep, indicating an increased deformation with time. Tested with 0.1% xanthan gum at 0.23 mL/s.

change in fracture front velocity thus causes a narrowing of the cross-section of flow within the deforming region of the blister, affecting tissue deformation. The effects can be seen directly from the profile curve in Fig.5.6 showing the change in blister shape with time. Based on the figure, we note that the maximum difference of separation radius caused by the shear-thinning fluid versus Newtonian fluids is roughly 0.5 mm, which is only 2% of the total radius of $R_F = 25\text{mm}$. Also as is discussed below in Fig. 5.9, the effective length for curvature measurement in the range of our experiment is smaller than 0.5 mm, which means the fitting is capable of reflecting the true curvature.

When the dynamic blister profiles are normalised to the same radius (Fig.5.7), they all collapse onto a uniform shape which can be described by the approximation Equations (5.2), especially at the very front of the blister. This makes sense from lubrication theory, Equations (2.3) and (2.5), as the fluid rheology has most impact on the deformation of the tissue.

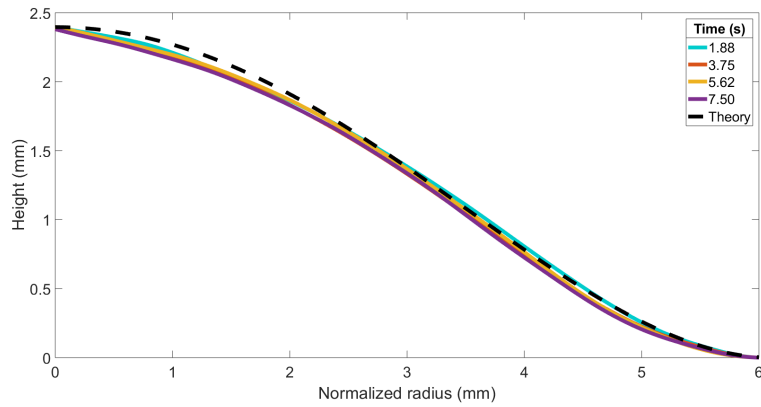


Figure 5.7: Blister profile normalized by maximum radius to the same radius. The black dashed curve represents the theoretical fit from a bell-shaped curve theory.

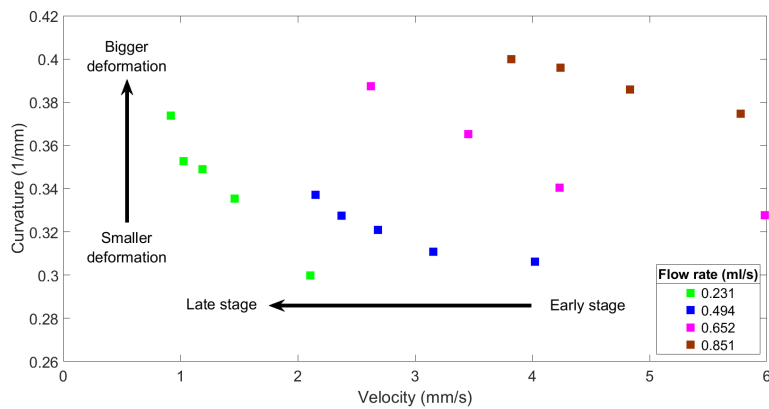


Figure 5.8: Dynamic curvature as a function of blister fracture front propagation speed. Starting from fast velocity the curvature increases as velocity drops.

A plot of the blister profile shows a direct observation of the deformation dynamics in the fracture front region, and we can use the curvature to quantify the deformation. Fig.5.8 plots the curvature as a function of time at different flow rates. Note that each of the flow rates is one individual separation process, and in each case as separation continues the velocity will decrease, which means the right side of the figure represents short times and the left long times. Larger curvature means higher tissue deformation. Fig.5.8 shows that in each separation, the deformation gradually increases as flow of injected fluid, and fracture rate, decreases. The trend is consistent with a fluid that increases in viscosity as it slows down, shear-thinning, meaning the greater extent of fluid infiltration alters the effect on the soft tissue. Also, as with Newtonian fluids, higher flow rates cause an increase in deformation. Equation (5.3) shows a correlation between curvature and viscosity and flow rate and curvature that is consistent with our data, so we can use these data and the theory to assess surgical techniques.

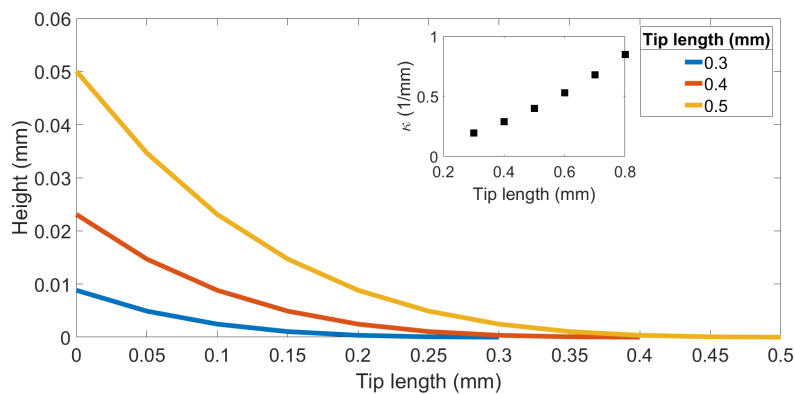


Figure 5.9: Theoretical profile of the fracture front calculated by Equation (2.6) with different tip lengths. The higher the tissue is lifted the more the tissue is deformed, as well as the longer the length would be. Inset shows longer length gives bigger curvature.

The larger deformation observed can be explained by examining the fracture tip length. At the fracture front we think of the tissue as behaving like an elastic

solid, described by a simple bending model. In such a model, the fluid front and the substrate at the blister front act as two stands that support the tissue. Since the pressure at the vapor tip is zero, the tissue is bent by a uniformly distributed compression stress σ acting normally to the tissue.

In the experimental set-up presented previously, σ becomes the atmospheric pressure which has a value of 1.01×10^5 Pa. If $\sigma = P$ in Equation (2.6) ($B \nabla^4 h = P$) the length of the vapor tip becomes a function of the height at the fluid front. Generally higher pressure will then lift the tissue more, which then increases the length. With different tip lengths we find different fracture front profiles, with longer ones tending to be bent more significantly (Fig.5.9). Once the profile is obtained, curvature can be calculated by $\kappa = 2h_F/L^2$. Equation (5.3) is a Newtonian form of the curvature expression $\kappa = 2h_F/L^2$ for the convenience of engineering calculation, which shows that the increase of flow rate and viscosity at the front will cause a bigger curvature and deformation. This is in consistent with the results displayed in Fig.5.8 but it is based on the Newtonian fluid assumption that flow rate and viscosity are constant during the separation, which causes a static fracture tip profile. It is still necessary to discuss dynamic aspects of non-Newtonian fluid fracture behavior as we know that the viscosity at the fracture front changes significantly (Fig.5.10).

It is clear from Fig.5.10 that Newtonian fluids 40% glycerin and water both have a constant viscosity at the shear range of the experiments, while for shear-thinning 0.1% xanthan gum the viscosity has shown an almost four-folds increase from high shear to low shear. This is because of the decay in fracture rate, which determines the shear rate at the fracture front, with slower fracture rate the shear rate is lower. According to Equation (5.3) such change tends to cause roughly 130% difference between the smallest and biggest curvature. Applying this in Fig.5.8 we found that the range of curvature has shown a similar ratio with roughly 133% difference. To

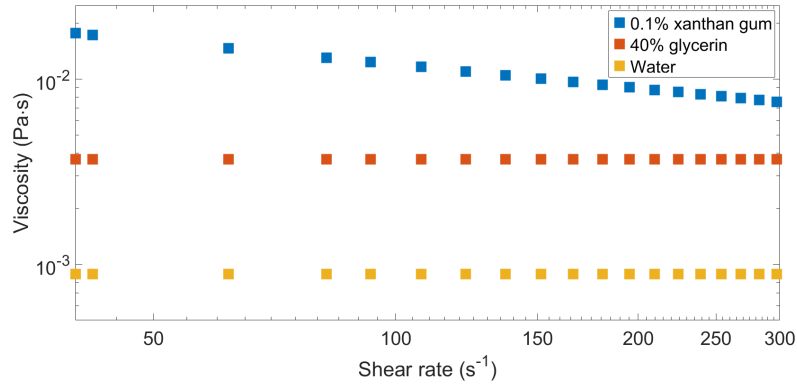


Figure 5.10: Rheology of 0.1% xanthan gum, 40% glycerin and water in the range of shear rate observed from our experiments. The viscosity of 0.1% xanthan gum has almost four-folds increase between the lowest and highest values.

further justify the effects of viscosity, we apply lubrication equations for both Newtonian fluids and shear-thinning fluids (Equations (2.3) (2.5)) to calculate the pressure gradient in the blister caused by such difference in viscosity. These two equations comparable and interchangeable as if we adapt Newtonian fluid expression $\tau = M\dot{\gamma}$, $n = 1$ and $M = \mu$ in Equation (2.5) ($\frac{dP}{dx} = 2^{n+1}(\frac{2n+1}{n})^n \frac{MV^n}{h^{n+1}}$), then it becomes Equations (2.3) ($\frac{dP}{dx} = 12\mu/h^2V$).

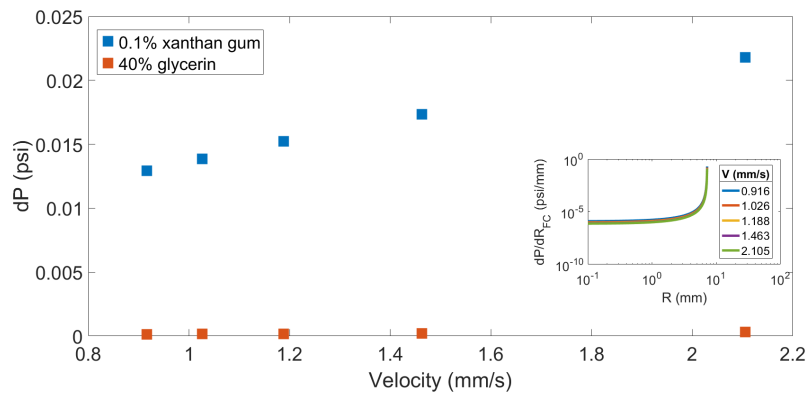


Figure 5.11: Pressure loss and pressure gradient in blister for 40% glycerin and 0.1% xanthan gum. Inset is the pressure gradient of blister separated by 40% glycerin during the process. In the separation process the velocity keeps dropping.

Fig.5.11 shows an example of the pressure gradient with 40% glycerin and the total pressure loss in the blister for both 40% glycerin and 0.1% xanthan gum. The pressure loss is an integration of the pressure gradient shown in the inset. From the results we see that with constant viscosity, 40% glycerin has only a very minimum change in pressure during the separation, while for shear-thinning 0.1% xanthan gum the difference is much more significant. As the curvature is essentially determined by the pressure so with very small pressure difference the curvature of Newtonian fluids is expected to be almost static. Likewise, higher pressure difference then causes a dynamic curvature as measured with 0.1% xanthan gum.

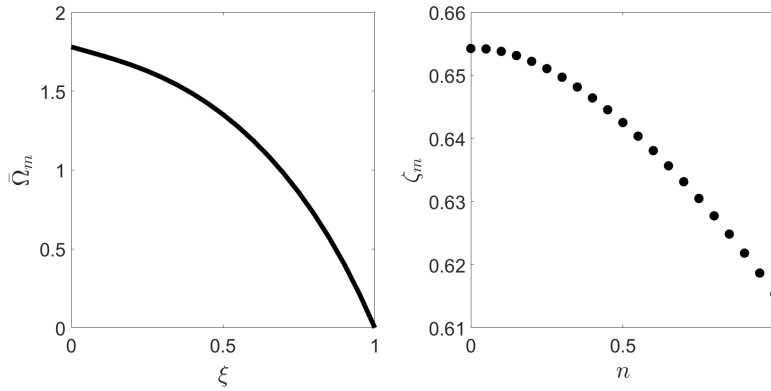


Figure 5.12: Published data of dimensionless opening parameter $\bar{\Omega}_m$ and ζ_m extracted from Adachi and Detournay's paper. $\bar{\Omega}_m$ is obtained at power law index $n=0.6$, while n is determined from the rheology data of 0.1% xanthan gum. ζ_m value depends on n solely so we take also at $n=0.6$. ξ is the adjusted coordinate with $\xi = 1$ the location of the fracture front tip. n is the power-law index exponent.

Equation (5.8) is a dimensionless curvature approximation accounting for the effects of flow rate and dynamic fracture rate, as well as power-law parameters which describe flow-induced changes to the rheology of non-Newtonian fluids. It indicates that an increase of flow rate and decrease of fracture rate can cause bigger deformation, represented by an increased curvature. Comparison of the experimental results and the curvature calculated by this equation can be performed

using literature values of the dimensionless parameters $\zeta_m = 0.63696$ and $\bar{\Omega}_m = 0.046$ (Fig.5.12). Dimensionless opening $\bar{\Omega}_m$ is obtained at power law index $n=0.6$, while ζ_m only depends on n so we take it also at $n=0.6$. The power-law parameters are obtained from experimental rheology data of 0.1% xanthan gum. The flow rate and velocity are then used to calculate a dimensionless curvature and compare with experimental data (Fig.5.13).

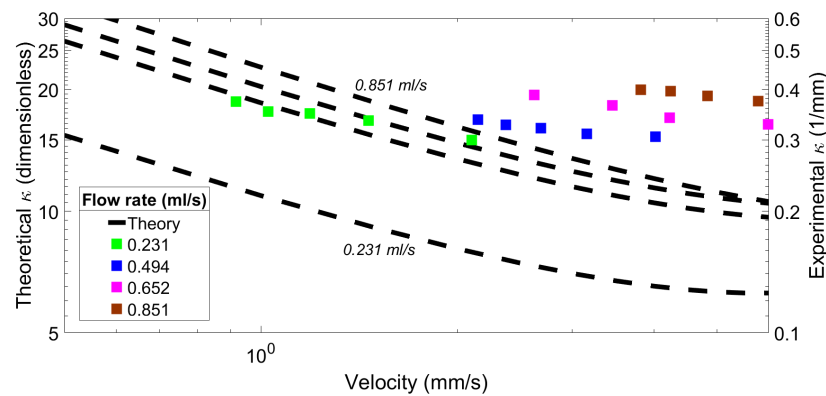


Figure 5.13: Comparison between theoretical calculation of curvature and experimental data. The dashed lines denote theory, displayed with the left y-axis, and the flow rate increases at the same pace as the experimental data. The colored points are for experimental data displayed with the right y-axis.

It is clear that both theory and experiment support an increased curvature with reduced fluid velocity. It also indicates the positive effect of flow rate. We have compared the overall scaling behaviour of the theory and experiment here using Equation (5.8) as several parameters are not able to be obtained for our system. The theory predicts a much stronger decrease in curvature with increased fluid velocity than we see experimentally (note that the scope of axis range for both axes is the same magnification from 5 to 30 and from 0.1 to 0.6). The discrepancy may stem from the fact that our system is constrained in the maximum height it can reach, deviating from the theory’s assumption of free surface fracture with a uniformly distributed compression stress acting along the fracture from the entry of the fluid

to the fracture tip. Our use of dimensionless parameters obtained from literature are for fracture of a uniform material, while here we separate two distinct materials. Also, the prefactor that involves dimensionless parameters needs to be deduced to a form with dimensional physical parameters to make more accurate curvature predictions. The main reason for the big difference in magnitude is because of the conversion from the time scale to the velocity. Similar reason can be seen in Wang and Detournay's study which shows the imbalance between dimensionless calculation and engineering calculation with dimensional parameters. If curvature is calculated with the time scale Equation (5.7) the curvature will have a closer value. Nevertheless, these differences do not affect the flow rate and fracture rate description, so the curvature equation for engineering calculations is still expected to follow a form of $\kappa = A \cdot Q^a (1/V)^b$.

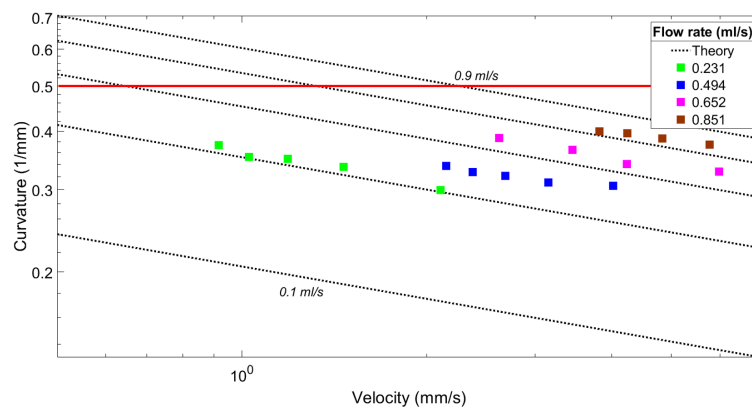


Figure 5.14: Experimental data with numerically fitted theoretical calculations plotted in a log axis. The dashed lines represent theoretical curvature, from the bottom to the top the theoretical flow rate increases from 0.1 mL/s to 0.9 mL/s with a 0.2 mL/s increment. The red line indicates $\kappa = 0.51 / \text{mm}$.

In order to quantify the safe threshold for cataract surgery, $\kappa = A \cdot Q^a (1/V)^b$ is fitted numerically to the data obtained from the experiments and merged to the same axis (Fig.5.14). Fitting the value $A = 0.0215$ and exponents $a = 0.49$ and $b = 0.23$, makes $\kappa = 0.0215 \cdot Q^{0.49} (1/V)^{0.23}$. The ultimate safe curvature discussed in Chapter

(4) can be correlated with the safe strain of eye lens capsule and thus defined as 0.5 mm^{-1} ¹⁵⁻¹⁸. As indicated in Fig.5.14, when the flow rate is 0.5 mL/s, most of the duration of flow will occur at a curvature lower than 0.5 mm^{-1} . When flow rate is higher than 0.5 mL/s, it is more likely the curvature will exceed the safe threshold. If used in cataract surgery under these conditions there is then a higher risk to the eye lens tissue. On the other hand, any flow rate that is lower than 0.5 mL/s would be considered much safer. A starting point for fluid design and operating conditions is then working with Equation (5.8) and surgeons to better understand and enhance the safety of cataract surgery.

It is interesting to see that the Newtonian Equation (5.3) is in agreement with the power-law Equation (5.8). If we look at an average viscosity of the power-law fluid during the whole fracture process, it can be written as

$$\bar{\mu}_e = \frac{1}{12} M'^{\frac{3}{n+2}} E'^{\frac{n-1}{n+2}} t^{\frac{2(1-n)}{n+2}} \int_0^1 \left(\frac{\Omega^2}{\Psi} \right)^{1-n} d\xi \quad (5.9)$$

this shows that $\bar{\mu}_e$ has a positive power-law relationship with time, which means that as separation continues, the decrease of fracture rate at the front causes the increase of the average viscosity¹². Combining this with the rheology of shear-thinning fluids (Fig.5.1), and with the Newtonian Equation (5.3), we understand that: as separation happens, the fracture rate at the front gradually decreases, causing the decrease of shear rate, which for shear-thinning fluids results in a higher viscosity; with higher viscosity the tissue curvature increases, causing bigger deformation.

5.4 Conclusion

This chapter proposed a general method based on previous published theories to describe the deformation conditions at the front of soft tissue undergoing shear-thinning induced hydraulic fracture. With a modified model, several fluids are tested and the results show a consistent trend with the equation proposed. In general, hydraulic fracture performed by a shear-thinning fluid will cause a dynamic change of the fracture front profile, so that as separation continues the deformation becomes larger. Also found is that increasing the flow rate causes overall bigger deformation. The results suggest that the shear-thinning fluids used in real surgery may put some potential risks on eye lens tissue because of the increase of viscosity during the separation. A determination of the safe threshold for cataract surgery has been made based on the data collected from our gelatin injection model, allowing us to specify restrictions on the safe injection flow rate. Further study could increase the accuracy of the model we utilised, take into account mechanical properties of the tissue, and include cataract surgery operation parameters.

5.5 References

- [1] V. Vasavada, V. A. Vasavada, L. Werner, N. Mamalis, A. R. Vasavada, A. S. Crandall, *Journal of Cataract & Refractive Surgery* **2008**, *34*, 1173–1180.
- [2] I. H. Fine, M. Packer, R. S. Hoffman, *Journal of Cataract & Refractive Surgery* **2003**, *29*, 16–19.
- [3] H. Kalantan, *Saudi Journal of Ophthalmology* **2012**, *26*, 41–49.
- [4] R. Grigorian, A. Castellarin, R. Fegan, C. Seery, L. Del Priore, S. Von Hagen, M. A. Zarbin, *British journal of ophthalmology* **2003**, *87*, 737–741.
- [5] R. J. Mackool, S. Nicolich, R. Mackool Jr, *Journal of Cataract & Refractive Surgery* **2007**, *33*, 553.

-
- [6] G. Kapoor, S. Seth, T. Ahluwalia, S. Dhar, *medical journal armed forces india* **2016**, 72, 242–246.
- [7] S. H. Dewey, *Journal of Cataract & Refractive Surgery* **2002**, 28, 11–14.
- [8] T. V. Ball, J. A. Neufeld, *Physical Review Fluids* **2018**, 3, 074101.
- [9] Z.-Q. Wang, E. Detournay, *Journal of Applied Mechanics* **2018**, 85, year.
- [10] D. Garagash, E. Detournay, *J. Appl. Mech.* **2000**, 67, 183–192.
- [11] F.-E. Moukhtari, B. Lecampion, *Journal of Fluid Mechanics* **2018**, 838, 573–605.
- [12] J. Adachi, E. Detournay, *International Journal for Numerical and Analytical Methods in Geomechanics* **2002**, 26, 579–604.
- [13] Y.-S. Chang, Y.-H. Lai, D. A. Dillard, *The Journal of Adhesion* **1989**, 27, 197–211.
- [14] M. Parsons, A. Polyakova, E. Stepanov, A. Hiltner, E. Baer, *The Journal of Adhesion* **1998**, 68, 45–63.
- [15] S. Krag, T. T. Andreassen, *Progress in retinal and eye research* **2003**, 22, 749–767.
- [16] H. B. Dick, S. E. Aliyeva, F. Hengerer, *Journal of Cataract & Refractive Surgery* **2008**, 34, 1367–1373.
- [17] S. Krag, T. Olsen, T. T. Andreassen, *Investigative ophthalmology & visual science* **1997**, 38, 357–363.
- [18] R. Fisher, *The Journal of physiology* **1969**, 201, 1–19.

Chapter 6

Complex fluid separation

We can not completely apply past theories to the description of more complex fluids that exhibit significant yield stress and normal stress behaviour. It is, however, worthwhile to learn the behaviours of these two fluid classes soft tissue hydraulic fracture because of their potential for more beneficial effects beyond what current fluids offer. Even if the fluids studied are not immediately helpful the information gained can aid in future formulation and fluid design efforts.

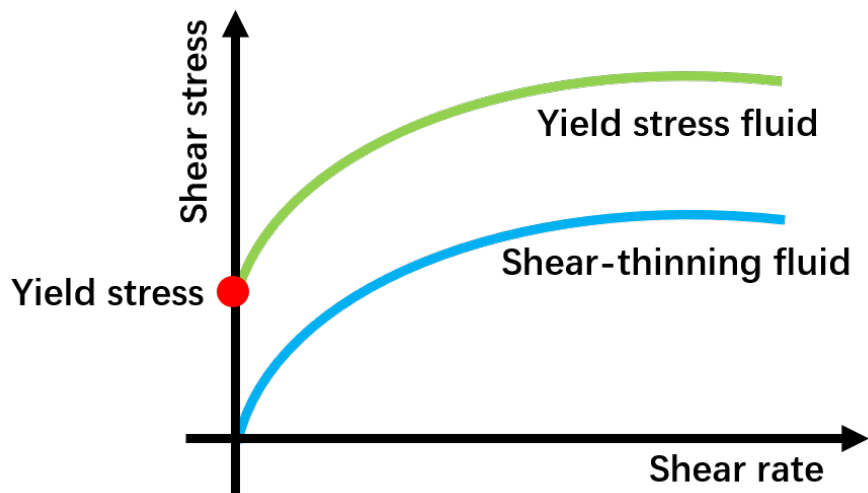


Figure 6.1: Schematic contrasting the rheology of a yield stress fluid and shear-thinning fluid. A certain minimum shear stress is needed to initiate movement of static yield stress fluids.

Broadly speaking, yield stress fluids are only able to flow and behave as a liquid when the applied shear stress exceeds a critical value, the yield stress. At stresses below the yield stress the system behaves as an elastic solid with no flow (Fig.2.21).

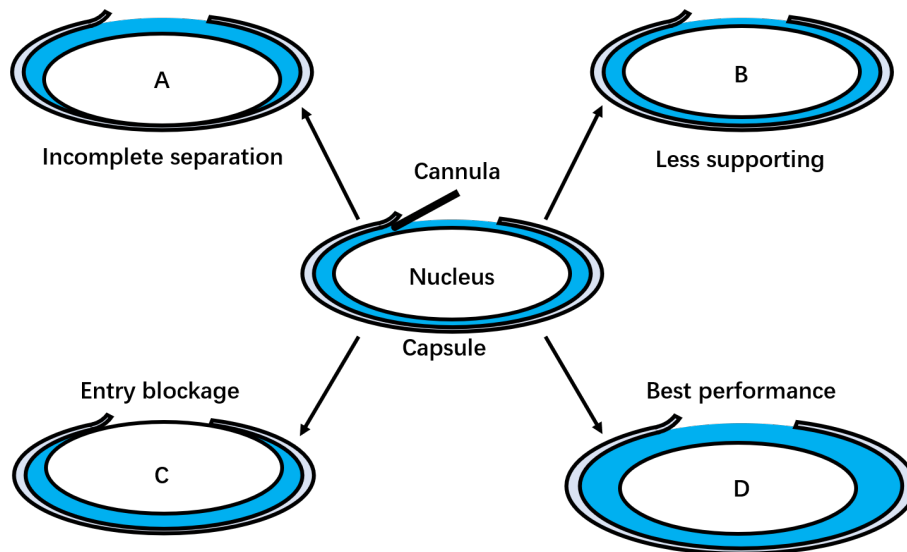


Figure 6.2: Schematic representation of performance of different fracture fluids. A: attachment still exists between capsule and nucleus; B: small clearance and less fluid support; C: easy movement of nucleus blocks the entry; D: good support and sufficient clearance.

Fig. 6.2 shows schematics of different types of outcomes during cataract surgery as a basis for discussing how a fluid and its properties could be beneficial. Generally, viscous fluids will provide support to the lens capsule as well as reducing the movement of the lens nucleus that might cause problems for the capsule^{1,2}. There is some precedent for using yield stress fluids as an aid to fracturing, as hydraulic fracturing of rock is known to use fluids with a yield stress as a way of propping open rock that has been previously ruptured^{3,4}. The difference between these two cases is that eye surgery currently uses viscoelasticity to delay flow while fracking uses elasticity to halt flow until certain conditions are met. We explore here whether such traits could be beneficial for soft tissue fracture.

At small scales of fracture, the geometry can be considered Poiseuille flow between two parallel stationary plates. For yield stress fluids flowing in such a geometry, the flow profile can be described by a plug shape which consists of the yielded region and unyielded region (Fig.6.3). The boundary between the zones

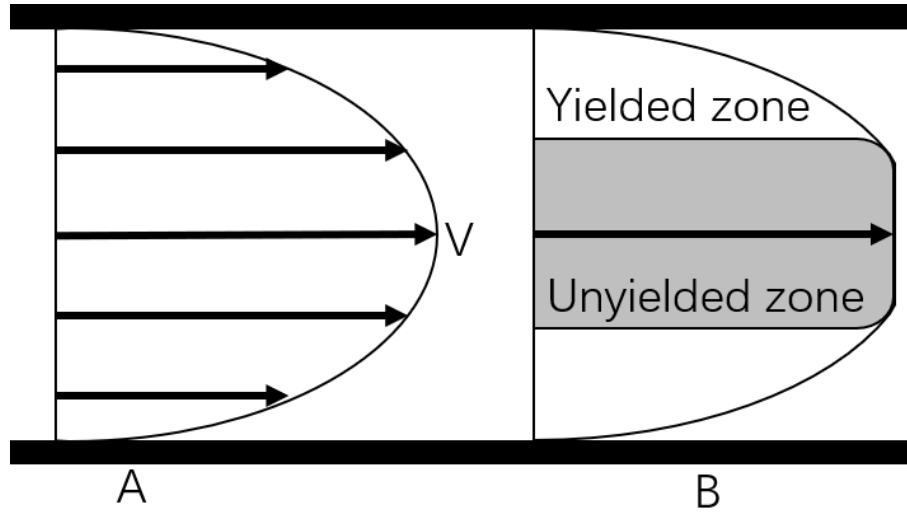


Figure 6.3: Comparison of velocity profile of shear-thinning fluids without yield stress (A) and with yield stress (B). The arrows indicate the local fluid velocity. For normal fluids, the velocity decays as the location approaches the wall because of drag. For yield stress fluids there is a yielded zone where fluid flows and acts like lubricant, and there is an unyielded zone where fluid is in a solid-like status.

occurs where the local shear stress equals the fluid yield stress. The yielded zone acts like a lubricant layer, starting from the wall of the plates and gradually vanishes as the shear stress caused by the friction keeps dropping from the wall to the centre of the streamline. At the location where shear stress is lower than the yield stress there is a transition to the unyielded zone in which fluid is solid-like and shows very low flow capability. In a squeezing flow that is similar to the flow at the fluid front of hydraulic fracture, the shear stress τ can be simply written⁵:

$$\tau = \mu \frac{dV}{dy} + \tau_0 \quad (6.1)$$

where τ_0 is the yield stress, dU/dy is the velocity gradient. This shows that the lower the velocity, the lower the shear stress.

A different type of non-Newtonian fluid rheology occurs when fluids possess significant normal stresses. A normal stress is a stress perpendicular to the direction of shear flow and it is independent of the fluid pressure. We are not aware of literature discussing the effects of high fluid normal stresses on hydraulic fracture. However the foundation of such behavior is simply lifting (or pulling together) boundaries in a flow. One example of such an effect is when particles suspended in pipe flow of a normal stress fluid experience strong migration toward the pipe centre where fluid shear rate is lowest. Ho and Leal suggests that for a shear-thinning fluid exhibiting normal stress, particle migration is dominated by normal stress. The effect of normal stress on particles can be expressed in a simple linear equation^{7,8}:

$$\Sigma = C_N + C_S \quad (6.2)$$

where C_N and C_S are contributions of normal and shear stresses respectively. Transforming this to describe hydraulic fracture, a general form of⁹

$$\Sigma = C_N + C_P = B \nabla^4 h + \rho g h \quad (6.3)$$

which shows the relationship between apparent hydraulic stress Σ , the contribution of normal stress C_N and height of the material h the fluid can lift.

6.1 Materials and methods

6.1.1 Experimental set-up

The injection model is the same as in Chapters 3, 4 and 5 with a bilayer structure and microfluidic channel. The top layer is made of 15% gelatin to mimic the eye lens capsule and the bottom layer (PDMS 1:10) is the nucleus. Carbopol solutions

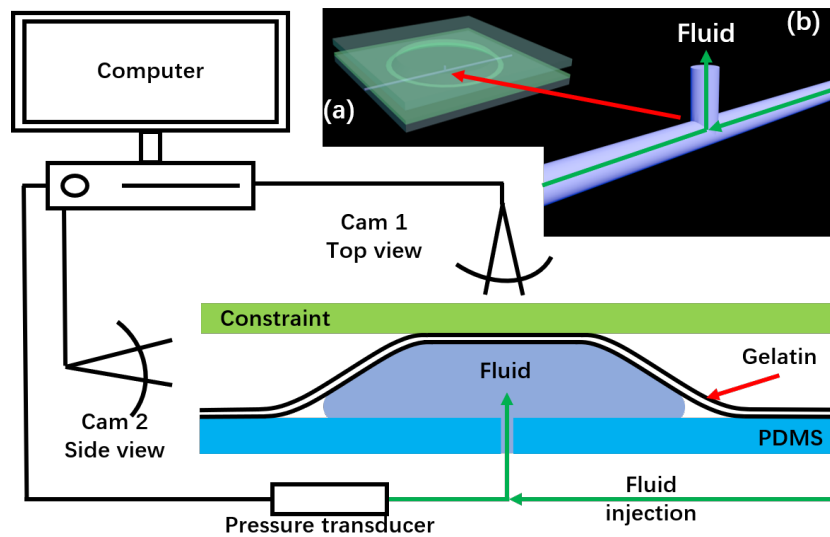


Figure 6.4: Schematic of experimental set-up and sample structure. Pressure transducer reads and records the pressure at the entry of the fluid into the micro-channel; compressed air is used to pressurize the liquid in the syringe and push it into the model. (a) 3D structure of injection model, bright green ring indicates the edge of blister where separation happens; (b) T-shape mould used for templating the micro-channel in the base layer.

(0.1% pH=6.7 $\tau_0 = 2.9$ Pa and 0.15% pH=6.04 $\tau_0 = 6.6$ Pa) are used for yield stress study; 0.1% hyaluronic acid (HA) solution (MW = $1.5 \sim 1.8 \times 10^6$ Da) is used to study the effects of normal stress.

Fig.6.4 shows a schematic of the experimental set-up. A glass slide is placed approximately 2.5 mm above the pre-made injection model to constrain the maximum height the gelatin layer can reach. In an experiment, the injection model is connected to a pressure transducer and syringe via the two ends of the micro-channel. Compressed air pressurizes the fluid in the syringe and creates pressure inside the system. The pressure transducer monitors instantaneous pressure and digitally records it. Two cameras are used to capture the top and side view of the experiment. The top view shows the extent of separation while the side view shows the profile of the tissue being separated.

Fluid rheology is measured using a TA Instruments stress-controlled DHR-1 rheometer with a cone and plate geometry with cone and plate geometry (cone diameter 60 mm, angle 2 degrees). Flow curves are performed over a shear rate range of 0.1-100 s^{-1} with flow sweep procedure. Shear stress, shear rate, viscosity and normal stress are all measured.

6.1.2 Curvature analyses

Using the same method as introduced in Chapters 4 and 5, the curvature is measured directly from the images of blister profile. The data processing and curvature measurement apply software ImageJ and MATLAB. Analysis is done by below procedure:

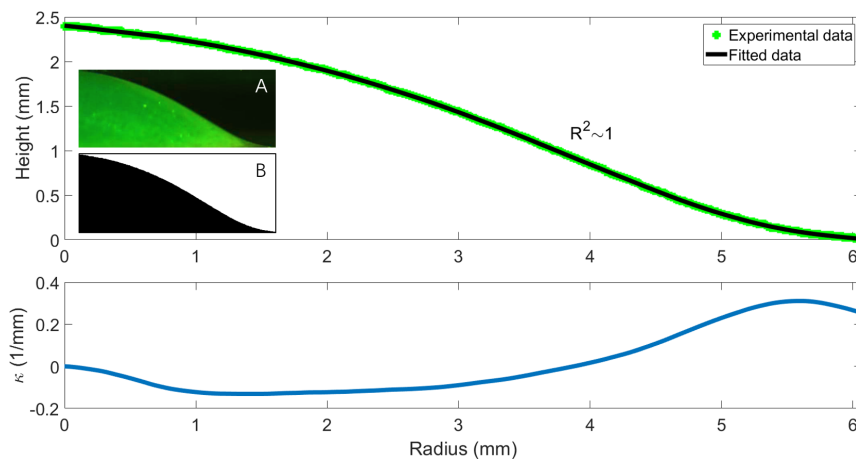


Figure 6.5: Curvature processing of blister profile. *A:* Raw image captured with camera. *B:* Binary image of *A* for quantification. Green color indicates experimental data extracted from *B* and black curve is the fitting by Equation (4.2). Curvature is taken at its maximum value.

- The blister image is obtained directly from experiment-setup camera (Fig.6.5 (A))
- It is input into ImageJ and converted to binary image with only black and white color (Fig.6.5 (B))

- The scale of B, 79.78 pixels/mm, is set in ImageJ allowing B to be digitized and exported to a coordinate (Fig.6.5 Green color)
- This data is then input into MATLAB and fitted by Equation (4.2), with the fitting $R^2 \sim 1$ (Fig.6.5)
- The curvature curve is then computed by MATLAB with code in Appendix (A), and the maximum value is also selected automatically as the curvature at the fracture front

The raw images are captured with a resolution that gives 79.78 pixels/mm scale, meaning that the minimum observable length unit being 0.0125 mm. This length scale is small enough for accurate curvature measurement and will be discussed in more details in Chapter (5). The fitting accuracy is shown to have $R^2 \sim 1$ which means a perfect fitting. Comparing the values of experimental data and fitted data the difference (error) in average is within 0.3% of the original data.

6.2 Results and Discussion

6.2.1 Yield stress fluids

It has been well discussed in Chapter (5) that hydraulic fracture conducted with shear-thinning fluids tends to lift the tissue higher at the fracture front at longer times as the fluid slows due to drag. A similar phenomenon is seen with yield stress shear-thinning fluids (Fig.6.6), where the blister profile becomes steeper at the end of separation. Here, however such behaviour is more complicated as we often see the yield stress cause sufficient pressure to build in the system that the soft tissue model ruptures (Fig.6.6). Rupture occurs fairly early in the process, preventing significant separation from occurring. Rupture typically occurs at the fracture front,

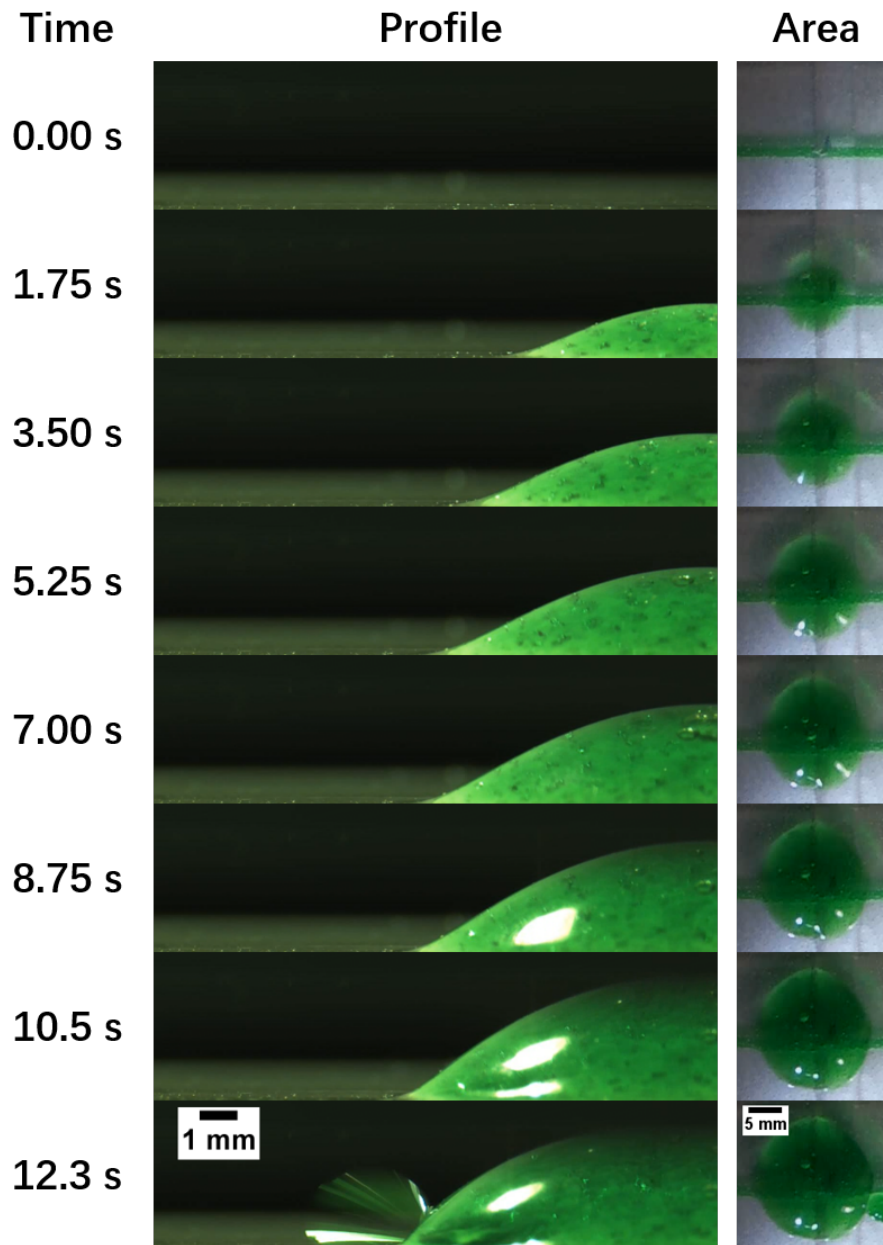


Figure 6.6: Hydraulic fracture conducted with 0.1% Carbopol at a pH = 6.7 and 15 psi driving pressure. The profile shows an increase of curvature and the dynamic area shows the decrease of fracture rate at the front.

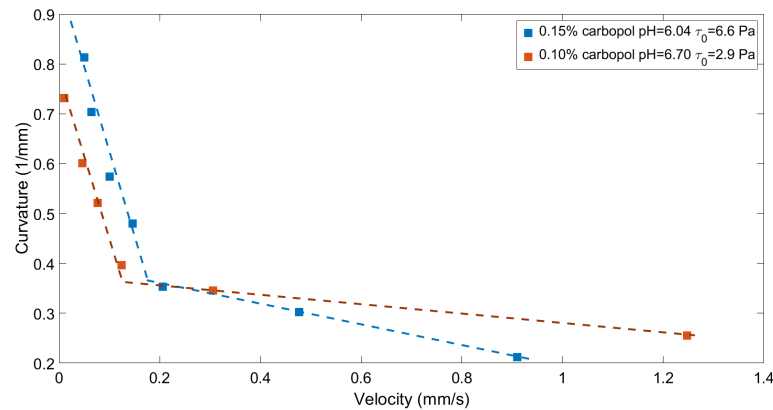


Figure 6.7: Plot of the dynamic curvature changes during tissue separation with two yield stress fluids. In the beginning the velocity (fracture rate) is fast and the front has a small curvature. As velocity decreases the curvature keeps increasing to a discontinuous point where a sudden rise can be seen.

and we note that a significant level of deformation occurs leading up to the tissue failure.

As stated in Chapters 4 and 5 the tissue deformation is quantified by the fracture front curvature. Bigger curvature represents bigger deformation. Fig.6.7 shows the relationship between curvature and fracture rate for fluids with 2.9 and 6.6 Pa yield stress. It is clear that there are two stages in yield stress fluid fracture. The first a slow build in curvature while the fluid is still flowing and mobile. Here the fracture rate is high, and the curvature is small. The second stage is when accumulation of fluid occurs. Here the fracture becomes slow and the curvature increases dramatically because of the vertical accumulation of fluid. The transition curvature for both high and low yield stress fluids is found to be at a curvature $\sim 0.37 \text{ mm}^{-1}$, and the critical velocity for both fluids is similar with higher yield stress a bit higher. The behaviour in Fig6.7 can be explained by a transition from yielded to unyielded behavior.

As shown in Fig.6.8, part of the yield stress fluid flowing in a narrow gap is unyielded so it can only slip on the yielded part. The yielded part is sheared by the drag on the wall, where at the wall the flow velocity is zero. At fast flow velocity, there

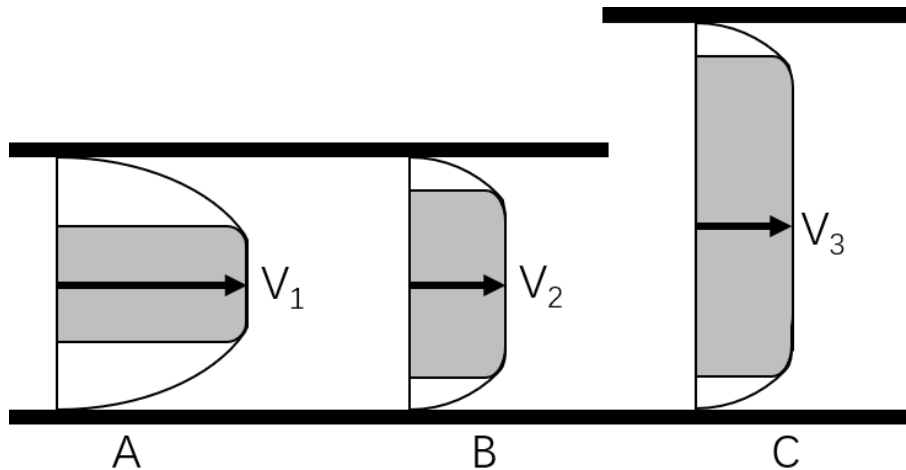


Figure 6.8: Schematic of yield stress fluid flow. The white zone is the yielded zone undergoing fluid-like flow and the grey zone the unyielded zone in a solid-like status. A-B: As velocity decreases, a smaller shear stress will cause a bigger unyielded zone to form and continuously weaken the flow capability. C: The increase of height has similar effects to a decrease of velocity and also makes the total flow more unyielded.

is a bigger velocity gradient between the wall and the boundary of the unyielded zone. As a result the yielded part dominates and the fluid flows easily. As separation occurs the velocity decreases, which reduces the velocity gradient as well as the shear stress. At smaller shear stress less fluid exhibits is yielded increasing the size of the unyielded zone and dominating the front. Eventually at a critical point the fluid accumulation and degraded flow capability deforms the tissue beyond its yield strain and rupture occurs. The dynamic process is clear from the plot of curvature with velocity.

While the loss of fluid flow velocity plays a key role, the fluid accumulation is also critical to understand the tissue failure. At the fracture front the tissue is bent by a uniformly distributed compression stress ($\sigma = 101 \times 10^3$ Pa), and according to¹⁰ $B \frac{d^4 h}{dx^4} = \sigma$ the fracture front can be modelled theoretically (Fig.6.9 $L = 0$ being the location of fluid front). As the height of fluid front increases, the tissue is bent

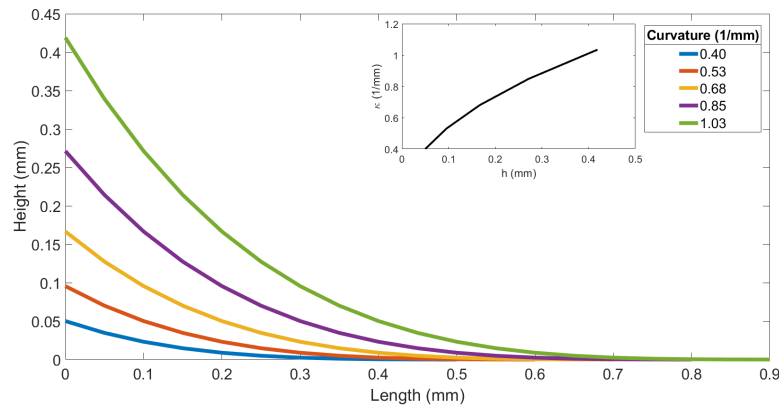


Figure 6.9: Profile of the fracture front modeled with equation **bending**. $L = 0$ is the location of fluid front. The inset shows the curvature calculated by $\kappa = 2h/L^2$ as a function of the height.

and curvature is increased. Applying the curvature equation $\kappa = 2h/L^2$, theoretical curvature is plotted against height (Fig.6.9 inset). The results show the expected increase in curvature with height. When the height increases, even for the same velocity gradient, the unyielded zone merges in a larger portion, which increases the resistance on the bulk flow (Fig.6.8). These results indicate the strong effects of yield stress fluids on hydraulic fracture of soft tissue. While only two yield stress values have been studied, it is possible more fragile networks might help avoid such behaviour while providing more benefit. While yield stress fluids are not currently used in eye surgery, they can form from normally shear-thinning fluids that become unstable, such as when polymeric solutions aggregate. These data indicate the importance of check for such instabilities as part of product quality tests and specifications.

6.2.2 Normal stress fluids

After discussing the effects of viscosity and shear behavior in Chapters 4 and 5, and yield stress in Section (6.2.1), the last rheological property we study is normal

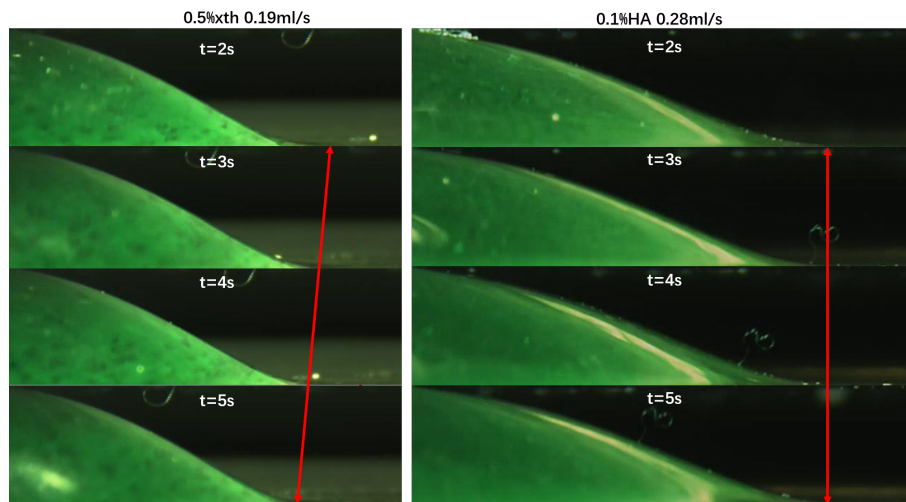


Figure 6.10: Comparison of deformation between a shear-thinning fluid (0.5% xanthan) and a high normal stress shear-thinning fluid (0.1% HA). Without a normal stress, the shear-thinning fluid causes a dynamic increase of deformation on tissue during injection. With a normal stress the fluid deformation is balanced to be almost static.

stress. Here we tested two fluids with different normal stresses which shows exactly different separation behavior.

To start, from our experiments, a clear observation is that 0.1% hyaluronic acid (HA) solution causes a stable and static blister shape, meaning that the deformation of tissue caused by apparent fluid pressure remains unchanged. Note that 0.1% HA has a similar shear-thinning behavior like 0.5% xanthan gum, and the latter one brings a dynamically increased deformation to the tissue during the whole separation. This can be seen visually in Fig.6.10 in which the profile of xanthan gum becomes steeper while HA solution remains the same over time.

Measuring the curvature and plotting shows the same trend (Fig.6.11). The curvature for 0.1% HA is constant with varying velocity while for 0.5% xanthan gum it changes with both the velocity and flow rate. 0.1% HA has overall smaller curvature, even for when the flow rate is higher. This can be caused by two reasons, first is the viscosity of HA is lower than xanthan gum, the second is difference in normal

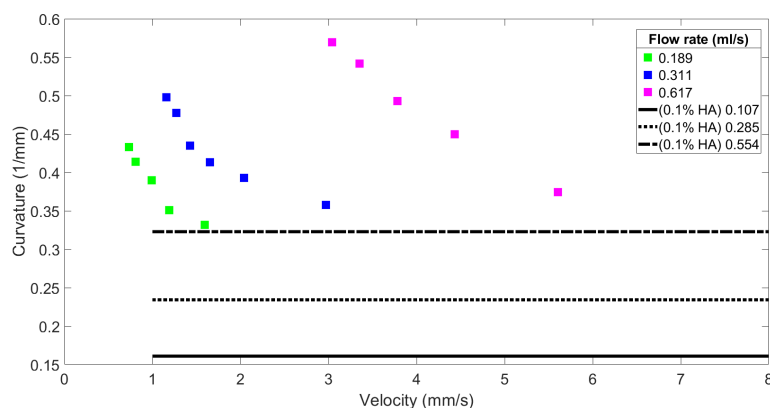


Figure 6.11: Measured dynamic curvature for 0.5% xanthan gum and static curvature for 0.1% HA at different flow rates.

stress. Besides, such a big difference in the dynamics of curvature depends only on the normal stresses (Fig.6.12 (A)).

The constant deformation and smaller curvature caused by the normal stress of fluid can be explained by making an analogy with the migration of suspended particles in high normal stress fluid pipe flow^{8,11}. The hydraulic fracture and particle migration essentially drive the lifting or pulling effect of hydrodynamic pressure on movable objects, either particles or tissue. Generally the stresses imposed on the object are linearly dependent on the contributions of normal stress and viscosity. Though the contribution of normal stress requires more modelling and simulations to be modeled in thin film flow with lubrication theory, we can determine experimentally how the normal stress affects tissue deformation. Normal stress in flowing fluid generally resists (positive value) the compression caused by shear or pulls itself (negative value) together if sheared, depending on the relative direction to the shear¹². That being said, if the fluid with negative normal stress passes through two paralleled plates it tends to bring them together. This phenomenon has been observed in a study by Keentok *et al.*, who measures the normal stress by analysing the height of free surface of flow in a semicircular pipe caused by the normal stress

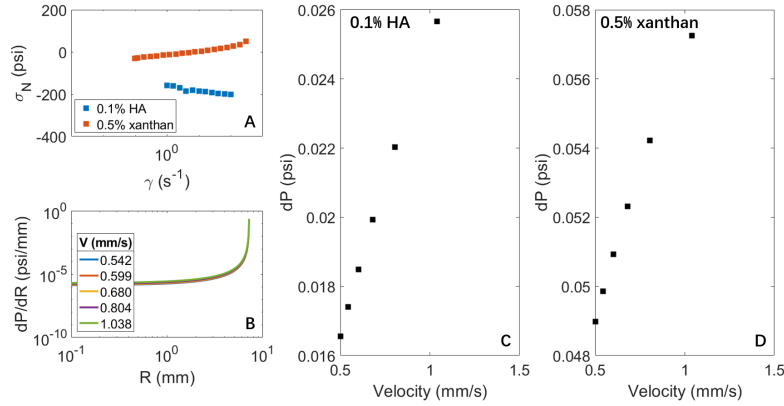


Figure 6.12: A: Normal stresses of 0.1% HA and 0.5% xanthan gum obtained from rheological data. B: Pressure drop along the blister at varying velocity. C: Total pressure loss during separation with 0.1% HA. D: Total pressure loss during separation with 0.5% xanthan gum. C,D insets: schematics of stresses distribution during separation for two types of normal stresses.

pulling effect. From their results the flowing fluid surface becomes convex because of negative normal stress. Thereby we look further into the normal stress and apparent pressure for separation with both 0.1% HA and 0.5% xanthan gum, aiming to see the difference in lifting caused by viscosity and normal stress.

Mapping the pressure and stress behavior in the deforming region (Fig.6.10 curved profile) aids the understanding on normal stress effects. Firstly the pressure gradient dP/dR (Fig.6.12 (B)) is calculated from power-law lubrication equation¹⁴ $\frac{dP}{dr} = 2^{n+1} \left(\frac{2n+1}{n}\right)^n \frac{MV^n}{h^{n+1}}$, with h obtained from experiment, n and M from rheology measurement, and V from¹⁴ $V = Q/h$. Then the total pressure loss dP is calculated by the integration of pressure gradient over the time scale of the separation. Total pressure loss is plotted for two fluids 0.1% HA and 0.5% xanthan gum in Fig.6.12 (C) and (D). The rheology measurement suggests that 0.1% HA has negative normal stresses ranging from roughly -0.023 to -0.029 psi while for 0.5% xanthan gum the normal stress shows a much smaller variation from -0.004 to 0.007 psi (Fig.6.12 (A)). such big difference can be compared with the magnitude of total pressure loss in

the blister to understand the effect of normal stress, note that the pressure loss dP is negative, here the figure plot it in positive axis for easy graph reading (Fig.6.12 (C,D)). It is clear that the total drop of pressure in the blister for 0.1% HA varies from roughly -0.026 psi to -0.016 psi. Comparing with the normal stresses obtained from experimental rheology data the conclusion is that both the pressure loss and normal stress of 0.1% HA are in the same magnitude, meaning that they might have similar qualities of effects on the apparent fluid pressure. Nevertheless, for 0.1% xanthan gum, the pressure loss is relatively high, between about -0.058 psi and -0.048 psi, while the normal stress is far lower than 0.1% HA, suggesting a weaker influence under the same pattern. Keentok *et al.*'s study relates the deformation of free surface flowing viscous fluid to normal stress and the results suggests that a normal stress of approximately -0.0145 to -0.0218 psi is able to deform the height of fluid free surface by up to 0.38 ± 0.01 mm, which if we connect to our experimental data, makes an agreement. Thus, our results suggests that in separation process, the normal stress balances the total pressure loss caused by viscous drag and makes the pressure and deformation curvature a more static state.

Besides, because of these effects of negative normal stress, 0.1%HA solution has an smaller curvature at even higher flow rate.

This has shown the potential to adapt normal stress fluids to optimize the performance of hydraulic fracture and make use of it further in cataract surgery. In an ideal case, new fluids could be designed to exploit these traits. However, it is important to point out the relatively optimal performance of the HA solution, the current choice for surgical viscodissection. While it is unlikely the current fluid was chosen by surgeons for these specific rheological properties, it is clear that a gradual process of optimisation has occurred over the years by practical observations and

documentation. We hope these studies contribute to and potentially accelerate future development efforts.

6.3 Conclusion

The experiments conducted with complex fluids, yield stress and high normal stress fluids, have shown distinct hydraulic fracture behaviors. For yield stress fluids the emergence of yielded and unyielded zones caused by the fluid-layer friction and wall friction has great effects on the flow capability of fluids at the fracture front. Generally, when separation happens the shear stress at the front decays with the decrease of velocity gradient. Such decay results in the dominating effects of unyielded zone, which lowers the flow ability of fluid and causes it to accumulate locally. When this happens the tissue is deformed to an extent beyond its limitation. Consequently, tissue rupture eventually occurs. Use of a similar fluid in cataract surgery would be dangerous and irresponsible as such rupture in an eye lens capsule would cause permanent damage and loss of vision. At the current stage, despite the fact that yield stress fluids might provide good support after the separation of eye tissue is done, their use is not recommended because of potential risks.

For normal stress fluids, a very helpful behaviour is noted in which the two tissue layers are kept from significant deformation by the negative normal stresses in flow. Although each fluid has a similar shear stress behaviour, the overall increased normal stress causes little variation in blister deformation during a fracture experiment while the decreased normal stress shows significant variations. The findings have shown great potential to use manipulated negative normal stress fluids to make soft tissue deformation safer and to explain why currently used fluids work so well.

6.4 References

- [1] A. R. Vasavada, D. Goyal, L. Shastri, R. Singh, *Journal of Cataract & Refractive Surgery* **2003**, 29, 309–314.
- [2] V. Vasavada, V. A. Vasavada, L. Werner, N. Mamalis, A. R. Vasavada, A. S. Crandall, *Journal of Cataract & Refractive Surgery* **2008**, 34, 1173–1180.
- [3] A. O. Bessmertnykh, E. V. Dontsov, *Journal of Applied Mechanics* **2019**, 86, year.
- [4] A. R. de Castro, A. Ahmadi-Sénichault, A. Omari, *Advances in Water Resources* **2020**, 146, 103794.
- [5] S. Wilson, *Journal of Non-Newtonian Fluid Mechanics* **1993**, 47, 211–219.
- [6] B. Ho, L. Leal, *Journal of Fluid Mechanics* **1976**, 76, 783–799.
- [7] J. F. Morris, F. Boulay, *Journal of rheology* **1999**, 43, 1213–1237.
- [8] R. M. Miller, J. F. Morris, *Journal of non-newtonian fluid mechanics* **2006**, 135, 149–165.
- [9] T. V. Ball, J. A. Neufeld, *Physical Review Fluids* **2018**, 3, 074101.
- [10] Z.-Q. Wang, E. Detournay, *Journal of Applied Mechanics* **2018**, 85, year.
- [11] K. W. Seo, H. J. Byeon, H. K. Huh, S. J. Lee, *RSC advances* **2014**, 4, 3512–3520.
- [12] P. A. Janmey, M. E. McCormick, S. Rammensee, J. L. Leight, P. C. Georges, F. C. MacKintosh, *Nature materials* **2007**, 6, 48–51.
- [13] M. Keentok, A. Georgescu, A. Sherwood, R. Tanner, *Journal of Non-Newtonian Fluid Mechanics* **1980**, 6, 303–324.
- [14] J. Desroches, E. Detournay, B. Lenoach, P. Papanastasiou, J. R. A. Pearson, M. Thiercelin, A. Cheng, *Proceedings of the Royal Society of London. Series A: Mathematical and Physical Sciences* **1994**, 447, 39–48.

Chapter 7

Conclusion

Cataract is one of the greatest human health challenges, accounting for almost half of blindness cases. It is caused by physiology and aging and is irreversible, so the only effective treatment is cataract surgery. Despite the success of cataract surgery, there are numerous factors that have not been quantified or optimised in a way that can predict safety and relate measurable properties to the risk of lens capsule rupture. In addition there is not currently sufficient knowledge to begin design of robotic surgical control systems. This project aims to provide some of these details and, hopefully, enhance safety of cataract surgery. The objectives are to understand the fluid separation mechanism and improve connections between rheology, hydrodynamics and adhesion.

In Chapter (2), the structure of eye lens and bio-mechanics relating to the aging and physiology were introduced. The cataract surgery separation process was narrowed down to a hydraulic fracture problem, a theory to describe flow behavior of multiple fluid types in tissue fracture. The separation is dominated by the fracture front tip, which means the radius propagation and deformation is determined by the conditions of the fracture front. The extent of separation and the curvature at the fracture front are shown to be critical variables for measurement as a path to characterising cataract surgery processes. The conditions can be described with flow hydraulic properties and fluid rheology properties. Relating theories were proposed to explain specifically how the volumetric flow rate, flow velocity, viscosity,

yield stress and normal stress affect the propagation of fluid and deformation of tissue.

In Chapter (3), the blister test was introduced to measure the adhesion of soft tissue on an rigid substrate, and a model was designed to mimic the separation process of cataract surgery. By blister test, the adhesion strength for the testing system proposed in this project varies between 0.93 J/m^2 and 1.52 J/m^2 depending on the roughness, with rougher surfaces providing higher adhesion strength. The highest adhesion is used, allowing a more stable separation and partially mimicking heterogeneous biological tissues. The results also indicate the potential for blister test use in measurement of adhesion strength of actual soft and brittle biological tissues. The test's relatively gentle conditions and lack of direct destructive contact with the sample prevents unexpected tissue damage and related energy depletion.

Chapter (4) proposed a viscosity-dominated hydraulic fracture process for eye lens capsule removal with Newtonian fluids. The effectiveness of separation is studied for a blister with constrained height. The radius equation is revised to show a flow rate dependency. At higher flow rates the separation is more effective and this follows $R \sim \sqrt{Qt/\pi h}$. Deformation of tissue as a result of varying viscosity and flow rate in Newtonian fluid injection is studied and it is found that both the increase of these two parameters will cause an increase of tissue curvature at the fracture front, increasing deformation and rupture risk ($\kappa \sim \mu^{1/3} Q^{7/15}$). This finding can be applied to current cataract surgery which mostly uses injected balanced salt solution (BSS). For BSS it would be good to control or set an upper limit to the flow rate so that the deformation does not threaten human eye tissue safety. The results also provide a general idea of the safe range of BSS injection which may aid the performance of cataract surgery.

Chapter (5) proposed a general method based on previous published theories to describe the deformation conditions at the front of soft tissue undergoing shear-thinning induced hydraulic fracture. With a modified model, the results show a consistent trend with the equation proposed. In general, hydraulic fracture performed by a shear-thinning fluid will cause a dynamic change of the velocity and profile of fracture front, so that as separation continues the deformation becomes larger. Also found is that increasing the flow rate causes overall bigger deformation. The results suggest that the shear-thinning fluids used in real surgery may put some potential risks on eye lens tissue because of the increase of viscosity during the separation. A determination of the safe threshold for cataract surgery has been made based on the data collected from our gelatin injection model, allowing us to specify restrictions on the safe injection flow rate. Further study could increase the accuracy of the model we utilised, take into account mechanical properties of the tissue, and include cataract surgery operation parameters.

Chapter (6) The experiments conducted with complex fluids, yield stress and high normal stress fluids, have shown distinct hydraulic fracture behaviors. For yield stress fluids the emergence of yielded and unyielded zones caused by the fluid-layer friction and wall friction has great effects on the flow capability of fluids at the fracture front. Generally, when separation happens the shear stress at the front decays with the decrease of velocity gradient. Such decay results in the dominating effects of unyielded zone, which lowers the flow ability of fluid and causes it to accumulate locally. When this happens the tissue is deformed to an extent beyond its limitation. Consequently, tissue rupture eventually occurs. Use of a similar fluid in cataract surgery would be dangerous and irresponsible as such rupture in an eye lens capsule would cause permanent damage and loss of vision. At the current stage, despite the fact that yield stress fluids might provide good support after the

separation of eye tissue is done, their use is not recommended because of potential risks.

For normal stress fluids, a very helpful behaviour is noted in which the two tissue layers are kept from significant deformation by the negative normal stresses in flow. Although each fluid has a shear stress expression, the overall larger negative normal stress causes little variation in blister deformation during a fracture experiment, while the small normal stress shows significant variations. The findings have potential to enable manipulated negative normal stress fluids to make soft tissue deformation safer and to explain why currently used fluids work so well.

In summary, cataract surgery eye lens removal is a micro scale hydraulic fracture (separation), and the performance is related to fluid flow properties. The viscosity, velocity and flow rate are all able to increase the deformation of separated tissue. This is applicable for both Newtonian and shear-thinning fluids and the only difference is that for Newtonian fluids the constant viscosity causes static deformation, while for shear-thinning fluids the dynamic viscosity causes more complex dynamic deformation. Yield stress fluids are proved to be unsuitable for separation, at least when yield stress magnitude is significant, as stagnant fluid accumulation may cause rupture to the tissue. Normal stress fluids have shown potential application in lowering the deformation of tissue because of the negative normal stress.

Further studies are needed to focus on: 1. improving the dimensionless approximation of shear-thinning fluid behavior for more accurate prediction 2. numerical model of normal stress hydrodynamics to provide more precise explanation of the normal stress effects on hydraulic fracture 3. accordingly, manipulate fluid rheology to optimize the cataract surgery process 4. generate more modelling for design of robust automatic surgery control systems.

Appendix A

MATLAB - curvature measurement code

```
fittedmodel(xx)
yy=ans

% spline method
sp = spline(xx,yy);    % spline(x,y)

x = xx(1):0.01:xx(length(xx));
y = ppval(x,sp);

subplot(211)
for i=1:length(xx)
    plot(xx(i), yy(i), 'b*')
    hold on
end
plot(x,y, 'r');
legend('Fitted data')
grid on
title('Profile')

%gradient
for i=1:(length(x)-1)
    dx(i)=x(i+1)-x(i);
    dy(i)=y(i+1)-y(i);
    ddy(i)= dy(i)/dx(i);
end

%curvature
```

Appendix A. MATLAB - curvature measurement code

```
for i = 1 : (length(x)-2)
    ddx(i) = dx(i+1) - dx(i);
    ddy(i) = dy(i+1) - dy(i);
    K(i)=(dx(i)*ddy(i)-dy(i)*ddx(i))/((dx(i)*dx(i)+dy(i)*dy(i))^1.5);
end

% subplot(312)
% ud=linspace(xx(1),xx(length(xx)),(length(x)-1));
% plot(ud,ddy)
% grid on
% title('gradient')

subplot(212)
uu=linspace(xx(1),xx(length(xx)),(length(x)-2));
plot(uu,K)
grid on
title('Curvature')
max(K)
```

Appendix B

MATLAB - error propagation code

```
syms h;
r=(p2^2-sqrt(64*p3.*h/p1)).^0.5;
dr=diff(r);
ddr=diff(dr);
k=abs(ddr)/(1+dr^2)^1.5;
dk=diff(k);
subplot(131);
ezplot(r);
subplot(132);
ezplot(k);
subplot(133);
ezplot(dk)
```